Intercomparison of airborne and surface-based measurements during the CLARIFY, ORACLES and LASIC field experiments

Paul A. Barrett[1], Steven J. Abel[1], Hugh Coe[2], Ian Crawford[2], Amie Dobracki[3,], James Haywood[4,1], Steve Howell[5], Anthony Jones[1,4], Justin Langridge[1], Greg M. McFarquhar[6,7], Graeme J. Nott[8], Hannah Price[8], Jens Redemann[6], Yohei Shinozuka[9], Kate Szpek[1], Jonathan W. Taylor[2], Robert Wood[10], Huihui Wu[2], Paquita Zuidema[3], Stéphane Bauguitte[8], Ryan Bennett[11], Keith Bower[2], Hong Chen[12], Sabrina Cochrane[12], Michael Cotterell[4,13], Nicholas Davies[4,14], David Delene[15], Connor Flynn[16], Andrew Freedman[17], Steffen Freitag[5], Siddhant Gupta[6,7], David Noone[18,19], Timothy B. Onasch[17], James Podolske[20], Michael R. Poellot[15], Sebastian Schmidt[12,21], Stephen Springston[22], Arthur J. Sedlacek III[22], Jamie Trembath[8], Alan Vance[1], Maria Zawadowicz[22], Jianhao Zhang[3,23,24]

[1]Met Office, Exeter, EX1 3PB, UK
[2]Department of Earth and Environmental Sciences, University of Manchester, M13 9PL, UK
[3]Rosential School of Marine and Atmospheric Science, University of Miami, Miami, FL 33149, USA
[4]University of Exeter, Exeter, EX4 4PY, UK
[5]Department of Oceanography, University of Hawai'i at Mānoa,, Honolulu, HI, USA
[6]School of Meteorology, University of Oklahoma, Norman, OK, USA
[7]Cooperative Institute for Severe and High-Impact Weather Research and Operations, University of Oklahoma, Norman, OK, USA
[8]FAAM Airborne Laboratory, Cranfield, MK43 0AL, UK
[9]Universities Space Research Association, Columbia, MD, USA
[10]Department of Atmospheric Sciences, University of Washington, Seattle, WA, USA
[11]Bay Area Environmental Research Institute, NASA Ames Research Centre, Moffett Field, Mountain View, CA, USA
[12]Department of Atmospheric and Oceanic Sciences, University of Colorado, Boulder, CO, USA
[13]School of Chemistry, University of Bristol, Bristol, BS8 1TS, UK
[14]Haseltine Lake Kempner, Bristol, BS1 6HU, UK
[15]Department of Atmospheric Sciences, University of North Dakota, Grand Forks, ND, USA
[16]School of Meteorology, University of Oklahoma, Norman, OK, USA
[17]Aerodyne Research Inc., Billerica, MA, USA
[18]College of Earth, Ocean, and Atmospheric Sciences, Oregon State University, Corvallis OR, USA
[19]Department of Physics, University of Auckland, Auckland, New Zealand
[20]NASA Ames Research Centre, Moffett Field, Mountain View, CA, USA
[21]Laboratory for Atmospheric and Space Physics, University of Colorado, Boulder, CO, USA
[22]Brookhaven National Laboratory, Upton, NY, USA
[23]NOAA Chemical Sciences Laboratory (CSL), Boulder, CO, USA
[24]Cooperative Institute for Research in Environmental Sciences (CIRES) at the University of Colorado Boulder, Boulder, CO, USA

Correspondence to: Paul A. Barrett. (paul.barrett@metoffice.gov.uk)

Abstract. Data are presented from intercomparisons between two research aircraft, the FAAM BAe-146 and the NASA Lockheed P3, and between the BAe-146 and the surface-based DOE (Department of Energy) ARM (Atmospheric Radiation Monitoring) Mobile Facility at Ascension Island (8 S, 14.5W, a remote island in the mid-Atlantic). These took place from 17 August to 5 September 2017, during the African biomass burning season. The primary motivation was to give confidence in the use of data from multiple platforms with which to evaluate numerical climate models. The three platforms were involved

in the CLouds-Aerosol-Radiation Interaction and Forcing for Year 2017 (CLARIFY-2017), ObseRvations of Aerosols above CLouds and their intEractionS (ORACLES), and Layered Atlantic Smoke and Interactions with Clouds (LASIC) field experiments. Comparisons from flight segments on six days where the BAe-146 flew alongside the ARM facility on Ascension Island are presented, along with comparisons from wing-tip to wing-tip flight of the P3 and BAe-146 on 18th August 2017. The intercomparison flight sampled a relatively clean atmosphere overlying a moderately polluted boundary layer, while the 6 fly-bys of the ARM site sampled both clean and polluted conditions 2-4 km upwind. We compare and validate characterisations of aerosol physical, chemical, and optical properties, atmospheric radiation, and cloud microphysics between platforms. We assess the performance of measurement instrumentation in the field, under conditions where sampling conditions are not tightly controlled as in laboratory measurements where calibrations are performed. Solar radiation measurements compared well between airborne platforms. Optical absorption coefficient measurements compared well across all three platforms, even though absolute magnitudes were often low (<10 Mm^{-1}) and close to the sensitivity limits of measurement instrumentation thereby confounding assessments of the comparability of absorption Ångström exponent characterisations. Aerosol absorption measurements from airborne platforms were more comparable than aircraft-to-ground observations. Scattering coefficient observations compared well between airborne platforms, but agreement with ground-based measurements was worse, potentially caused by small differences in sampling conditions or actual aerosol population differences. Chemical composition measurements followed a similar pattern, with better comparisons between the airborne platforms. Thermodynamics, aerosol, and cloud microphysical properties generally compared well.

1 Introduction

A number of in situ and remote sensing observational field campaigns involving multiple airborne and ground-based measurement platforms operated in the southeast Atlantic region from 2016 to 2018 (Fig. 1, Table 1). The overarching aim of this unprecedented observational effort was to provide constraints with which to address the disparity in radiative forcing estimates due to cloud and aerosol processes between leading climate models, such as those contributing to the AeroCom intercomparison exercise (Stier et al., 2013). The uncertainty in radiative forcing estimates in the southeast Atlantic is related to poorly constrained optical properties of the absorbing biomass burning aerosols (BBA), discrepancies between the representation of marine boundary layer clouds, the location in the vertical of the aerosols relative to these clouds, and the interaction of these aerosols with oceanic boundary layer clouds (Zuidema et al., 2016).

International projects (Zuidema et al., 2016) including CLARIFY-2017 (Haywood et al., 2021), ORACLES (Redemann et al., 2021), LASIC (Zuidema et al., 2018) and AEROCLO-SA (AErosol, RadiatiOn, and CLouds in Southern Africa: Formenti et al., 2019) had many overlapping objectives, aiming to determine the optical, chemical and physical properties of BBA and thus the radiative impacts of those aerosols on climate, through both direct radiative effects and impacts on the properties of clouds. Figure 2 shows the flight tracks over the three years of sampling between 2016 and 2018 for the airborne platforms. CLARIFY and ORACLES focussed on measurements over the southeast Atlantic Ocean and AEROCLO-SA supplemented this with observations over Namibia and the near-coastal ocean. Direct comparisons with the AEROCLO-SA were not possible due to the separation in space and time between it and the other campaigns. Here we focus on observations from the CLARIFY, ORACLES and LASIC components as side-by-side intercomparison data are available.

Most measurements of relatively fresh BBA close to the coast of Africa were taken with the P3 during ORACLES while more aged BBA was measured from the LASIC and CLARIFY-2017 platforms. Confidence that the contrasts between the measurement sets are not simply a result of instrument biases is critical for understanding aerosol aging. A key benefit of this collaboration is that it provides information regarding the comparability of measurements made from the various platforms, provided the instrumentation remains well-calibrated. This facilitates more reliable assessment of spatiotemporal gradients made by compositing data from the different platforms.

Here we present results from a wing-tip to wing-tip airborne intercomparison flight between the NASA P3 (Flight PRF05Y17) and the FAAM BAe-146 (Flight C031) on 18th August 2017, with both aircraft departing from the Wideawake Airfield on Ascension Island. The intercomparison was composed of flight segments in the pristine free-troposphere, within a moderately polluted marine boundary layer, and through an elevated pollution layer. Additional comparisons were made by FAAM flying adjacent to the ARM site on Ascension Island following this airborne intercomparison and on 5 further flights throughout

August and September 2017 (Table 2). FAAM–LASIC intercomparisons took place at nominally the same altitude as the ARM
site with the FAAM BAe-146 operating between 2 and 4 km offshore and upwind of the LASIC observation site.

We offer the results of this study as a "transfer standard" upon which other comparisons and scientific conclusions can be
baselined. A key aim is to provide comparisons of parameters that are required to determine aerosol optical, physical, and
chemical properties, cloud microphysics, atmospheric radiation, and tracers for airmass characterisation.

The following section provides an overview of the instrumentation from each platform that is considered in this
intercomparison. Section 3 describes the methods employed in executing the intercomparisons and the processing of resulting
measurement data. Results presented in Sect. 4 are discussed in Sect. 5. Conclusions are presented in Sect. 6.

2 Instruments

A brief introduction follows for each of the instruments and inlets under study here along with the calibration procedures
undertaken. When multiple instruments providing a given measurements were available on a particular platform, we chose to
focus primarily on what would be considered the standard, routine data product. However, in some cases, datasets are included
from supplementary instruments where this proves informative. We provide sufficient information for the reader to understand
instrument operation and its installation configuration on the platform and the reader is directed to the references provided for
full descriptions of instrumentation characteristics. Parameters depending on sample concentration or flow rates, such as
particulate measurements and gas concentrations, are converted to Standard Temperature and Pressure (STP) conditions of
273.15 K and 1013.25 hPa. Timing offsets between instruments, introduced for example by flow-rate offsets, were first
corrected for.

2.1 Particle and gas inlets

Gas samples were drawn into the BAe-146 aircraft through dedicated whole-air sample pipes and samples containing aerosol
particles were drawn into the aircraft through modified Rosemount Aerospace Inc. Type 102 Total Temperature Housings,
which while aspirated, operate a sub-isokinetic flow-velocities. The Rosemount inlets are mounted in pairs at three locations
towards the front of the aircraft, the inlets in each pair offset from one another to avoid interference. The EXtinction SCattering
and Absorption of Light for AirBorne Aerosol Research rack (EXSCALABAR) (Sect. 2.52) of instrumentation was fed by the
Rosemount pair located above the starboard doorway towards the front of the aircraft. The Single Particle Soot Photometer
(SP2) (Sect 2.41) took its feed from the other of this forward-starboard Rosemount inlet pair. The Aerosol Mass Spectrometer
(AMS) rack (Sect. 2.42), which includes a Scanning Mobility Particle Sizer (SMPS) was fed from the lower Rosemount pair
on the port side. On the port-side of the FAAM BAe-146 is a blister-pod that houses large radiometers. This feature sits just
upstream (in terms of airborne streamlines around the fuselage) of the Rosemount particle inlets for AMS, SMPS and the
condensation particle counter (CPC), and may provide a potential barrier to the airflow and shadow a certain portion of the
particle size distribution. However, the transmission efficiency for submicron low density aerosols (i.e., not dust) has been
demonstrated to be close to unity for individual Rosemount inlets (Trembath et al., 2012, Trembath, 2013) with good agreement
between two pairs of Rosemount inlets on the port side of the aircraft.

Aerosol particles were brought into the P3 through the Solid Diffuser Inlet (SDI) which was operated isokinetically with the
flow rate matched to external airflow velocity to within 5 % (Dobracki et al., 2021). The inlet has been shown to efficiently
transmit particles at dry diameters up to 4.0 μm (McNaughton et al., 2007) with good agreement for submicron sized scattering
aerosols. Internal pipework was designed to minimise transport losses to a negligible level for particles up to 4.0 μm, using
open-source software from Baron (2001) although additional complications associated with airborne sampling mean that not
all losses may be well accounted for, and differences may exist owing to different flow rate and pathways to different
instruments (Dobracki et al., 2021).

Aerosol sampling during LASIC at the ARM facility on Ascension Island took place within shipping containers fed by a
centrally located community inlet at the top of a 10 m mast and delivered to a 5-way distribution port through a 2" polished
stainless steel pipe. This nominally transmitted aerosols as large as 10 μm (PM10) but a selectable impactor was used

periodically to select only those particles smaller than 1 µm (PM1) (at 50 % efficiency) (Uin et al. 2020). The latter data stream is available only to the nephelometers.

2.2 Meteorological parameters

135   On the FAAM BAe-146, aircraft position and attitude are provided by an Applanix POS AV 410 Global Positioning System aided Inertial Navigation System with static pressure taken from the aircraft's Air Data Computer (BAe Systems 2000). Vertical wind data were produced by combining data from pressure sensors in a nose-mounted 5-port turbulence probe and aircraft position and attitude data, recorded at 32 Hz, and analysed here at 1 Hz (Barrett et al., 2020). Temperature was provided by a Rosemount Aerospace Inc. Type 102 non-de-iced total temperature housing fitted with an open-wire platinum resistance

140   thermometer sensing element located on the nose-cone of the aircraft. Temperature data were reported at 32 Hz, averaged to 1 Hz. The uncertainty in temperature was computed by combining in quadrature the uncertainties associated with sensor drift, the data acquisition system, the calibration standard itself and the digital voltmeter used in the calibration. For flight C031 (Sect 3.1) non-de-iced temperature sensors uncertainties were smaller than 0.4 K.

Humidity data were recorded by a Buck Research Instruments CR2 Chilled Mirror dew-point hygrometer with heated inlet
145   (Price et al. (2022). The Buck CR2 has computed in-flight uncertainty in dew point temperature (when conditions were suitable) of a mean value of 0.2 K, with 99 % of values below 1.0 K. When converted to water vapour concentrations the uncertainty was below 2 % across the range encountered during the intercomparison flight. Whilst this humidity sensor is stable and calibrated to traceable standards it is combined with a tunable diode laser (TDL) hygrometer where faster response measurements are required. The TDL, a Water Vapor Sensing System (WVSS-II, SpectraSensors), recorded data at 0.4 Hz
150   which was linearly interpolated to 1 Hz, fed by the standard flush mounted inlet as described by Vance et al. (2015). The wet-bias noted by Vance et al. (2015) was subsequently shown not to result from the performance of the flush-mounted inlet (Vance et al., 2018) which is expected to perform well in the humidity range encountered during the measurements in this study. The WVSS-II is an absolute measure of water vapour concentration with an uncertainty of ±5 % (above a minimum of ±50 ppmv) (Vance et al., 2015), but the sample-cell temperature and pressure are not known and so data are subject to unknown
155   uncertainties. Therefore, data were first baselined against the Buck CR2 to known good data using the method detailed in Price et al. (2020). This WVSS-II data product is deemed the primary humidity measurement provided by FAAM, in part due to the combination of a stable calibrated sensor, the Buck CR2 and the faster response time of the WVSS-II TDL sensor.

On the NASA P3, a Honeywell Sperry AZ-800 air data system provided static pressure, pressure altitude, and true airspeed with aircraft position, attitude, ground speed, and vertical speed coming from a Universal Avionics UNS-1Fw (NASA
160   Handbook, 2010). Vertical wind data were provided by this system and reported at 1 Hz, where the uncertainty was ±0.15 ms^{-1}. The magnitude of the vertical wind velocities and the fluctuations about the run mean values were interrogated. Total air temperature was provided by a Rosemount 102 type non-deiced probe with a manufacturer reported uncertainty of approximately 0.35 K over 1 second. Water vapour concentrations were measured with a Picarro L2120-i (total water vapour concentration #2: Tot2) fed from the SDI (Pistone et al., 2021), with a similar measurement of ambient water vapour
165   concentrations made by a second Picarro L2210-i instrument (total water vapour concentration #1: Tot1) fed from the Counterflow Virtual Impactor inlet (CVI) when out of cloud. These two measurements are part of the "WISPER" system. A Los Gatos Research 23r (the P-3"COMA" instrument, see Sect. 2.3) is also fed from the SDI and provides additional independent water vapour measurements Comparisons during ORACLES-2016 showed good comparability between the COMA and WISPER systems, with the slope of linear regressions within 2 %, with COMA detecting slightly higher
170   concentrations in general, although lower concentrations at altitudes greater than 1.3 km. The airborne humidity instruments under test here reported values of vmr with NASA operating the WISPER Tot2 as the primary instrument. WISPER Tot1 is employed as a support measurement (it sometimes made cloud measurements from the CVI inlet) along with the COMA instrument (which also measured CO). All three are considered here.

LASIC ARM site observations of temperature, pressure, and relative humidity (RH) were supplied from a Vaisala Weather
175   Transmitter WXT520B (Campbell Scientific) at a frequency of 1 Hz. Measurements of temperature were obtained using a capacitive ceramic THERMOCAP® sensor with manufacturer quoted instrumental accuracy of ±0.3 K and RH with a HUMICAP® thin-film polymer sensors accurate to ± 3% RH (below 90 % RH).

2.3 Gaseous constituents

Carbon Monoxide (CO) concentrations from the FAAM aircraft were provided by an inboard Core Aero Laser GmbH model
180 AL5002 VUV resonance fluorescence spectrometer (Gerbig et al., 1999). The instrument was calibrated periodically during
flights with reference gases with CO = 500 ppb and CO = 0 ppb. Concentrations are reported at STP.

CO concentrations onboard the NASA P3 were provided with a gas-phase $CO/CO_2/H_2O$ Analyzer (ABB/Los Gatos Research
$CO/CO_2/H_2O$ Analyzer (907-0029)) modified for aircraft use and referred to as the "COMA" system. The analyser uses a
patented Integrated Cavity Output Spectroscopy (ICOS) technology to make stable cavity-enhanced absorption measurements
185 of CO, CO_2, and H_2O in the infrared spectral region. The instrument reports mixing ratio (mole fraction) at a 1 Hz rate based
on measured absorption, gas temperature, and pressure using Beer's Law The technology has been demonstrated to operate
with a precision of 0.5 ppbv if averaged over 10 s on other airborne research platforms (Liu et al., 2017). Quoted uncertainty
for CO is 6 % $\pm$ 1 ppb. Altitude dependent sample-line timing offsets were corrected for. Concentrations are reported at STP.

Likewise, the instrument responsible for CO concentrations at the LASIC ARM site was a Los Gatos Research instrument,
190 with a quoted uncertainty on the measurement of $\pm$ 2 ppb, and concentrations reported at STP.

Ozone concentrations on the BAe146 were provided by an inboard Core Thermo Fisher Scientific Inc. model 49i UV
absorption ozone photometer with a manufacturer quoted instrumental uncertainty of 1 % $\pm$ 1 ppb. Concentrations are reported
at STP. NASA ozone measurements were made with a 2B Technologies Model 205 instrument and reported at STP, with an
uncertainty of 6 % $\pm$ 1 ppb. The LASIC ozone measurements were provided by a Thermo Fisher Scientific Inc. model 49i UV
195 absorption photometer with uncertainty of $\pm$ 2 ppb (or 5 % whichever is greater) and reported at STP.

2.4 Aerosol composition

2.4.1 Black carbon particulate matter

The FAAM BAe-146 flew an SP2 instrument manufactured by Droplet Measurements Technologies Inc. (DMT) to monitor
black carbon number (rBC_n) and mass concentrations (rBC_m) (Schwarz et al., 2006). The SP2 detects refractory black carbon
200 (rBC) for particles between ~80 and 500 nm volume equivalent diameter (assuming rBC density of 1.8 kg m^{-3}). The instrument
was located on the starboard side of the aircraft behind a Rosemount inlet (Taylor et al., 2020). Calibrations were performed
using nebulised mass-selected Aquadag (using a centrifugal particle mass analyser) and corrected by a factor of 0.75 as
recommended by Laborde et al. (2012). An SP2 was also installed at the LASIC ARM site with this instrument calibrated
using fullerene following Laborde et al. (2012) and Gysel et al. (2011) giving accuracy of 10 % and precision of 30 %
205 (Sedlacek, 2017). Concentrations are reported at STP.

The NASA P3 SP2 instrument was affected by a leak on the supply rack during the part of the flight immediately before the
intercomparison segments and so data are compromised. Nonetheless, data are presented in Supplement Sect. 5 for
completeness. The P3 instrument was calibrated in the same manner as the one at the ARM site and is expected to be of good
210 quality at other times in the ORACLES campaign. The installation location was on the front rack some 8 m behind the SDI
inlet.

2.4.2 Aerosol mass spectrometers

The FAAM BAe-146 flew an Aerodyne Compact Time-of-Flight Aerosol Mass Spectrometer (AMS) (Aerodyne Research Inc,
Billerica, MA, USA) (Drewnick et al., 2005), to measure the chemical composition of non-refractory aerosols in the 50 nm to
215 600 nm vacuum aerodynamic diameter range. According to Morgan et al. (2009) for a particle of density of 1600 kg m^{-3}, 600
nm equates to an upper mobility diameter of 440 nm. Morgan et al. (2009) describe the operation of the AMS on the FAAM
aircraft, including calibration and corrections while Wu et al. (2020) outline its use during CLARIFY.. The aerosol samples
entered the aircraft through a modified Rosemount inlet on the port side of the aircraft above the radiometer blister. Data were
processed using the SeQUential Igor data RetRiEvaL, v.1.60N (Allan et al., 2003, 2004) algorithm (SQUIRREL) to return unit
220 masses of ion fragments in the mass-charge (m/z) range 10-500 (Wu et al., 2020) and corrected to STP. The AMS was

calibrated using monodisperse ammonium nitrate, and the relative ionisation efficiencies (RIE) of ammonium and sulphate were calculated by varying concentrations of ammonium nitrate and ammonium sulphate. The RIE of sulphate was found to be 1.0834, while the RIE of ammonium was 4.0516. Organics and nitrate RIE were kept as the SQUIRREL defaults of 1.4 and 1.1 respectively. Limits of detection for species were (all at STP): 0.3 µg m^{-3} (organics), 0.1 µg m^{-3} (sulphate) and 0.03 µg m^{-3} (nitrate and ammonium).

The NASA P3 flew a high-resolution time-of-flight AMS (HR-AMS), also manufactured by Aerodyne Research Inc. (Dobracki et al., submitted). Particles between 70 and 700 nm vacuum aerodynamic diameter were analysed with the AMS peaks processed using the Particle Integration by Key v.1.16 (PIKA) algorithm (deCarlo et al., 2006). The nitrate ionization efficiency values for the HR-AMS centred on 1.31×10^{-7}, with a nominal 10 % uncertainty assigned to it following Bahreini et al. (2009). The ionization efficiencies for ammonium, sulphate, and organics relative to those for nitrate are thereafter determined within SQUIRREL as: 4 for ammonium; 1.1 for measured nitrate relative to the calibration value; 1.2 for sulphate; and 1.4 for organics, following Jimenez (2009). Overall uncertainties for components of the composition are between 33 and 37 % (Dobracki et al., submitted). The instrument sat 8 m downstream of the SDI. Sampling transit times of 6 s due to pipework transit times were accounted for by comparison to with wing-mounted Passive Cavity Aerosol Spectrometer Probe (PCASP, Sect 2.6) measurements. Cloud shatter events were screened out by considering number concentrations of (nominal) 10 µm sized cloud particles from a wing-mounted Phase Doppler Interferometer cloud microphysics probe (Chuang et al., 2008), including screening of data from 10 s post-event. Concentrations are reported at STP. The limit of detection for organics was 0.15 µg m^{-3}, 0.03 µg m^{-3} for sulphate, 0.04 µg m^{-3} for nitrate and 0.01 µg m^{-3} for ammonium.

During CLARIFY, a time- and composition-dependent collection efficiency (CE) was applied to the data based on the algorithm by Middlebrook et al. (2012). The collection efficiency (CE) for each airborne AMS during the airborne comparisons was 0.5. This was demonstrated in the free troposphere for ORACLES data (Dobracki et al., submitted) and for the CLARIFY boundary layer and free troposphere measurements more relevant to the region of these tests (Fig. S3). Differences between the SQUIRREL and PIKA algorithms only accounted for 7 % differences between estimates of sulphate mass concentrations (Supplement Sect. 4).

LASIC operated an Aerodyne Aerosol Chemical Speciation Monitor (ACSM) to measure mass loading and chemical composition of non-refractory aerosol particles in real-time with data taken from the C2 dataset. The aerosol size range spans 40 nm to 1 µm vacuum aerodynamic diameter. The ACSM was calibrated against a dedicated Scanning Mobility Particle Sizer (SMPS) both before and after the LASIC campaign, with an in-field calibration procedure that is based on the constant presence of peaks at mass-charge ratio, m/z = 28, resulting from nitrogen. Composition dependant collection efficiency was unity on all comparison days, at the closest time point, but not for all days during the preceding or subsequent hours. Once the correct collection efficiency is applied, the ACSM can obtain mass concentrations of particulate organics, sulphate, nitrate, ammonium, and chloride to within a detection limit <0.3 and <0.2 µg m^{-3} for organics and nitrate respectively, for 30 min of signal averaging (Ng et al., 2011). Results are presented for the closest 30 min sample to the FAAM fly-past, with the range given as the standard deviation for the timespan one hour before and after. Data were not available for 5th September. The relative proportions of the various aerosol species is approximately correct to within the instrument uncertainty - overall accuracy is ± 30 % (Watson, 2017).

2.5 Aerosol optical properties

2.5.1 NASA P3 nephelometer and PSAP

Aerosol optical properties on the P3 were obtained by measuring optical scattering coefficients (σSP) with a TSI 3563 Nephelometer and optical absorption coefficients (σAP) with a Radiance Research tri-wavelength Particle Soot Absorption Photometer (PSAP). The PSAP measured σAP at 470 nm (blue), 530 nm (green) and 660 nm (red). Data were corrected as per Pistone et al. 2019 following the method of Virkkula (2010) (further details in Sect. 11.2). This has been shown to provide a good level of correction for BBA over the south east Atlantic region, mitigating against the impacts of scattering and absorption artefacts on the filter-based measurement (e.g., Davies et al., 2019). The instrument optics were heated to 30°C during the 2017 ORACLES campaign resulting in a "dried" sample while minimising vaporisation of volatile components. Errors of 0.5 Mm-1 remain when averaging for 240 to 300 seconds, as shown by McNaughton et al. (2009, 2011). The limited

sampling time of ~120 s available in this work and low aerosol concentrations encountered will result in larger errors. The particular unit employed here was the "rear" instrument as the "front" instrument suffered problems during sampling.

270   A TSI 3563 Nephelometer recorded σ_{SP} at 450 nm (blue), 550 nm (green) and 700 nm (red) wavelengths, corrected according to Anderson and Ogren (1998). Blue and red channel data were then interpolated to 470 nm and 660 nm respectively using an interpolation based on linear regression between the logarithms of scattering optical depths ($\tau_0(\sigma_{SP})$ and $\tau_1(\sigma_{SP})$) and wavelengths (λ_0 and λ_1) (Eq. 2). First the scattering Ångström exponent, $\mathring{A}_{SP}$, was derived from observations at the native wavelengths, prior to use of Eq. 2 again to determine scattering at the desired wavelength for amalgamation with PSAP data. Calibrations were performed in-the-field with refrigerant R-134A (1,1,1,2-tetrafluoroethane). RH data are measured within the
275   nephelometer but outside the sensing chamber so estimates of sample RH are made by using laboratory calibrations to correct the real-time data. During boundary layer sampling, the RH was above 60 % and often at the threshold maximum reported value of 70 % (not shown). Overall uncertainty is of the order 10 % when averaged over 240 s, so errors at the shorter comparison times available for this study will be greater than this. The optical extinction coefficient (σ_{EP}) was computed from the sum of the nephelometer-measured σ_{SP} and PSAP-measured σ_{AP} at 470 nm and 660 nm wavelengths using Eq. 1. Note,
280   that humidity may be different in each instrument.

$$\sigma_{EP} = \sigma_{SP} + \sigma_{AP} \qquad\qquad (1)$$

$$\mathring{A}_{AP,SP,EP} = \log\left(\frac{\tau_0^{(\sigma_{AP,SP,EP})}}{\tau_1^{(\sigma_{AP,SP,EP})}}\right)\bigg/\log\left(\lambda_0\big/\lambda_1\right) \qquad (2)$$

Flow supplied to aerosol optical instruments on the P3 was from the port side SDI at 30 L min^{-1} and switched through either a PM1 impactor or direct through the PM10 (nominal) sampling line. Data are presented following correction of flowrates to
285   STP. Timing offsets were corrected for by comparing against aerosol particle measurements from a wing-mounted outboard PCASP (Sect. 2.6). Although data are output at 1 Hz, the effective sample temporal resolution is 6 seconds, and data are first smoothed with a 10 s moving average to reduce the impact of additional transit pipework to the rear PSAP instrument and to facilitate comparison with other instruments under test. Periods where shattering of cloud particles may have degraded the quality of the P3 measurements were removed by consulting liquid water content (LWC) data from a King hot-wire probe and
290   cloud particle number concentration data from a cloud droplet probe (CDP: Sect. 2.6).

2.5.2 FAAM BAe-146 EXSCALABAR

FAAM flew state-of-the art instrumentation for measurement of aerosol optical properties: EXtinction SCattering and Absorption of Light for AirBorne Aerosol Research (EXSCALABAR). The bespoke instrument was developed by the Met Office and University of Exeter for use on the BAe-146 aircraft (Davies et al., 2018a, 2019). Cavity ring-down spectroscopy
295   (CRDS) (Langridge et al., 2011) was employed to measure σ_{EP} and photo-acoustic spectroscopy (PAS) (Davies et al., 2018a, 2019) to measure σ_{AP}. CLARIFY was the first major campaign for EXSCALABAR following initial work during the Methane Observations and Yearly Assessments (MOYA) experiment (Allen et al., 2017, Wu et al., 2021), which comprised a limited number of flights sampling West-African BBA close to the source of emissions.

The instrument racks are located towards the front of the BAe-146 on the starboard side, supplied by a Rosemount aerosol
300   inlet. The 8 L min^{-1} total sample flow first passed through a Nafion™ dryer (Permapure, PD-200T-12-MSR) and a custom-built activated carbon "honeycomb" scrubber to remove ozone and NO$_x$. The sample then passed through a custom-made impactor (Brechtel Manufacturing Inc.) with nominal aerodynamic diameter cut size: D_{50}, 1.3 µm (50 % of particles of this diameter are captured). All EXSCALABAR sampling occurred with the impactor in line. Custom built splitters then feed 8 parallel 1 L min^{-1} sample lines. Transmission losses between the instrument inlet and sample cells (i.e., through the sample
305   conditioning) have been characterised and corrected for as have time lags between measurement cells. Data were corrected to STP. Transit through the airflow system and detection cells results in an effective temporal resolution of 6 s and here 1s reported data are smoothed using a 10 s moving average prior to further analysis and for direct comparability with measurements from P3.

Dry σ_{EP} (RH below 10 %) are provided by CRDS channels for blue (405 nm) and red (660 nm) wavelengths (Davies et al.,
310   2018a). Given aerosol loadings between 10 and 100 Mm^{-1}, the measurement precision dominates total extinction uncertainty.

The precision of 1 Hz data has been characterised in ground-based tests from Allan-Werle deviation analyses as being better than 0.4 Mm^{-1} for the CRDS spectrometers used in this work. Assessments of the CRDS measurement accuracy demonstrated that the measured aerosol extinction cross sections are within 3.6 % of expected values (Cotterell et al. 2020); indeed, this excellent accuracy is expected given that CRDS is a direct, calibration-free approach to aerosol optical property
315 characterisations and is not subject to the artefacts that degrade characterisations from nephelometry or filter-based approaches.

Dry σ_{AP} at 405 nm (blue), 515 nm (green) and 660 nm (red) wavelengths is measured by PAS. A blue and red PAS cells are each positioned in-series downstream of the blue and red dry CRDS cells. The green dry PAS cell operates in parallel with these blue and red sample lines. The PAS cells were calibrated either before or after each flight using ozone at concentrations determined using the CRDS cells (Davies et al., 2018a). Calibrations were stable throughout the campaign for all channels
320 except PAS red dry for which the optics were adjusted slightly mid-campaign. For all except the PAS red dry cell, an average of all calibrations was applied to for each flight. For the red dry channel, calibrations before and after the adjustment were averaged and applied to all flights during their respective periods. Various pressure dependencies were corrected for using methods described by Cotterell et al. (2021).

Measurements of the aerosol-free background are required for both CRDS and PAS data analysis. A filtered-air stream is
325 passed through the sample chambers and the response measured for ~45 seconds every 10 minutes during flight with additional background measurements following large pressure (i.e., altitude) changes. From these filtered-air measurements, background corrections were determined. Absorption coefficients encountered during the intercomparison flight were low. As such, they were especially sensitive to variations in acoustic background signal that occurred. Absolute measurement uncertainties (i.e., the combined uncertainties associated with measurement sensitivity and sources of bias) in the range 8 to 55 % can be achieved
330 with the upper end of absolute uncertainty corresponding to the limit of absorption tending to 1 Mm^{-1} (Davies et al., 2019). The background signal varies with pressure. During this campaign, it was also affected by recent previous exposure to BBA which complicated the derivation of a background signal. The cell design has subsequently been improved to minimise this effect (Cotterell et al., 2019a, 2019b).

For comparison with P3 data, the values of σ_{EP} and σ_{AP} from the blue (405 nm) EXSCALABAR channels were interpolated to
335 a common wavelength of 470 nm, to avoid extrapolation of data outside of any instruments sampled range of wavelengths. This is done for σ_{EP} and σ_{AP} by determining the Extinction or Absorption Ångström Exponent (Å$_{EP}$, Å$_{AP}$) between the red and blue CRDS cells and blue and green PAS cells (Eq. 2), before interpolating the 405-nm CRDS data to the 470 nm wavelength using Eqn. 2. The red cell wavelength of 660 nm already matches that of the P3 PSAP. Absorption Ångström Exponent, σ_{AP}, was computed using Eq. 2 for all combinations of wavelength pairs.

340 A TAP (Tri-wavelength Absorption Photometer) was also installed in parallel with EXSCALABAR's PAS cells and has previously been used to compare absorption instrument filter-based correction schemes (Davies et al., 2019). This filter-based technique operates at wavelengths of 476 nm (blue), 528 nm (green) and 652 nm (red) and was subjected to the same sample conditioning as the sample entering the PAS cells. Data are presented here after undergoing filtering and processing as described by Davies et al. (2019) which provides σ_{AP} at a sampling rate of 30 s (which is a longer averaging time than used for
345 other measurements in this paper), and as they are supplementary data are left at the native wavelengths. Data were corrected to STP. Here, we take data from the airborne intercomparison for more direct comparison with the filter-based measurement onboard the NASA P3 and utilise the Virkkula (2010) corrected data. Absorption Ångström Exponent, σ_{AP}, was computed using Eq. 2 for all combinations of wavelength pairs.

2.5.3 LASIC ARM site nephelometer and PSAP, and CAPS PM$_{SSA}$

350 Aerosol laden air samples entered the LASIC cabin through the roof mounted inlet. Scattering observations took place using a TSI 3563 nephelometer which reported at 450 nm (blue), 550 nm (green) and 700 nm (red) wavelengths. The sample was not actively dried but the RH of the sample in the measurement cell was estimated to be between 45 % and 60 % (Zuidema et al. 2018a – supporting information). Data were corrected according to Anderson and Ogren (1998). Prior to use in this study the data from blue and red channels were interpolated to 470 nm and 660 nm, the native wavelengths of the PSAP. Dilution of
355 the sample stream was accounted for and data were reported at STP.

A Radiance Research tri-wavelength PSAP measured σAP at 464 nm (blue), 529 nm (green) and 648 nm (red). The wavelengths differed from those detailed in Sect 2.5.1 for NASA P3 (470, 530 and 660 nm) because they had been empirically determined with an Ocean Optics grating spectrometer registered to a mercury pen lamp (Springston 2018a). The sample was actively dried by a Nafion(TM) dryer and further dilution with a clean, dry airstream occurred. Whilst the RH was not
360 measured, it is estimated to be below 25 % (Zuidema 2018a – supporting information). PSAP data were constructed as the average of the Ogren (2010) corrections and Virkkula (2010) wavelength averaged corrections. Flow rate was calibrated against a Gilibrator instrument and measurements corrected to STP. Prior to use in this study the data from blue and red channels were interpolated to 470 nm and 660 nm to be comparable with data from the aforementioned spectroscopy instruments.

365 A Cavity Attenuated Phase Shift Single Scattering Albedo (ω_0) (CAPS PM$_{SSA}$) monitor operating at a wavelength of 530 nm was deployed on Ascension from August 4 to September 22, 2017, overlapping with the CLARIFY time period, for the express purpose of assessing the filter-based LASIC ω_0 calculation. The CAPS PM$_{SSA}$ monitor provides a direct measurement of the particle single scattering albedo by simultaneously measuring σ_{SP} and σ_{EP}, calculating ω_0 from their ratio. Absolute particle extinction is measured using the cavity attenuated phase shift technique, and particle scattering is derived from the light
370 collected using an integrating sphere within the same optical path (Onasch et al., 2015), with absorption calculated from the difference. The total extinction was calibrated at Aerodyne prior to LASIC using 600 nm diameter polystyrene latex (PSL) particles, and another calibration was done in the field on August 20, 2017. The scattering was calibrated to the extinction for white (non-absorbing) particles (by definition, ω_0=1.0). A 2 % truncation correction was applied to the scattering channel, based on Ultra High Sensitivity Aerosol Probe (UHSAS) size distribution data. The uncertainty in the ω_0 measurements is
375 estimated at ±0.03 (Onasch et al., 2015). Early assessments found excellent agreement (within 1 %) between the PSAP and CAPS PM$_{SSA}$ absorption measurements, with the nephelometer scattering exceeding the CAPS PM$_{SSA}$ scattering measurements (within 10 %). The monitor sampled from both the PM1 and PM10 inlets. The CAPS PM$_{SSA}$ measured from the same inlet as the UHSAS and PSAP, behind the nephelometer, which measured air with a relative humidity of 46-65 %. Here we use the data to estimate σ_{AP} by inputting the measured quantities into Eq. 1.

380 **2.6 Aerosol and cloud microphysical and bulk properties**

Total aerosol particle number concentrations in the form of measurements of Condensation Nuclei (CN) particle number concentrations were provided on all three platforms by CPC instruments. The NASA P3 flew a TSI 3010 instrument, which has a nominal lower size threshold of 10 nm. Uncertainty in concentration of 5 % is primarily due to flow rate uncertainty. Data are multiplied by a constant factor of 1.02 following laboratory intercomparisons with other TSI 3010 CN counters used
385 in the ORACLES campaign. Data are reported at STP. Onboard the BAe-146 was a TSI 3776 with a lower size threshold of 2.5 nm and 5 % flow rate uncertainty. LASIC used a TSI 3776, an ultrafine CPC with a lower size threshold of 2.5 nm, which was operated without dilution flow.

Both FAAM and LASIC had access to Scanning Mobility Particle Sizer (SMPS) data which provided aerosol particle number concentrations for fixed particle mobility diameter. In the case of LASIC a TSI 3081 Differential Mobility Analyser (DMA)
390 associated with a TSI 3080 column supplied a full scan of data at 5 minute intervals following a 260 s scan period. The instrument was located behind an impactor with D$_{50}$ = 700 nm and has a lower size threshold of 10 nm. FAAM data were provided by a similar system with a TSI DMA 3081 connected to a TSI CPC 3786 (Wu et al., 2020) and reported particle mobility diameter in the size range 20 nm to 350 nm. An empirically determined collection efficiency factor of 1.8 is applied to reduce the concentrations from the BAe-146 SMPS which has been demonstrated to achieve good overlap with the externally
395 mounted PCASP instruments during CLARIFY (Wu et al. (2020)).

UHSAS's were operated by both LASIC and NASA (located within the aircraft). These instruments have been shown to undersize particles where BBA are present (Howell et al., 2020). The high power laser modifies the measured size distribution through heating and evaporation of brown carbon thus reducing particle size at the time of measurement. Reductions (up to 35 %) were observed for the larger particles of rBC. NASA P3 data are first corrected using the power-law introduced by Howell
400 et al. (2020) which scales the default bin dimensions to be closer to mobility diameters as determined real-time in-flight by size selecting particles with a DMA. Here we use the NASA P3 data for comparison with the outboard FAAM BAe-146 PCASPs.

FAAM and NASA flew wing-mounted DMT PCASPs (Lui et al., 1992) with SPP200 electronics (DMT 2021) which were exposed to the free airstream. NASA operated a single unit located in the inner position of the inner pylon located under the
405 port wing. FAAM flew two units mounted externally: PCASP1 and PCASP2. A third probe, PCASP3 (also with SPP200 electronics) was located within the fuselage as part of the EXSCALABAR suite of instruments, fed by a Rosemount inlet. PCASPs measure aerosol particle sizes in 30 channels in the nominal size range 0.1 μm to 3 μm optical diameter (polystyrene latex sphere (PSL) equivalent). Data are reported at a frequency of 1 Hz. Concentrations from the NASA PCASP channels were calibrated in the laboratory by comparison with an SMPS and a scaling factor applied to certain channels to ensure
410 comparability. For all PCASP's, channels that bracket gain-stage crossovers were merged following the method in Ryder (2013) and the smallest size bin was rejected as the lower size threshold is unbounded, resulting in 26 usable channels. Errors are comprised of Poisson counting uncertainties and flow rate errors, assumed to be 10 %, with both combined in quadrature. The air intake of an external PCASP is designed to decelerate the particle flow, with the resulting ram air causing sample heating and some reduction in RH of the sample compared to ambient which may affect particle size. The inboard BAe-146
415 PCASP sample was subjected to the same conditioning as that for EXSCALABAR cells - most notably dried to < 10% RH and behind the impactor – and adjusted for transmission losses through that conditioning section.

Data for externally-mounted PCASPs for the airborne comparisons are presented in manufacturer nominal bin dimensions and no adjustment has been made for the absorbing characteristics of BBA laden airmasses. All external instruments are sampling the same material without the complication of inlets, and so when instrument are employing the same measurement technique,
420 i.e., optical detection, this should not impact the results of this comparison. Comparisons with the NASA UHSAS should be approached with caution as this instrument is effectively calibrated to particle mobility diameter. The internally-mounted FAAM PCASP3 is compared against the outboard PCASP2 and against the internally-mounted SMPS instrument (which measures mobility diameter). The purpose of this comparison is, in part, to assess the performance of the Rosemount inlets and transmission loss corrections. A refractive index (RI) correction was applied to the nominal bin boundaries for PCASP2
425 (outboard) and PCASP3 (inboard) using the observationally derived value of 1.54-i0.027, appropriate for the BBA laden airmasses (following Peers et al. (2019)). This correction was applied to bin boundaries for diameters smaller than 800 nm. Differences between the nominal and BBA bins were as large as 25 % for the smallest bin but typically 10 % for particle diameters smaller than 800 nm. At sizes larger than this, the nominal bin dimensions (at PSL equivalent RI) were used.

Both aircraft operated Cloud Droplet Probes (CDP) (Lance et al., 2010) which detect and size cloud particles in the size range
430 3 to 50 μm diameter in 30 particle size bins. The FAAM BAe-146 instrument was located on the inner-lower position of the port pylon and the NASA P3 instrument was located on the outer location of the outer port pylon. The pylon holding the CDP during ORACLES 2017 and 2018 was further ahead and lower relative to the aircraft wing compared to the pylon used in ORACLES 2016. These forward scattering probes have size bins defined using the RI for water of 1.33. The CDP on the NASA P3 used the manufacturer default sample area of 0.26±0.05 mm^2 and optics collection angle 4° to 12°. The sample area
435 of BAe-146 CDP has been experimentally determined by DMT as 0.252±0.05 mm^2 with the collection angle for the optics found to be 1.7° to 14° (after Lance et al., 2012). BAe-146 CDP performance was observed to be stable throughout the campaign as monitored through daily pre-flight, glass bead calibrations. A linear fit between the median calibration response to these daily tests showed that the BAe-146 CDP with nominal bin dimensions under-sized cloud particles ~7 %. This linear fit was applied to the nominal bin boundaries (Supplement Sect. 3). Nominal bin dimensions applicable to BAe-146 and P3
440 CDPs along with calibrated bin dimensions for BAe-146 are given in Table S1. Gupta et al. (2021b) compared data from the P3 CDP against that collected by a cloud and aerosol spectrometer (CAS) also installed on the P3, concluding that the CDP provided data most consistent with bulk water contents measured by a King probe and less than calculated adiabatic water contents. Errors are comprised of Poisson counting uncertainties, true airspeed uncertainties assumed to be 5 %, and sample area uncertainty of 5 %, all combined in quadrature.

445 Larger cloud particles and drizzle drops were sampled on both aircraft using Stratton Park Engineering Company (SPEC) 2DS Optical Array Probes (OAP) (Lawson et al., 2006), which measure the sizes of particles between 10 μm and 1280 μm as they cast shadows on a 128 element charged-coupled-device (CCD) array illuminated by a laser. FAAM BAe-146 OAP data were processed using the Optical Array Imaging Software (OASIS) software package (Crosier et al., 2011, Taylor et al., 2016) and presented at native bin resolution of 10 microns. P3 data were processed using the University of Illinois/Oklahoma Optical
450 Array Probe Processing Software (McFarquhar et al., 2018) as described by Gupta et al. (2021a). Errors in channel

concentrations were estimated by combining Poisson counting uncertainty values and size-dependent sample volume uncertainties in quadrature.

Bulk condensed water properties on FAAM were measured with a Nevzorov hot-wire probe (Abel et al. 2014). Bulk water content onboard the NASA P3 was identified with a King hot-wire probe (King et al. 1981, Strapp et al. 2003). LWC derived
455 from the Picarro L2120-i hygrometer (Sect 2.3) fitted downstream of the Counterflow Virtual Impactor inlet (CVI) was used to determine when the NASA P3 was in cloud free conditions by locating times when the bulk water content was determined to be zero. Closure tests between the LWC derived from the P3 cloud probe spectra and the King hot-wire were conducted for in-cloud measurements from each ORACLES deployment (Gupta et al., 2021b).

When out-of-cloud, the CDP from BAe-146 and the 2DS probes from both platforms were used to measure the coarse mode
460 aerosol particle size distributions and identify the presence of supermicron aerosol particles (Miller et al., 2021). However, CDP data from the NASA P3 were masked-out during the cloud sampling leg.

The altitude of the ARM site at 341 m above mean sea level was low in the boundary layer, and always below cloud base.

2.6.1 Derived microphysical parameters

Aerosol (corrected to STP) and cloud particle number concentrations per size channel (N(i)) were reported at 1 Hz from
465 microphysics probes. Particle size distributions (PSD) as a function of particle diameter N(D) were computed from these data using Eq. 3. For CDP and 2DS the individual channel concentrations were scaled by the size dependant sample volume (SV(i): Eq. 3.1) which is a function of the sample area (SA(i)) and the aircraft true airspeed (TAS). For PCASP and UHSAS the sample volume is internally determined by the sample flow rate and is uniform across size channels. Aerosol (N_a) and cloud drop (N_c) number concentrations were generated using Eq. 4 by summation of the individual discreet channel concentrations,
470 excluding the smallest size channel, which is susceptible to electrical noise and has an unbounded lower size threshold. This results in the smallest reported bin edge of diameter (D) greater than 3 μm for the CDP and greater than 105 nm for the PCASP. Count median diameters of the particle size distributions were computed as the diameter where 50 % of the observations were above and below the given size. Effective radius (R_e) and mean volume radius (R_v) were computed for individual probes by summation across the particle size channels using Eqs. 5, 6. For aerosol observations this was done for the accumulation mode
475 only, by selecting only particles smaller than 800 nm (PSL equivalent) to compare probe performance in the optically important BBA mode (e.g., Peers et al., 2019). The restrictions on these computations of R_e and R_v mean that the values should not be compared to those from other field campaigns – the values a representative of probe response only. Bulk LWC values for cloud particle spectrometers were computed using Eq. 7.

$$N(D) = N(i)/SV(i) \tag{3}$$

480
$$where\ SV(i) = SA(i) * TAS \tag{3.1}$$

$$N_{a,c} = \sum_{i=1}^{nbin} N(D) \tag{4}$$

$$R_e = \sum_{i=1}^{nbin} D^3 N(D) dD \Big/ 2 \sum_{i=1}^{nbin} D^2 N(D) dD \tag{5}$$

$$R_v = \sum_{i=1}^{nbin} D^4 N(D) dD \Big/ 2 \sum_{i=1}^{nbin} D^3 N(D) dD \tag{6}$$

$$LWC = \frac{\pi}{6} \rho_w \sum_{i=1}^{nbin} D^3 N(D) dD \tag{8}$$

485 ### 2.6.2 Cloudy and clear-sky masks

Cloudy periods are readily identified from the airborne datasets by taking CDP observations of LWC and setting the lower threshold to 0.05 g m^{-3} at times when $N_c > 3$ cm^{-3}.

Cloud-free periods were identified more rigorously to avoid cloud contaminating the aerosol measurements. A clear-sky mask was generated for P3 data by taking LWC data from behind the CVI probe and cloud particle concentrations from CDP. A
490 threshold number concentration of 2 cm^{-3} from CDP and times when zero LWC was reported serve as the raw mask. To account

for sporadic sampling of low concentration events a 2-second safety margin (approximately 200 m) was applied around any positively identified cloudy points to generate the final clear-sky mask. The FAAM clear-sky mask employed bulk water content data from the three Nevzorov probe elements and the particle number concentrations from CDP as detailed in Barrett et al. (2020). To summarise here – the high resolution 32 Hz raw power data from the three Nevzorov sensing elements show

495 a bimodal distribution during cloudy- and clear-skies sampling with the lower power mode arising from clear-skies. The threshold between the cloud and clear-skies modes depends on a number of environmental factors and must be chosen empirically on a case by case basis. Here an upper limit of ~3.1 mW was chosen, below which the Nevzorov was deemed to be in clear-skies. A second constraint of particle number concentration from CDP below 1 cm^{-3} was specified, being less strict than the limit on P3 by virtue of the higher sensitivity of the Nevzorov flag catching more of the cloudy data points. The same

500 2-second safety window was applied.

The ARM site did not suffer from cloud occurrence in situ since it is located within the surface mixed layer.

2.7 Atmospheric radiation

The radiation measurements equipment on the FAAM BAe-146 during CLARIFY that will be compared to the measurements from the NASA P3 include:

505 a) Two upward and two downward facing Eppley broadband radiometers (BBRs) were fitted with clear and red domes covering the 0.3–3.0 μm and 0.7–3.0 μm spectral regions (e.g., Haywood et al., 2003). Degradation of the upper red domes owing to scouring of the leading face of the domes when flying in mineral dust during previous campaigns based close to the Sahara Desert (e.g., DABEX, GERBILS and FENNEC campaigns, Haywood et al., 2008; 2011; Ryder et al., 2013) was evident and thus data from the upper red domes were considered unsatisfactory and are not presented in the following analysis. Data from

510 red-domed Eppley lower radiometers was satisfactory. The BBRs are installed 3° pitched forward angle to the airframe which partially accounts for the nominal pitch of the aircraft when under standard operating conditions of 6° nose-up. Owing to the non-perfect alignment of the radiometers with the horizontal plane when mounted on the aircraft, box-pattern and pirouette manoeuvres are performed to correct any alignment discrepancies in the upper BBRs as described in Supplement Sect. 1. The fluxes measured by the BBRs have an estimated error of ±5 Wm^{-2} for upward fluxes (Haywood et al., 2001), and 3–5% for

515 downward fluxes, the higher uncertainty in the downwelling fluxes being due to aircraft pitch and roll correction uncertainties which vary as a function of the diffuse fraction and hence the altitude of the aircraft (Foot et al., 1986).

b) The Shortwave Hemispheric Irradiance Measurement System (SHIMS) measures the upward and downward spectrally resolved solar irradiances. Each of the upper and lower SHIMS uses two temperature-controlled Carl Zeiss spectrometer modules operating across the visible (VIS) spectral range 0.30–1.15 μm and near infra-red (NIR) range 0.95–1.70 μm. Data

520 from the VIS module were truncated at 0.95 μm to match up with the IR module at the short wavelength end. The pixel separation is approximately 0.0033 μm in the VIS module and 0.006 μm in the NIR module, giving approximate spectral resolutions of 0.010 μm and 0.018 μm with an in-house designed integrating head. The SHIMS instrument provides counts per millisecond. During this measurement campaign laboratory and transfer calibrations were performed. The combination of lab-work and this knowledge of the uncertainties associated with the BBRs suggests a likely uncertainty for SHIMS of ±10 %

525 (Vance et al. 2017). However, when operated on the aircraft a bias of up to 30 % between the SHIMS and BBR observations is apparent. An additional spectrally-invariant adjustment based on idealised model radiative transfer data was used to adjust the SHIMS observations to account for this as described in Supplement Sect. 1.

Comparable shortwave spectrally resolved irradiances were provided on the NASA P3 by the Solar Spectral Flux Radiometer (SSFR) in zenith and nadir directions (Pilewskie et al., 2003). A mechanical levelling platform ensured correct orientation of

530 the sensors and data were corrected for aircraft altitude and the angular response of light collectors. (Cochrane et al., 2019, 2021). The nominally visible wavelength range 0.35 μm – 1.0 μm is monitored with a Zeiss grating spectrometer with silicon linear diode array and the near infra-red range 0.95 μm – 2.10 μm with Zeiss grating spectrometer with InGaAs linear diode array. The devices have moderate spectral resolution of 0.008 to 0.012 μm with radiometric uncertainty of 3 to 5 % for both zenith and nadir with precision of 0.5 % (Cochrane et al., 2019, 2021). A National Institute of Standards and Technology

535 (NIST) traceable lamp was used to calibrate the instrument before and after the campaign and portable field calibrators monitored the performance of the instrument during the campaign.

One semi-permanent cloud feature that occurs in Ascension Island, is the generation of orographically forced cloud over Green Mountain whose altitude reaches 859 m. This cloud frequently impacted LASIC radiation measurements. As FAAM measurements were limited to a minimum distance of 2-4 km offshore of Ascension Island, the local impact of the orographically generated cloud hampered direct comparisons of down-welling solar irradiances and these are not therefore pursued further in this study.

3 Case studies

3.1 Airborne and side-by-side intercomparison

Both aircraft departed from Wideawake Airfield on Ascension Island on 18th August 2017 within a few minutes of one another, climbed out of the boundary layer and transited approximately 400 km ESE to a rendezvous point located close to 9° S, 11° W. The location for the flight intercomparison segments was chosen based on numerical weather prediction and aerosol forecasts to give the best possibility of encountering good conditions for sampling aerosol and cloud (Fig. 3). Overall, the two aircraft collected co-located data for a period of 75 minutes between 1250 and 1405 UTC, over a horizontal distance in excess of 450 km. Aerosol optical depth measured over Ascension Island using a handheld sun-photometer indicated a column aerosol optical depth at 500 nm of 0.16, suggesting the conditions on the day were relatively lightly polluted (Haywood et al., 2021). Satellite imagery on the day identified a region of broken cumulus clouds to the south of the Island that were a suitable target. The flight inter-comparison segments were located along the 9° S latitude line, offset ~100 km south of the island and the ground-based ARM site to maximise the chances of sampling adequate clouds.

Following rendezvous in the free-troposphere (FT) at ~5.8 km (Fig. 3), the two aircraft performed a wingtip-to-wingtip flight-leg (hereafter: runFT) for 10 minutes, from 125119 UTC along the 9° S latitude line (Table 2) with the BAe-146 formatting on the P3 to the starboard side. The flight leg, runFT, was conducted in clean FT conditions characterised by low aerosol number concentrations and clean conditions, ($N_a < 30$ cm^{-3} and CO < 90 ppb Fig. 4). While remaining in formation, the two aircraft made a profile descent from 5.8 km (runPRO), through an elevated pollution layer (runELEV) where lidar depolarisation observations indicated a small amount of dust particles, and into the boundary layer to finish at 1000 ft pressure altitude, which is nominally the same altitude as the ARM site. The elevated pollution layer was located between ~2.7 km and 4 km. Neither aircraft passed through cloud during the descent. Upon reaching the lower altitude both aircraft commenced a wing-tip to wing-tip straight-and-level run (SLR), hereafter runBL, flown at the same constant altitude, sampling cloud-free boundary layer air for 19 minutes. During SLRs, the FAAM BAe-146 sat between 7 and 13 m lower than the NASA P3. For runBL many instruments operated independently or had bespoke averaging times as documented in Table 2. Following runBL both aircraft climbed to 1.7 km and implemented a 14-minute cloud sampling leg at this altitude – hereafter runCLD. For safety reasons when performing this cloud sampling flight leg, the BAe-146 trailed behind the P3 by 5 minutes in time but followed the same track. Flying across wind meant that any turbulence or exhaust from the lead aircraft will have advected away from the region before the arrival of the second aircraft. Afterwards, the FAAM BAe-146 returned to Ascension Island to perform an intercomparison with the ARM site while the NASA P3 continued to make measurements remote from the island. Only the most relevant and appropriate measurement sections of the inter-comparison flight as indicated in Fig. 3 (b) are analysed here.

3.1.1 Meteorological parameters

The meteorological conditions encountered during the airborne intercomparison between FAAM BAe-146 and NASA P3 are summarised in the vertical profiles from runPRO, shown in Fig. 4. The temperature profiles show the decoupled stability profile expected for this location with a surface mixed layer in the lowest 600 m of the atmosphere, characterised by high RH > 70 % and a well-mixed temperature profile. Above the surface mixed layer and beneath the trade-wind inversion located close to 1.7 km sat a cloud-containing layer characterised by increasing RH with altitude. Broken cumulus clouds were present at this altitude throughout the period of the intercomparison.

Moderate levels of pollution due to BBA mixing into the boundary layer were found through the depth of the decoupled
boundary layer system CO > 100 ppb and N_a > 600 cm^{-3} close to the surface and 400 cm^{-3} just beneath the inversion. A
timeseries of CO data measured by LASIC at the ARM site is presented in Zhang et al. (2019) for both August periods, 2016
and 2017, showing that concentrations ranged between 50 and 150 ppb during 2017, and reaching somewhat higher to > 200
ppb in 2016. Ultraclean conditions in the Ascension Island region during the biomass burning season are defined by
accumulation mode aerosol particle number concentrations below 50 cm^{-3} and typically have median concentrations of CO =
69 ppb and an inter-quartile range (IQR) of 62 to 74 ppb (Pennypacker et al., 2020), with almost all cases having CO
concentrations levels < 80 ppb.

For the first 800 m above the trade-inversion, the free troposphere was pristine and dry, with N_a < 30 cm^{-3}, CO < 60 ppb (using
FAAM measurements), and low humidity values (Fig. 4). During the runELEV segment of the profile descent, the aircraft
passed through a thermodynamically-stable slightly-polluted layer between 2.7 and 4.0 km, with N_a > 50 cm^{-3}, and CO > 85
ppb. Water vapour concentrations were also higher than the layers immediately above and below, leading to slightly increased
RH locally, as is typical of the continental pollution plume (Pistone et al. 2021).

At 5.8 km conditions were relatively pristine and dry with N_a < 30 cm^{-3} and CO < 85 ppb and a water vapour water vapour
mixing ratio (vmr) of 168 ppb reported by FAAM.

Back trajectory calculations using the Met Office Unified Model were used to estimate source regions for airmasses arriving
at 9° S 12° W at 1200 UTC on 18th August 2017, chosen to be representative of the time and location of the airborne
intercomparison. Boundary layer trajectories, ending at 500 m and 1500 m showed airmass histories predominantly over the
ocean to the southeast for the previous 10 days, with the 1500 m trajectory over land for 10th to 12th August. A trajectory ending
at 3.5 km was located over Africa at altitudes between 6 and 8 km, from 10th to 13th August where it may have encountered
BBA in plumes or else lofted to that altitude through convection. Other trajectories ending in the free troposphere were
exclusively over ocean for at least the previous 7 days. The large-scale synoptic conditions of the day were typical of the region
with broken cumulus clouds.

3.2 FAAM – LASIC ARM site fly-pasts

FAAM flew sections upwind of the ARM site on 6 occasions (Table 2) between 17th August and 5th September, providing a
wide dynamic range of pollution parameters. One such flight leg took place following the FAAM—NASA intercomparison
on 18th August as the BAe-146 returned to base. The aircraft flew at a nominal altitude of ~330 m, a similar altitude to the
ARM site (340 m) and was displaced from the coast by between 2 and 4 km at the pilot's discretion depending on local flying
conditions. Flight segments took place across the mean wind direction and were between 7 and 15 minutes duration (40 to 90
km long). The mean wind speed at the ARM site was of the order 7 m s^{-1} meaning that sampling took place over a distance
equivalent to between 4 km (10 minute samples) and 12 km (30 minute samples). This approach assumes that local variability
is negligible across the aircraft track.

4 Results

4.1 Airmass characteristics

Vertical profiles of the thermodynamic state of the atmosphere during the airborne intercomparison for are presented for
temperature, vmr and RH (Fig. 4 (a), (b) and (c) respectively). Table 3 presents summary values for each of the parameters
and run segments. The temperature observations from NASA and FAAM are essentially unbiased, with a mean difference of
0.05 K between the aircraft across all segments - much smaller than the computed uncertainty of ±0.4 K for the FAAM sensor
for example. LASIC data at the ARM site tend to report warmer temperatures with a mean difference of 0.7 K which could be
related to the island heat effect or a genuine bias.

During the aircraft descent in Fig. 4 (b) the water vapour variations are tracked in a similar manner by FAAM WVSS-II and
the NASA WISPER instrument until passing through 800 m altitude where WISPER (both Tot1 and Tot2) reported drier

conditions than both FAAM and the NASA COMA instrument. For runBL the agreement between COMA and WVSS-II is better than the 5 % uncertainty of the WVSS-II. Differences between the WISPER instruments and WVSS-II tend to be up to 6.5 %, other than at the driest region of runFT where differences of 20 % occur, with up to 10 % between WISPER and the raw Buck CR2 measurement. Combining the WVSS-II and WISPER instrumental uncertainties in quadrature gives a combined
625   uncertainty of 5.4 % which does not explain all of the differences. Derived parameters of dew point temperature and relative humidity are shown in the table for convenience with NASA tending to report drier conditions by 0.6 K and 1 % RH in the mean across the dataset. LASIC also reports drier conditions than those onboard FAAM by a similar magnitude, at just over 3 % RH (Buck) or 1 % RH (WVSS-II) although this is over a much narrower dynamic range of humidity.

4.2 Gaseous and particulate pollution tracers

630   Carbon monoxide (CO) has a lifetime of over one month in the troposphere and is not susceptible to removal through precipitation processes. As such it is a suitable tracer for pollution from combustion and as such an important parameter for marking out airmasses. Fig. 4 (d) shows CO concentration data for the airborne profile descent while the flight level summary statistics summarised in Table 3 confirm that higher concentrations were reported by the NASA aircraft with a mean bias of +7 ppb (Table 3). Figure 5 (a) shows the correlations between CO from the FAAM aircraft with various flight level data from
635   NASA and during the 6 fly-pasts of the ARM site. LASIC data reported lower concentrations of CO with a mean bias of -4.8 ppb. Linear regressions performed between the FAAM data and the other two platforms show that the differences are consistent across the range of concentrations encountered (see Fig. 5 (a)). Ozone concentrations for each platform relative to the measurements made onboard FAAM are shown in Fig. 5 (b). The three instruments behaved comparably as demonstrated by the mean biases in Table 4.

640   SP2 probes systematically reported lower rBC_n and rBC_m concentrations at the LASIC ARM site than onboard the FAAM BAe-146 (Fig. 5 (d), (e), Table 3) with linear regression sensitivities of 0.79 and 0.88 respectively. NASA P3 SP2 comparisons against FAAM BAe146 are presented in the supplement (Sect. 4) for completeness, although it is expected that the temporary leak makes them unusable.

   Accumulation mode N_A concentrations from NASA and FAAM PCASPs during the profile descent are shown in Fig. 4 (e).
645   Mean and standard deviations of observations from each probe were computed over the full length of the individual runs (Table 3). Qualitative correlations with pollution tracer CO and thermodynamic properties of temperature and humidity are apparent along with being closely related to the optical extinction coefficients shown in Fig. 4 (f). The greatest concentrations N_a were observed during runBL, with NASA P3 reporting 550±61 cm^{-3}, as compared with 516±63 and 484±63 cm^{-3} from the two FAAM PCASPs. UHSAS data are available for this flight leg and show particle number concentrations for diameters greater
650   than 0.1 μm of 570±54 cm^{-3}. At these concentrations the flow rate errors dominate (assumed to be 10 % for the PCASP), which means that the number concentrations are comparable, although it is noted that the two NASA measurements are closer to one another than the FAAM measurements. At the cloud level (although when out of cloud) the number concentrations were slightly lower, of the order 400 cm^{-3}. Further observations were made during runFT and during descent through the elevated pollution layer and in the clear-skies portions of the cloud sampling leg as summarised in Table 3. Number concentrations as
655   low as 16±5 cm^{-3} (FAAM PCASP1) were recorded on the runFT leg and were of the order 74±23 cm^{-3} (FAAM PCASP1) in the elevated pollution layer. In general NASA and FAAM PCASP1 are within 10 % of one another, while NASA and FAAM PCASP2 are separated by slightly larger amounts. Linear regressions comparing NASA PCASP concentrations to FAAM PCASP1 and FAAM PCASP2 had slopes of 1.07 and 1.13, respectively.

   Number concentrations of CN are shown in Fig. 5 (c) and summarised in Table 3. A linear regression of CN concentrations
660   showed that NASA P3 data had a slope of 0.9 relative to the BAe-146 concentrations. This trend is the opposite of that shown by the PCASP observations. CN concentration data from the ARM site showed a slope of 0.8 relative to the BAe-146 data.

4.3 Aerosols

4.3.1 Aerosol composition

665 Comparisons between the airborne AMS's were possible for runBL where concentrations were larger than limits of detection. Concentrations were too low during runELEV to be considered for this. Likewise, data from elsewhere in the FT were also below limits of detection for some parameters. Table 3 shows that organic aerosol (OA) concentrations from NASA were 80 % of those reported by FAAM. Similarly, ammonium concentrations were lower, by 90 %, from NASA measurements compared to those sampled from FAAM. Concentrations of nitrate throughout the profile were low and close to the FAAM limit of detection, with NASA reporting 80 % of FAAM concentrations. Conversely, the NASA-reported sulphate 670 concentrations were 40 % higher than those reported by FAAM. Some fragment markers from the AMS measurements can provide information on the OA composition and oxidation states, e.g. m/z 43 and m/z 44. The m/z 43 is mainly from the fragments of saturated hydrocarbon compounds and long alkyl chains and are good indicators of fresh aerosols (Alfarra et al., 2007). The m/z 44 is the signal of the CO_2^+ ion from carboxylic acids and organo-peroxides and suggests the presence of oxygenated organic compounds (Aiken et al., 2008). Proportional contributions were calculated as the ratios of these OA 675 fragment markers to the total OA mass concentration respectively (f43 and f44). The f44 values were relatively consistent between two aircraft measurements for runBL, and the f43 also compares well (Table 3).

Data from LASIC ACMS (using the c2 dataset) do not compare well with those from FAAM, with LASIC–FAAM mass ratios of 4.0, 4.5, 3.9, and 3.1 for OA, SO_4, NO_3, and NH_4 respectively. These differences remain unexplained.

4.3.2 Aerosol physical properties

680 Aerosol PSDs are presented as number distributions (dN/dlogD) for runBL in Fig. 6 (a), and for the runELEV and runFT leg in Fig. 6 (b). The accumulation mode in the boundary layer looks to be captured in a similar manner by the NASA PCASP and FAAM outboard PCASP1 and PCASP2 (Fig. 6 (a)). Data from PCASP probes here are not adjusted to an alternative RI. Poisson counting uncertainties (e.g., Lance et al., 2010) for individual channels (available here for FAAM probes and expected to be of similar magnitude for the NASA probe) are below 1 % for sub 0.5 μm diameter aerosol particles. Data for runBL were 685 also available from the NASA UHSAS, first corrected for the characteristics of BBA as described in Howell et al., (2020), and compare well with the PCASPs under test for diameters up to 0.5 μm which corresponds to the stated upper size limit for the correction algorithm.

Accumulation mode aerosol R_e values as reported by the individual instruments within the boundary layer agree well for the outboard PCASPs (Table 3) for runBL. The NASA PCASP reported $R_e = 0.139\pm0.004$ μm, and FAAM PCASP1 and 2 reported 690 0.140 ± 0.004 μm and 0.133 ± 0.003 μm respectively. The NASA UHSAS reported smaller mean values of 0.123 ± 0.014 μm with larger variability (note that the UHSAS is reporting geometric mobility diameter). In the free-troposphere only PCASPs reported data, with good correspondence observed between the two aircraft. Linear regression shows that R_e estimates were in good agreement at all altitudes with a slope of 0.97 found when comparing NASA PCASP to FAAM PCASP1 data. Following the performance in the boundary layer the FAAM PCASP2 reported smaller values of R_e, with a slope of 1.27 between the 695 FAAM PCASP2 and the NASA PCASP values. These numbers do not reflect ambient conditions as this would require adjustment to the RI of the material under test.

A coarse aerosol mode was also present during runBL. At diameters larger than 0.5 μm, where particle counts are much lower, Poisson counting uncertainties become significant: 40 % at 1.5 μm and more than 200 % at 3.0 μm. The magnitude of the differences between PCASPs is much larger than the combined uncertainties at supermicron diameters. The largest differences 700 are apparent between the two probes on the FAAM BAe146 platform while FAAM PCASP2 and the NASA PCASP are in good agreement. Only the FAAM CDP reported aerosol data in the particle diameter range 1-5 μm, but, at larger diameters, data from 2DS probes on both aircraft cross over with CDP observations and show distributions with similar shapes. This

coarse mode will contribute to the total optical scattering from aerosol particles, as evidenced by the NASA runBL nephelometer data (Sect. 4.3.3) when switching between PM1 and PM10.

705 Comparison of PSDs from the elevated pollution layer and the runFT leg are shown in Fig. 6 (b). The PCASP probes detected much greater concentrations of accumulation mode aerosol particles in the elevated pollution layer than the clean free-troposphere during runFT. A coarse mode was present in the elevated pollution layer that was not present in the clean free-troposphere, possibly composed of dust particles. The PCASP probes have the ability to distinguish the elevated pollution layer from the cleaner surrounding free troposphere, when taking instrumental uncertainties into account.

710 Comparisons between LASIC and FAAM of aerosol PSD took place on 6 occasions (Table 4) shown in Fig. 7, utilising the ARM site SMPS and the BAe-146 PCASP2 (outboard), PCASP3 (inboard) and SMPS (inboard). A dominant accumulation mode was observed on August 17th, August 18th and September 5th with good overlap observed between all PCASP and SMPS instruments. Only the SMPSs can detect the Aitken mode which was most evident on August 18th, August 22nd, August 24th and August 25th. The Aitken mode was dominant or comparable to the accumulation mode in magnitude on August 22nd and
715 August 25th, both notable for accumulation mode max particle number concentrations (in terms of dN/dlogD) below 100 cm^{-3}. When the Aitken mode max concentration was low (dN/dlogD < 200 cm^{-3}), the ARM SMPS reported higher concentrations than the aircraft SMPS. Otherwise, the FAAM aircraft SMPS reported concentrations significantly higher than the ARM SMPS, as was found for the accumulation mode. Generally, all instruments reported similar width and mean for both modes. The application of the empirical scaling factor (Wu et al. 2020) to FAAM SMPS data is supported by this comparison.

720 **4.3.3 Aerosol optical properties**

The vertical profiles of extinction coefficient (Fig. 4 (f)) show that data from the NASA and FAAM aircraft both identify the large scale features of the elevated pollution layer and the aerosol-laden boundary layer. The instruments aboard the NASA P3 reported larger extinction magnitudes in the boundary layer below 1.7 km at the 660 nm wavelength compared to measurements made from FAAM, but measurements from aboard the FAAM and the NASA P3 aircraft were similar
725 throughout the vertical profile at the 470 nm wavelength. During the descent, the NASA P3 instruments sampled the full particle size range (PM10) whereas the FAAM CRDS instruments sampled behind an impactor with an aerodynamic D50 cut-off at 1.3 μm. During runBL, the NASA P3 alternately sampled downstream of either a PM10 or PM1 inlet as detailed in Table 2.

Observations of σ_{SP} (470 nm) made onboard NASA from the three PM10 periods (runBL_A, _B, _C (Table 2)) showed a
730 decreasing trend along the run from values at the start of 67 ± 2 Mm^{-1} to 44 ± 3 Mm^{-1} at the end of the run with corresponding data from behind the PM1 impactor for periods runBL_1 and runBL_2 (Table 2) of 48 ± 4 Mm^{-1} and 43 ± 3 Mm^{-1} (not shown). Comparison of measured PM1 and PM10 σ_{SP} along runBL shows that the recorded σ_{SP} after the PM10 impactor were on average higher by ~14 Mm^{-1}, indicative of the contribution to scattering from supermicron particles, most likely of marine origin (Wu et al., 2020). Comparisons of σ_{SP} for red and blue channels for runBL are shown in Fig. 5 (f), (g) as a function of
735 data from FAAM BAe-146 for the NASA P3 and LASIC ARM site. Table 3 summarises these observations. The intercomparison of σ_{SP} observations from the two aircraft shows that NASA P3 observes between 50 and 60 % more scattering than the FAAM BAe-146 for non-size-selected observations (runBL_A, _B, _C), as given by the sensitivity of a linear regression. The two were closer, within 20 %, when the NASA P3 sampled only submicron aerosols (Fig. 5 (f), (g)). Blue channel σ_{SP} data from the ARM site has a linear regression sensitivity of 0.74 compared with the BAe-146 data and 0.39 for
740 the red channel during the 6 intercomparison flight-legs.

The comparison of σ_{AP} at the LASIC ARM site with FAAM measurements show that the 470 nm data had a linear regression slope of 0.99 during the 6 intercomparison flight legs (Table 2) with an offset of -0.39 Mm^{-1}. Similar performance was found at 660 nm, with a slope of 1.07 and offset of -0.33 Mm^{-1} - note that FAAM reported σ_{AP} greater than 1.0 Mm^{-1} on only two of the segments. For the 530 nm data (not available for σ_{SP}) the linear regression between the FAAM PAS and LASIC PSAP data
745 had a slope of 1.17, with comparisons available for 4 flight segments. This compares with a linear regression slope of 1.23 between the FAAM PAS and LASIC CAPS PM$_{SSA}$ data over the same flight segments. LASIC ARM site from the CAPS PM$_{SSA}$ probe (530 nm wavelength only) show good agreement on 18th August 2017, with LASIC reporting some 25 % greater

values of σ_{AP} on 17th August and 5th September, when ARM site data were *not* behind the PM1 impactor. The low magnitude concentrations on 24th August showed LASIC reporting 50 % of the concentrations on the aircraft with large variability.

750 σ_{AP} compares well between NASA and FAAM when NASA sampled behind the 1 µm impactor (Table 3, runBL_1, _2) for nominal blue and green wavelengths, following interpolation from native wavelengths. Figure 8 (a) shows submicron σ_{AP} as a function of wavelength for runBL_2. Data at 660 nm were not available from EXSCALABAR for this run due to low concentrations of absorbing particles and uncertainties arising from the determination of the sample cell background value from available background measurements. Upon arrival at low level for runBL, the background signal was large due to the
755 change in pressure following the profile descent and the changing aerosol conditions. NASA σ_{AP} data were derived as a function of wavelength between 405 and 660 nm by computing Å_{AP} between adjacent wavelengths and either interpolating or extrapolating from the nearest observation in wavelength space. The same is done for FAAM data between 405 and 515 nm, but between 515 and 660 nm the Å_{AP} was set to the CLARIFY campaign mean value of 0.88 as determined by Taylor et al. (2020).

760 The FAAM PAS and NASA PSAP data points at native wavelengths are within 1 Mm[-1] of one-another across the wavelength range with NASA reporting the lower magnitudes σ_{AP}. The extrapolated values of σ_{AP} from the NASA PSAP at wavelengths shorter than 470 nm fall outside the 1 Mm[-1] maximum expected error range from the FAAM EXSCALABAR data. Filter-based absorption measurements such as from the NASA aircraft PSAP are subject to larger biases and uncertainties than spectroscopic techniques such as those used in EXSCALABAR (e.g. Davies et al., 2019). Data for σ_{AP} from the FAAM TAP
765 instrument for three native TAP wavelengths fall within 10 % of the interpolated values for the EXSCALABAR PAS data that it shares an inlet with.

Absorption Ångström exponents, Å_{AP}, computed from pairs of wavelengths as a function of mean wavelength are shown in Fig. 8 (b) for both runBL_1 and runBL_2 for NASA PSAP, FAAM EXSCALABAR PAS and the FAAM TAP. Campaign mean data from CLARIFY are also shown for comparison, reproduced from Taylor et al. (2020). For this particular flight
770 segment only the 405—514 nm wavelength pair are available for FAAM EXSCALABAR. A general trend of increasing Å_{AP} at shorter wavelengths is apparent in these measurements from the intercomparison data, as would be expected considering the CLARIFY campaign mean data from Taylor et al. (2020). Data from NASA PSAP are in better agreement with the CLARIFY EXSCALBAR PAS campaign mean values than the FAAM TAP data (which is also filter-based).

Similar comparisons of Å_{AP} for the FAAM EXSCALABR and LASIC PSAP observations are also shown in Fig. 8 (b) for
775 three segments with $\sigma_{AP} > 1.0$ Mm[-1]. FAAM Å_{AP} data over these segments are shown as mean and the range and are largest at shortest mean wavelength, following the trend of the aircraft intercomparison other observations. Contrary to this, the LASIC data show a flat, or slightly decreasing trend towards shorter mean wavelength.

Determination of ω_0 from observations of optical properties is hampered by the low magnitude of σ_{AP} and the short averaging times available for this study. There is additional discussion of this in Sect. 5.4.

780 **4.4 Atmospheric radiation**

4.4.1 Comparisons of downwelling spectral irradiances from FAAM SHIMS against those from the NASA SSFR

Three opportunities to compare the spectral irradiance from the SHIMS and SSFR radiometers are available for runs with the FAAM BAe-146 and NASA P3 aircraft: i) runFT which is the SLR at 5.8 km, ii) runPRO, which consisted of the profile descent from 5.8 km to 330 m, iii) runBL which is the SLR at 330 m. These manoeuvres were performed wing-tip to wing-tip.

785 Figure 9 (a)–(i) shows the downwelling spectral irradiance from SSFR (NASA) (first column) and SHIMS (FAAM) (second column). The third column shows the fractional difference between the measured spectral irradiances. Similarity between the measurements is apparent. For runBL, the spectral irradiances are variable at around peak values of 400-2500 Wm[-2] µm^{-1}. This is likely be a consequence of the two aircraft operating below patchy cloud where solar radiation is generally diminished but, on occasion, 3-dimensional reflectance effects from the edge of clouds can lead to a local enhancement of radiation (Marshak
790 and Davies, 2005). The agreement in the spectral irradiances during runBL when integrated over wavelength is on average within 0.04 % for the VIS SHIMS module (0.30 – 1.15 µm) and within 0.57 % for the NIR SHIMS module (0.95 – 1.70 µm)

(Table 4). The agreement between the irradiances when integrated over wavelength during runFT and runPRO are in somewhat poorer agreement and are on average some 1.5 – 2 % higher in the VIS SHIMS module, but 0.5 – 1.7 % lower in the NIR SHIMS module.

4.4.2 Comparisons of upwelling spectral irradiances from FAAM SHIMS against those from the NASA SSFR

The upwelling spectral irradiances from the FAAM and NASA aircraft are shown in Fig. 9 (j)–(k) for runFT along with instantaneous differences between then (Fig. 9 (l)). Considerable variability owing to the aircraft passing over variable amounts of cloud and, to a lesser extent, aerosol is apparent. Once again the measurements from the BAe-146 and the P3 aircraft are in reasonable agreement, with differences in the integrated irradiances of just 1 Wm^{-2} (max 5 %) and similar measures of variability (see also Table 4).

4.5 Cloud microphysical and bulk properties

The longitudinal cross section of N_c (Fig. 10 (c)) shows that broken cumulus clouds were sampled in situ by both aircraft with concentrations varying across the run. It is worth recalling that due to safety considerations the sampling by the two aircraft was separated by a distance equivalent to 5 minutes travel time. The composite cloud PSD from all cloud passes along the runs are shown in Fig. 10 (a) for data from the CDP and 2DS probes. The errors are presented for the FAAM instrument only for clarity since the magnitude of errors will be similar between similar instruments.

The probability distributions functions (PDF) of cloud drop effective radius, R_e, shown in Fig. 10 (b), have a bimodal nature from both FAAM and NASA observations, with modes overlapping well.

Mean N_c values were slightly greater and with a larger standard deviation on the NASA platform: 274 ± 153 cm^{-3}, than from FAAM: 226 ± 69 cm^{-3} (Table 3). The 90th percentiles of the distributions were 528 cm^{-3} (NASA) and 308 cm^{-3} (FAAM), and 99th percentiles 595 cm^{-3} (NASA) and 335 cm^{-3} (FAAM). Errors due to particle coincidence in the sample volume are expected to be minimal at these concentrations (< 1 % at 800 cm^{-3} according to Lance et al., 2012). Number concentrations of N_a were lower at this cloud level than encountered along runBL at 402 ± 28 cm^{-3} (NASA) and 374 ± 33 cm^{-3} (FAAM PCASP1) (Table 3). These N_a values were below the peak cloud drop number concentrations, implying that the clouds were nucleated some way below the flight level – something which was observed visually from the flight deck.

Occasionally the NASA P3 encountered much greater cloud drop number concentrations, $N_c > 500$ cm^{-3}, with the 90th and 99th percentiles some 30 % greater than for FAAM. Inspection of the time series of in situ vertical wind velocities (not shown) indicated that the P3 flew through a strong updraught in excess of 6 m s^{-1}, a feature not encountered by FAAM. Such an updraught would be expected to increase the supersaturation, nucleate a greater number of cloud particles from the aerosol population and condense more water. The particle size distributions (Fig. 10) for cloud (CDP) and small drizzle (2DS) from both platforms are exhibit similar shapes at all sizes given the demonstrated magnitudes of the uncertainties. The NASA 2DS reports slightly larger concentrations of particles larger than 40 μm, possibly due to the enhanced updraughts encountered. To investigate the impact of this the derived metrics of the PSD are computed with the data from the strongest updraughts removed – chosen to be above a threshold of 2 ms^{-1}, as this was seldom encountered by FAAM. Away from strong updraughts the NASA mean N_c is 253 ± 137 cm^{-3}, which is closer to the values reported by FAAM.

Derived size metrics count median diameter, R_e, and R_v were similar across the two platforms – again when the data from within the strong updraught are excluded the agreement is improved (Table 3). FAAM employed bulk-water corrected bin diameters, but the magnitude of differences between those and nominal bins is less than 5 % especially at diameters close to the mode of the PSD. R_e is identical away from strong updraughts as sampled by the CDPs, at 7.0 μm, with R_v also very similar: 7.7 μm (NASA) and 7.8 μm (FAAM).

LWCs are also very similar away from strong updraughts, at 0.24 ± 0.15 gm-3 (NASA) and 0.23 ± 0.15 gm-3 (FAAM). The 75th, 90th and 99th percentiles of the distribution are also broadly similar, whereas the LWC from locations including the updraught passage has a higher mean, and 99th percentile values over 2.0 gm^{-3}. Additional LWC data comes from the hot-wire probes. The FAAM Nevzorov reported 0.23 ± 0.16 gm^{-3} and while this is very similar to the FAAM CDP, recall that these data were used to effectively baseline the CDP calibration (Supplement Sect. 3). Excluding data during strong updraughts, data from the

NASA King probe are low in comparison at 0.12 ± 0.10 gm^{-3}. The expected uncertainty range for these evaporative probes according to Baumgardner et al. (2017) is between 10 and 30 %. The FAAM Nevzorov LWC compares well with LWC derived from the optical probes on the NASA aircraft but the NASA King probe exhibits a low bias. This may be due to a different size dependent collection efficiency or inadequate baseline removal (e.g., Abel et al., 2014).

5 Discussion

5.1 Thermodynamics and airmasses

Temperature measurements between the two aircraft were essentially unbiased, while the data at the LASIC ARM site were warm compared to the FAAM airborne data by slightly more than the instrumental uncertainty. The aircraft tended to fly between 15 m and 30 m lower than the ARM site which does not account for the differences. It is possible that surface heating on the island results in the slightly warmer temperatures observed at the ARM site.

Water vapour vmr sampled by the NASA WISPER Tot1 and FAAM WVSS-II were broadly similar although NASA reported drier conditions in the boundary layer and lower altitudes by an amount corresponding to a dewpoint of 0.6 K.

Conditions at the LASIC ARM site were reported to be up to 3.3 % RH drier than the FAAM aircraft, this difference being similar to the magnitude of the uncertainty of the ARM site Vaisala sensor itself. The sensor makes a direct measure of RH independent of temperature measurements. Conversion to vmr for comparison with the FAAM aircraft probe shows that the LASIC mean values of vmr are 1.9 % lower across the 6 fly-pasts (Table 3). Possible impacts of any discrepancies in RH reported by NASA, LASIC and FAAM would be encountered when using the distributions of boundary layer humidity to estimate CCN (Cloud condensation nuclei) concentrations, or when using aerosol growth models to predict optical scattering from aerosol as a function of RH.

Fluctuations of vertical winds during runBL from the BAe-146 show a larger standard deviation than data collected by the NASA P3 during this side-by-side sampling leg. The skewness, or the relative occurrence of outlier values was more positive on the NASA P3, indicating that it occasionally sampled stronger updraughts than the FAAM BAe-146 encountered. The two aircraft inevitably encountered different conditions when sampling at the cloud level – a consequence of the 5 minute separation in time. Air density and potential temperature were not strongly biased (not shown), meaning that thermodynamics and correction of concentrations to STP are not impacted by the thermodynamic measurements.

Pollution events at Ascension Island have been defined by Zhang et al. (2019) using thresholds of rBC$_m$. During August, 100 ng m^{-3} was set as the upper limit for clean conditions, and > 500 ng m^{-3} defined the most polluted tercile of conditions (Zhang and Zuidema 2019). Data from the intercomparisons presented are found in both the cleaner lower tercile and the moderately polluted middle tercile. The data from ARM and FAAM are shown to be in sufficient agreement to use these to determine the membership of clean and polluted conditions reliably. However, data from NASA is 50 % lower than that from FAAM. Specifically, during part of the flight on 18th August 2017, a leak was detected to one of the instrumentation racks. This limited the data that was recoverable from the flight, and it is therefore likely that the data from the intercomparison period were also affected.

The CO data presented here from the FAAM – LASIC comparisons span a range 60 to 110 ppb indicative of clean through to moderately polluted conditions. A similar range was encountered during the airborne intercomparison although the cleanest conditions below 80 ppb were only encountered as the two aircraft descended through the relatively pristine FT layers. The LASIC ARM site consistently reported CO concentrations up to 9 % lower than FAAM. FAAM and NASA CO data are close to being within the quoted NASA uncertainty of 6 % ±1 ppb. NASA consistently report the highest concentrations. It is noted that the FAAM instrument was regularly calibrated with reference gases during flights (Sect. 2.3) giving confidence in the instrument performance. The difference between the CO measurements from the NASA P3 and the LASIC ARM site is expected to be larger than between the aircraft platforms, something which remains an unresolved issue.

Importantly though, the magnitude of the differences in CO measurements between platforms does not preclude robust identification of pollution regimes within the south Atlantic region (Wu et al., 2020; Gupta et al., 2021a). Concentrations of

CO in the planetary boundary layer, close to the coast, during ORACLES-2016 rarely exceeded 120 ppb (Diamond et al.,
880   2018). During ORACLES 2016 in Namibia, CO concentrations in stratocumulus topped boundary layers were up to 30 ppb
higher during instances of contact between the biomass-burning aerosol layer and the cloud layer, relative to instances of
separation (Gupta et al., 2021a). Concentrations of CO in pristine oceanic conditions in the southern Hemisphere have
previously been observed to be between 50 and 60 ppb (Allen et al., 2008, 2011). Outside the BBA season, between December
2016 and April 2017 similar conditions were observed at the LASIC ARM site, with a median value of 59 ppb and an IQR of
885   55 to 65 ppb (Pennypacker et al., 2020). Ultraclean days were also observed during the BBA season (typified by $N_a <$ 50 cm⁻
³) which corresponded to median CO concentrations of 69 ppb and an IQR of 62 to 74 ppb (Pennypacker et al., 2020) with
Abel et al. (2020) observing 70 ppb in the vicinity of pockets-of-open-cells convection during BBA season. For August 2017
at Ascension Island the vast majority of CO concentrations were between 50 and 150 ppb, although during August 2016 there
were multiple days where CO concentrations above 150 ppb and as much as 200 ppb were observed at the ARM site (Zhang
890   et al., 2019). Working from Namibia, and generally sampling within 10 degrees of the coast between, 8 S and 24 S, ORACLES
2016 encountered CO concentrations between 60 and 500 ppb (Shinozuka et al., 2020) with the highest concentrations found
in the elevated smoke plume above the marine boundary layer. The most polluted conditions encountered during biomass
burning season were not sampled during the intercomparisons.

The ozone data from FAAM BAe-146 and NASA P3 fall within the measurement uncertainty of ±1 ppb (±6 % in the worst
895   case) and are essentially unbiased. There is a similar situation for the FAAM to LASIC comparisons with differences below
the measurement uncertainty. This suggests that there are no inherent biases in the gas phase sampling systems on either
aircraft. This leads to the conclusion that the bias in CO measurements must be related to the CO instruments themselves or
their sample supply lines. There is a suggestion from the data of a slightly non-linear behaviour to the comparisons between
the two airborne measurements, although within the expected range.

900   **5.2 Aerosol chemical composition**

Comparisons between the two airborne AMS instruments are generally within one standard deviation for ammonium and
nitrate, and within the 30 % to 37 % quoted uncertainty of the NASA P3 AMS. NASA P3 reported more sulphate and FAAM
BAe-146 reported a greater mass of organics. Differences may arise from low magnitudes of material, differences between
retrieval algorithms, collection efficiencies within the AMS instruments or relative ionisation efficiencies of the chemical
905   components. These differences, detailed further below, were not able to explain the differences in the sulphate masses,
ultimately leading to the conclusion that the two instruments can be meaningfully compared.

Limits of detection were found to be material specific using ORACLES 2016 flight data (Dobracki et al., 2021) . However,
during the intercomparison the mass concentrations were well above those limits, aside from some of the individual mass
fragments of organics, for which mass concentrations were close to their 0.15 µg m⁻³ limit of detection.

910   To explore any potential effect of using different post-analysis algorithms, data from the NASA P3 high resolution AMS was
also analysed using the SQUIRREL algorithm used by the FAAM Bae-146 AMS. This demonstrated that the different
algorithms can account for only 7 % of the difference (Dobracki et al. 2021). Relative ionisation efficiency (RIE)
characterisation could account for only minimal differences between instruments. Calibrations performed on the FAAM BAe-
146 instrument resulted in changes to the RIE coefficients for ammonium of less than 2 % and for sulphate of 10 %. Further
915   information is to be found in Supplement (Sect. 4).

Another possible source of the difference lies in the application of collection efficiencies. Liquid, primarily acidic, aerosols
are collected more efficiently than neutralised particles (Dobracki et al., 2021). Collection efficiency values were set at 0.5 for
each airborne AMS, since the aerosol was shown to be fully neutralised in the free troposphere for the ORACLES dataset
(Dobracki et al., 2021), and for both boundary layer and free troposphere for the CLARIFY dataset (Fig. S3).

920   The source of the nitrate in this region may be either ammonium nitrate or organic in nature (Dobracki et al. 2021). This can
be explored to some extent by considering the ratio of NO^+ (m/z 30) to NO_2^+ (m/z 46), given the observations of Farmer et al.
(2010). However, given the low concentrations of nitrate within the boundary layer, large uncertainties in the m/z 30 to m/z
46 ratio are expected. Considering the uncertainties can exceed 50 % for the m/z values and 75 % for the fractional values with
larger errors on NASA P3 data in this instance, the measurements show reasonable agreement (Table 3).

925   Uncertainty in OA mass concentrations stems from the determination of organic nitrates, with greater mass of OA reported BAE-146. By assessing the magnitude of the contributions of mass fragments 30 (NO^+) and 46 (NO_2^+) it is possible to assess the balance of organic to inorganic nitrates. During the airborne intercomparison nitrate concentrations were low and close to the FAAM limit of detection. While it is possible to compute and compare values for the ratio of f30 to f46 it is not clear that in these circumstances that would be particularly instructive given the low total nitrate mass.

930   Useful analysis of chemical composition takes place when derived quantities are computed, for example to give information of the age-state of a polluted air parcel. For example, in the Ascension Island region the BB OA is highly oxidised and of low volatility suggesting it is well-aged (Wu et al., 2020). Closer to the coast where ORACLES 2017 operated the aerosol might be expected to be younger. For OA fragment markers, the f44 compares well between two aircraft measurements, and the f43 is within one standard deviation. The difference of f43 may arise from the low magnitude as the BB OA is highly oxidised in
935   the Ascension Island region and the fraction of hydrocarbon-like OA is low. Good performance of the OA fragment markers (e.g. f44 and f43) between the two instruments and similarity between calibrated values suggest that the CLARIFY and ORACLES datasets should be useful in determination of the chemical age of biomass burning products.

Insight into the conditions at the time of combustion can be gleaned from ratios BC/ΔCO and OA/ΔCO where ΔCO is the difference from the background concentration in the boundary layer of (from CLARIFY data) CO_{back}= 66 ppb (Wu et al.,
940   2020). CLARIFY observations of BC/ΔCO were indicative of flaming combustion in both the free troposphere and similar in the boundary layer, with perhaps some inefficient cloud processing (Wu et al., 2020). The 50 % difference between FAAM and NASA BC mass concentrations drives discrepancies in BC/ΔCO, where FAAM = 14 ng μg^{-1} and NASA between 5 and 7 ng μg^{-1}. Accounting for the CO bias makes the comparison worse. Despite this, the width of the range representative of flaming combustion is such that conclusions on combustion type would be the same for each platform. For the 6 measurements
945   available from the FAAM–LASIC comparison, the results are more comparable with FAAM =10.6 ng μg^{-1} and LASIC = 10.3 ng μg^{-1}.

Comparisons of OA/ΔCO yield 0.96 μg μg^{-1} (FAAM) and 0.92 μg μg^{-1} (NASA). The positive biases in OA and CO measurements reported by NASA P3 compared to FAAM BAe-146 combine favourably, although note – this takes the background CO from the CLARIFY-only measurements that took place within the region.

950   The comparison between the FAAM BAe146 AMS and the LASIC ARM site ACMS is poor. There is factor between 3 and 4.5 difference between individual species mass concentrations with the larger magnitudes observed at the ARM site. The cause of this is unknown. To investigate LASIC ACMS data points from 30 minutes either side of the valid time were looked at and the resultant range compared to the FAAM AMS data. This did not result in better agreement. Unlike the airborne AMS collection efficiencies of 0.5, at the time of the comparison all LASIC data points had composition dependent collection
955   efficiencies of unity, although adjacent time sometimes had values below 1.0. The unexplained differences would benefit from further investigation.

5.3 Aerosol physical properties

During the airborne intercomparison PSDs in the accumulation mode compared well between airborne PCASPs and the UHSAS once the evaporation of absorbing particles due to the high laser power was accounted for (Howell et al. 2021
960   Individual studies will be required to assess the probe response, to the particular RI of aerosols encountered (e.g., Peers et al. 2019) and to conduct optical closure studies with radiometric measurements. It was shown by Peers et al. (2019) that aerosols were effectively sampled by FAAM in the optically active region of the accumulation mode which fell between 0.3 and 0.5 μm diameter (77 % of extinction).

The external PCASPs were able to distinguish between the elevated pollution plume and the cleaner surrounding free
965   troposphere. Here the performance of the NASA PCASP is more similar to the FAAM PCASP2. The accumulation mode at runFT is less well defined, and Poisson counting uncertainty is large at sizes greater than 0.5 μm. The presence of a coarse mode in the elevated pollution layer fits with back trajectory calculations which had the air parcel history over the African continent (not shown). This is consistent with similar conditions during ORACLES 2016 where back-trajectories showed polluted above-cloud air-masses (Gupta et al., 2021a).

970 A coarse-mode of marine aerosols was observed in the boundary layer and captured by PCASPs, the FAAM CDP and 2DS probes. The source of the discrepancy between the response of PCASP probes at larger diameters above 2 µm is unknown, but the inlet sampling efficiency of large particles, low concentrations, inlet jet alignment and possibly instrument RH differences may all contribute. The CDP cross-over with PCASPs is poor and large errors exist from low counting statistics at larger sizes and correspond to the region where 2DS sample volume uncertainties are largest, although the cross-over is good, as is

975 comparison between 2DS probes from NASA and FAAM. Sampling the coarse-mode and being able to account for its scattering is important for optical studies. At larger sizes > 600 nm the aerosol composition will not contain large amount of BBA (e.g., Wu et al., 2020) and likely consists of purely optically scattering hydrated salts, meaning comparison with probes such as CDP and OAPs are therefore likely to be more valid.

Observations of PSDs generally agreed well between LASIC and FAAM, when considering the scaled FAAM SMPS data and

980 either the external PCASP2 or internal PCASP3 with calibrated bin boundaries corrected to an appropriate RI for BBA. Condensation particle number concentrations were slightly lower for the LASIC dataset. The mean ratio of bin concentrations for sizes smaller than 600 nm (BBA RI corrected) between PCASP2 and PCASP3 was close to unity, although individual flights saw differences for the larger sies up to 30 % (average of 14 %).

5.4 Aerosol optical properties

985 LASIC measurements of σ_{SP} are ~74 % of those from FAAM at 470 nm and only ~40 % at 660 nm. While the EXSCALABAR optical properties are for dry aerosol, the LASIC nephelometer is reported to operate between 50-60%. However, if that were the only difference, the LASIC σSP would be larger than EXSCALABAR σSP, even for aerosol dominated by only weakly hygroscopic organics. Two further possible explanations for these discrepancies in σ_{SP} are 1) the aerosol population sampled at the ARM site is different to that encountered by FAAM, or 2) the aerosol sample is modified in some way during sampling.

990 The ARM site is located on land which presents an opportunity for introduction of aerosols not encountered during the airborne sampling over the ocean.

Relative humidity is not thought to be the cause of the discrepancy because the LASIC data are not actively dried unlike the EXSCALABAR data. Hence, the LASIC data might be expected to produce more scattering from a population of aerosols with larger sizes. There may be important size-dependent transmission efficiency artefacts. These would have to affect only

995 larger particles as there is good correspondence between σ_{AP} and rBC observations along with N_a, all of which are dominated by aerosol smaller than 600 nm diameter (e.g., Peers et al. 2019). Comparisons of scattering at the ARM site between the nephelometer and the CAPS PM$_{SSA}$ data (Sect. 11.5) show internal consistency, suggesting that the difference between the airborne and ground-based measurements is not related to a specific instrument but a systematic issue. Aerosol sampling – in particular inlets and particle transmission - is discussed further in Sect. 5.5.

1000 Observations of σ_{AP} from FAAM and NASA agree within instrumental uncertainties given low magnitude of signal and short averaging time. Likewise, there is good comparability between FAAM and LASIC for observations of σ_{AP}, to better than 20 % for the LASIC PSAP. Additional data from the CAPS PM$_{SSA}$ probe support the observations and suggest no inherent bias between the ground and airborne measurements, or from filter correction schemes. This study does not attempt to replicate previous work considering filter-based correction schemes such as Davies et al. (2019). Instead, it compares the data as

1005 published by each group. NASA data was based on the Virkkula (2010) wavelength-averaged scheme for comparability with other studies (e.g., Pistone et al., 2019), and the LASIC data using an average of the absorption calculated using the correction schemes from Virkkula (2010) (wavelength-averaged) and Ogren (2010).

Aerosol ω_0 and Å_{AP} are two important climate relevant parameters that are derived from observations of aerosol optical properties (e.g., Sherman and McComiskey, 2018). Å_{AP} was compared between the two aircraft and against the CLARIFY

1010 campaign mean (Taylor et al., 2020). The trend of larger Å_{AP} at shorter mean wavelength is apparent in all airborne datasets, including filter-based retrievals. The data from the LASIC ARM site show different behaviour for the three comparison segments under consideration, with smaller values of Å_{AP} for shorter mean wavelength. Zuidema (2018) noted spectrally flat behaviour for the 2016 BBA season based on LASIC ARM measurements. The range of values encountered for the blue-green pair during the season was large during the BBA season of 2016, with extreme values smaller than 0.8 and greater than 1.4

1015 (Zuidema 2018). The variability during that year is not expected to be unusual and so the range of values encountered during

these short intercomparison segments may just reflect this natural variability. The short sample time may not be sufficient to capture that variability.

Campaign mean ω_0 comparisons have been discussed elsewhere for the CLARIFY and LASIC campaigns with Wu et al. (2020) noting that the measurements collected at the ARM site were lower than the measurements made onboard the FAAM

1020 BAe-146 especially at longer wavelengths. Airborne ω_0 measurements made in the free troposphere during ORACLES 2016 (Pistone et al. 2019) were shown to be slightly larger than those made by CLARIFY (Wu et al. 2020). While both ORACLES and LASIC used filter-based absorption in the computation of ω_0, in this instance the filter correction schemes are not thought to be the dominant source of uncertainty (Haywood et al. 2021). Rather, the differences between measurements of scattering (or extinction) coefficients are the likely source of discrepancies in ω_0.

1025 **5.5 Inlets and particle transmission**

Here we consider the effects of inlet systems, internal pipework, and sampling system components such as impactors on the comparisons.

Transmission of a representative sample of aerosol particles into an aircraft while flying at high speed is challenging. The NASA P3 SDI has been well characterised and is expected to have a transmission function approaching unity for submicron

1030 aerosols: differences between this and other inlets was shown to be below 16 % (McNaughton et al., 2017). Likewise, the Rosemount inlets employed on FAAM have been shown to transmit with a function reasonably close to unity for submicron particles (Trembath et al., 2012), although these inlets are less well characterised than the SDI.

The starboard side of the BAe-146 within the vicinity of the Rosemount inlets for EXSCALABAR and SP2 is aerodynamically clean, with no barriers to the airflow. Good agreement was observed between FAAM BAe-146 and NASA P3 data for σ_{AP} and

1035 submicron σ_{SP}. There is support from LASIC σ_{AP} data which follow the FAAM measurements very closely, but not from LASIC σ_{SP} measurements which are much lower than those from FAAM. However, LASIC rBC_n are within 20 % of FAAM and rBC_m within 10% both lower. BC measurements were much lower from NASA than FAAM, although a leak was identified at other times, which possibly also affected the data collected during the intercomparison period. From observations presented here it seems reasonable to conclude that the starboard-mounted Rosemount inlets are adequately sampling submicron aerosols.

1040 The BAe-146 port-side Rosemount inlets are potentially compromised by the large-radiometer blister pod. CN number concentrations from FAAM and NASA are within 10 %. However, LASIC CN number concentrations are approximately 80 %, lower than FAAM. This ratio is similar to the ratios between BC measurements and suggestive of a small systematic effect. AMS data from the two aircraft showed good agreement and some differences were accounted for through CE and RIE. Organic aerosols have been shown to be contained in particles smaller than 0.4 µm (Wu et al., 2020) and it is here that the

1045 largest difference between FAAM and NASA data occur – with FAAM reporting 40 % greater mass concentrations. The AMS data (biased to larger particles with greater mass) and CN concentrations (biased to smaller particles with greater number) are not suggestive of particle shadowing by the BAe-146 blister-pod.

The FAAM SMPS measured aerosol PSDs behind a port side Rosemount inlet and data from the 6 LASIC fly-past segments mostly compare well with the LASIC SMPS and FAAM PCASP2 and PCASP3. There are differences although they do not

1050 appear to be systematic but vary day-to-day, with concentrations larger in either the accumulation or Aitkin modes from the FAAM SMPS compared the one at LASIC. It is noted that there is good agreement in the overlap region on all 6 days between the LASIC SMPS and the externally mounted FAAM PCASP2 and the internally mounted FAAM PCASP3. During CLARIFY as a whole, good agreement between the FAAM SMPS and the FAAM PCASPs was demonstrated in the cross-over region (Wu et al., 2020). Externally-mounted PCASPs on FAAM BAe-146 and NASA P3 also show good agreement, along with the

1055 internally mounted NASA UHSAS, once corrected for particle heating and evaporation.

Overall, there are no observable biases introduced into the datasets by sampling submicron aerosols through Rosemount inlets either on the aerodynamically clean starboard side of the FAAM BAe-146, or the port-side, which supports the blister-pod. This study does not have sufficient data to conclusively answer questions relating to the size dependent collection efficiencies of Rosemount in various location on the FAAM BAe-146 platform (a task begun by Trembath et al., 2012, Trembath, 2013).

1060 Should better precision be required than that shown here, then an additional study involving detailed flow modelling will likely be required.

Differences between the platforms may result from transmission losses within internal plumbing. Careful design of flow paths within pipework can mitigate against some of the potential losses of aerosol particles. Sample line losses can then be modelled, for example Baron (2001). Aerosol particle data from FAAM EXSCALABAR were corrected for measured sample line losses.
1065 Transmission loses of aerosols in the submicron range from the NASA P3 SDI to the AMS is demonstrated to be lower than 20 % as an average for the ORACLES campaign, although this is not explicitly accounted for when calculating concentrations (Dobracki et al. 2021). Similar losses are to be expected for other internal FAAM instruments, where concentrations were not corrected for line-losses.

Differences remain between LASIC ARM site and FAAM BAe-146 σ_{SP} observations. The BAe-146 EXSCLABAR sampled
1070 downstream of a 1.3 μm aerodynamic diameter impactor (Taylor et al. 2020) and the LASIC ARM site employed a 1.0 μm aerodynamic impactor upstream of instruments. Assuming the density of the sampled material to be 1.6 kg m^{-3} (appropriate for BBA) the FAAM impactor has a physical cut size diameter of approximately 1.0 μm, to within 3 % (computed using AEROCALC, Baron, 2001). Ammonium sulphate, having only a slightly higher density (1.77 kg m^{-3}), therefore has a similar cut size. For the LASIC ARM site impactor, the physical cut size diameter (assuming spherical particles) is 0.78 μm.

1075 Scattering by coarse mode particles was observed by the NASA nephelometer, when not sampling behind its impactor. Since the small end of the coarse mode very probably extends to diameters less than 1.0 μm, these sub-micron coarse mode particles are likely to contribute more to the extinction measured behind the EXSCALABAR impactor than the scattering measured behind the LASIC impactor. Thus, differences between σ_{SP} (and subsequently ω_0) from LASIC and FAAM may stem from this difference in the upper cut size of the impactors, especially where marine boundary layer aerosols are present.
1080 However – good agreement between NASA and FAAM was demonstrated for σ_{SP} when NASA also operated behind a nominal 1.0 μm aerodynamic diameter impactor. This may be a fortuitous results of the conditions encountered during the airborne intercomparison. It would have been beneficial to use the impactors with the same cut-size for the different campaigns being compared. Caution should be taken when comparing scattering measurements and derived parameters across these campaigns. This might take the form of detailed optical modelling and closure with radiation measurements.

1085 **5.6 Atmospheric radiation**

In cloud-free skies over ocean, where the surface reflectance is relatively well known, the direct radiative effect can be inferred simply from measurements of the upwelling integrated solar irradiance and the spectral solar irradiance (e.g., Haywood et al., 2003). However, this does not constitute radiative closure because the additional upwelling flux from the aerosol layer is a convolution of the aerosol optical depth, the backscattered fraction, and the degree of absorption of the aerosol, and the
1090 solutions are therefore non-unique. Among other studies, Haywood et al. (2011) and Cochrane et al. (2019) demonstrated that measurements of both the upwelling and down-welling integrated irradiances are needed if a unique solution relating the aerosol physical and optical properties unambiguously to the upwelling and downwelling solar irradiances is to be achieved. In cloudy skies, where the reflectance from clouds varies far more than the reflectance from the well-characterised sea-surface, it is even more important to understand the accuracy and variability of the upwelling spectral irradiances if radiative closure
1095 is to be achieved.

For down-welling irradiances, the agreement in the radiometric measurements appears to be better under diffuse sunlight conditions than during direct illumination conditions. This may be due to inaccuracies in the pitch and roll correction for the SHIMS instrument, which requires an accurate partitioning between the pitch-and-roll-corrected direct irradiance and the non-pitch-and-roll-corrected diffuse irradiance (see Jones et al., 2018). Other factors such as the directional sensitivity of the two
1100 instruments and the non-perfect cosine response could also be factors in why there are more significant differences between the measurements when the instruments are subject to direct illumination. Nevertheless, given the need to apply an adjustment to the SHIMS instrument calibration based on the BBR and radiative transfer (see Supplement Sect. 1) and uncertainty estimates as high as 10 %, the agreement in the spectral irradiances (within 2 % for all cases) is gratifying. This suggests that data from the instruments can be used for scientific purposes such as assessing the impact of aerosols on the spectral
1105 irradiances.

For up-welling irradiances, which benefitted from a reliable red-dome Eppley radiometer measurement (see supplementary material), the agreement between the measurements from SHIMS and SSFR are within 1 Wm^{-2} (or 5 %).

The general agreement between the instrumentation lends confidence to the measurements and the uncertainties in the measurements are small enough to suggest that radiative closure studies may be pursued using either the instrumentation on the BAe-146 or P3 platforms.

Generally, intercomparison of radiation measurements made by the LASIC ARM site were hampered by the frequent occurrence of orographically generated cloud, which is a persistent feature over Ascension Island.

Conclusions

Central to the purpose of the over-lapping field campaigns CLARIFY, ORACLES and LASIC was to provide combined datasets with which to undertake process studies and model evaluation work assessing the impact of biomass burning aerosols on climate. These datasets are distributed in space, being close to the coast of southern Africa, or in the far-field, and in time, across three years, as well as from early or later in the biomass burning season. Broad comparability between the measurements made during the CLARIFY, ORACLES and LASIC field experiments has been demonstrated. This gives confidence in any studies of the spatial and temporal evolution in parameters using combined datasets.

Temperature, humidity, and concentrations of CO were found to compare well enough to be able to confidently categorise airmasses by their pollution state and airmass history. This is important when using data from multiple regions, seasons, and periods. There were differences in CO that would benefit from further investigation. Black carbon, another pollution tracer, compared well between CLARIFY and LASIC, but NASA data were compromised during the intercomparison. Particle number concentrations, condensation nuclei, and the particle size distributions of submicron aerosols are comparable between all three field campaigns. There are larger differences between probes on a single platform than between two independent platforms suggesting that platform specific aspects such as mounting location, aircraft angle of attack and other specifics of installation are not resulting in significant biases to the sampling of accumulation mode aerosols.

Absorption coefficient measurements are comparable across all three platforms, although magnitudes of σ_{Ap} were low during the airborne inter-comparison. The wavelength dependence of absorption, characterised by Å$_{AP}$, followed similar trends for both airborne platforms and indicated an increasing absorption coefficient at shorter visible wavelengths. Conversely, observations from the LASIC ARM site show a reduction in absorption at shorter wavelengths. This may be a consequence of limited sampling time, or potentially size dependent sampling. The low absorption coefficient magnitude prevented study of the ω_0 and so caution must be exercised when combining data from multiple platforms. The comparison of submicron σ_{SP} is good between the FAAM BAe-146 and the NASA P3 suggesting that derived values of ω_0 can be trusted when larger amounts of material are present. LASIC and FAAM showed that the scattering measurements at the ARM site were of much lower magnitude than those onboard the BAe146, and that the comparison was worse at the longer red wavelength.

Composition observations are in general agreement between ORACLES and CLARIFY, leading to the conclusion that study of the evolution of the BBA plume as it advects away from the coast are possible using a combined dataset from both campaigns. The masses of chemical components at the LASIC ARM site were much larger than those reported by CLARIFY, in contrast to observations such as concentrations of condensation nuclei and black carbon particles, which tended to be ~20 % lower and black carbon mass concentrations which were 10 % lower. The cause of the greater masses recorded at the ARM site is unknown, and so caution is recommended when interpreting these datasets.

Previous work has shown that the FAAM SHIMS radiometer requires a bias correction to FAAM BBRs of ~30 %. Once this is applied, there is good agreement with the comparable measurements made by the P3 SSFR instrument. Comparable observations of the aerosol PSDS permit radiometric closure studies to be undertaken.

Observations of cloud particles were comparable between ORACLES and CLARIFY.

Further work is needed to characterise inlet systems on aircraft and at ground-based facilities, including improvements in understanding airflow around airframes, size-depend particle transmission, and characterisations of the RH within sampling lines.

1150 **Code Availability**

FAAM Airborne Laboratory; Post processing library for the data from the FAAM aircraft, available at: https://github.com/ncasuk/decades-pp, last access: 17 February 2020 and https://github.com/FAAM-146/decades-ppandas, last access 21 January 2022.

Data Availability

1155 ORACLES Science Team: Suite of Aerosol, Cloud, and Related Data Acquired Aboard P3 During ORACLES 2017, Version 3, NASA Ames Earth Science Project Office, Accessed at doi: 10.5067/Suborbital/ORACLES/P3/2017_V3 , 2020

Facility for Airborne Atmospheric Measurements; Natural Environment Research Council; Met Office (2017): FAAM C031 CLARIFY flight: Airborne atmospheric measurements from core instrument suite on board the BAe-146 aircraft. Centre for Environmental Data Analysis, 25 November 2021. https://catalogue.ceda.ac.uk/uuid/a070273597ab45619bbc4241d722bf61

1160 The LASIC ground-based data sets are publicly available from the Atmospheric Radiation Measurement Climate Research Facility (https://www.arm.gov/research/campaigns/amf2016lasic; Atmospheric Radiation Measurement Climate Research Facility, 2021).

SP2: https://iop.archive.arm.gov/arm-iop/2016/asi/lasic/sedlacek-sp2/?ticket=ST-122494-K0l8sp9x373VIQXXqqIzsIV55wcsso (Sedlacek, 2017),

1165 CO: https://doi.org/10.5439/1046183 (Springston, 2018b),

CAPS PM_{SSA}: https://adc.arm.gov/discovery/#/results/s::caps-ssa (Onasch, et al., 2015)

Supplement Link

See additional document.

Author Contribution

1170 SA, PB, JH, JR, GM, RW, PZ developed the concept and scope, designed the flights and ARM site intercomparison data collection. PB analysed the data and wrote the initial manuscript with contributions from SA, HCo, IC, AD, SH, AJ, JL, GN, HP, YS, KS, JT, HW, PZ. All authors performed instrument or data work for one or more instruments or systems on one or more platforms. All authors reviewed the manuscript.

Competing Interests

1175 The authors declare that they have no conflict of interest.

Special Issue Statement

New observations and related modelling studies of the aerosol–cloud–climate system in the Southeast Atlantic and southern Africa regions (ACP/AMT inter-journal SI).

Acknowledgements

1180 This research has been supported by the Natural Environment Research Council (grant no. NE/L013584/1 and NE/P013406/1), and the Norges Forskningsråd (grant no. 240372 and 244141). HC, IC, JH, AJ, JT, HW, KB and MC were supported through the CLARIFY-2017 Natural Environment Research Council large grant proposal (NE/L013797/1). ND was supported by a NERC/Met Office Industrial Case studentship (ref 640052003). JH, AJ and MC were also supported by the Research Council of Norway via the projects AC/BC (240372) and NetBC (244141).

1185 PZ and JZ were supported by the U.S. Department of Energy, Office of Science (grant nos. DE-SC0018272 and DE-SC0021250) with PZ acknowledging further support from NASA EVS-2 ORACLES grant NNX15AF98G. AD was supported by grant DE-SC0018272 and grant NNX15AF98G. SPC and KSS and HCh were supported by NASA grant NNX15AF62G. RW was supported by NASA grant NNX15AF96G-S13. SG and GM were supported by NASA grants 80NSSC18K0222, NNX15AF93G and NNX16A018H.

1190 Airborne data was obtained using the BAe-146-301 Atmospheric Research Aircraft flown by Airtask Ltd and managed by FAAM Airborne Laboratory, jointly operated by UKRI and the University of Leeds along with the Lockheed P-3 Orion (N426NA) operated by NASA Goddard Space Flight Center's Wallops Flight Facility Aircraft Office. Data were obtained from the atmospheric radiation measurement (ARM) user facility, a U.S. Department of Energy (DOE) Office of Science user facility managed by the biological and environmental research program. We thank David Sproson (FAAM) for reprocessing
1195 the FAAM BAe-146 datasets with the latest version of the decades-ppandas processing codes.

We acknowledge the use of imagery from the NASA Worldview application (https://worldview.earthdata.nasa.gov/), part of the NASA Earth Observing System Data and Information System (EOSDIS).

References

Abel, S., Cotton, R., Barrett, P., and Vance, A.: A comparison of ice water content measurement techniques on the
1200 FAAM BAe-146 aircraft, Atmos. Meas. Tech., 7, 3007–3022, https://doi.org/10.5194/amt-7-3007-2014, 2014.

Adebeyi, A. A. and Zuidema, P.: The role of the southern African easterly jet in modifying the southeast Atlantic aerosol and cloud environments, Q. J. R. Meteorol. Soc. 142, 69 (1574-1589), https://doi.org/10.1002/qj.2765, 2016.

Aiken, A. C., Decarlo, P. F., Kroll, J. H., Worsnop, D. R., Huffman, J. A., Docherty, K. S., Ulbrich, I. M., Mohr, C., Kimmel, J. R., Sueper, D., Sun, Y., Zhang, Q., Trimborn, A., Northway, M., Ziemann, P. J., Canagaratna, M. R., Onasch, T.
1205 B., Alfarra, M. R., Prevot, A. S. H., Dommen, J., Duplissy, J., Metzger, A., Baltensperger, U., and Jimenez, J. L.: O/C and OM/OC ratios of primary, secondary, and ambient organic aerosols with highresolution time-of-flight aerosol mass spectrometry, Environ. Sci. Technol., 42, 4478–4485, https://doi.org/10.1021/es703009q, 2008.

Alfarra, M. R., Prevôt, A. S. H., Szidat, S., Sandradewi, J., Weimer, S., Lanz, V. A., Schreiber, D., Mohr, M., and Baltensperger, U.: Identification of the mass spectral signature of organic aerosols from wood burning emissions, Environ.
1210 Sci. Technol., 41, 5770– 5777, https://doi.org/10.1021/es062289b, 2007.

Allan, J. D., Jimenez, J. L., Williams, P. I., Alfarra, M. R., Bower, K. N., Jayne, J. T., Coe, H., and Worsnop, D. R.: Quantitative sampling using an Aerodyne aerosol mass spectrometer, 1, Techniques of data interpretation and error analysis, J. Geophys. Res., 108(D3), 4090, doi:10.1029/2002JD002358, 2003.

Allan, J. D., Delia, A. E., Coe, H., Bower, K. N., Alfarra, M. R., Jimenez, J. L., Middlebrook, A. M., Drewnick, F., Onasch, T. B., Canagaratna, M. R., Jayne, J. T. and Worsnop, D. R.: A generalised method for the extraction of chemically resolved mass spectra from Aerodyne aerosol mass spectrometer data. J. Aerosol Sci., 35(7): 909-922, 2004.

Allen, G., Vaughan, G., Bower, K. N., Williams, P. I., Crosier, J., Flynn, M., Connolly, P., Hamilton, J. F., Lee, J. D., Saxton, J. E., Watson, N. M., Gallagher, M., Coe, H., Allan, J., Choularton, T. W., and Lewis, A. C.: Aerosol and trace-gas measurements in the Darwin area during the wet season, J. Geophys. Res. Atmos., 113, 1– 19, https://doi.org/10.1029/2007JD008706, 2008.

Allen, G., Coe, H., Clarke, A., Bretherton, C., Wood, R., Abel, S. J., Barrett, P., Brown, P., George, R., Freitag, S., McNaughton, C., Howell, S., Shank, L., Kapustin, V., Brekhovskikh, V., Kleinman, L., Lee, Y.-N., Springston, S., Toniazzo, T., Krejci, R., Fochesatto, J., Shaw, G., Krecl, P., Brooks, B., McMeeking, G., Bower, K. N., Williams, P. I., Crosier, J., Crawford, I., Connolly, P., Allan, J. D., Covert, D., Bandy, A. R., Russell, L. M., Trembath, J., Bart, M., McQuaid, J. B., Wang, J., and Chand, D.: South East Pacific atmospheric composition and variability sampled along 20∘ S during VOCALS-REx, Atmos. Chem. Phys., 11, 5237−5262, https://doi.org/10.5194/acp-11-5237-2011, 2011.

Allen, G., Pitt, J., Lee, J., Hopkins, J., Young, S., Bauguitte, S., Gallagher, M., Fisher, R., Lowry, D., and Nisbet, E.: The MOYA aircraft campaign: First measurements of methane, ethane and C-13 isotopes from West African biomass burning and other regional sources using the UK FAAM aircraft, EGUGA, Vienna, Austria, p. 8574, 2017.

Anderson, T. L. and Ogren, J. A.: Determining Aerosol Radiative Properties Using the TSI 3563 Integrating Nephelometer, Aerosol Science and Technology, 29:1, 57-69, DOI: 10.1080/02786829808965551, 1998.

Bahreini, R., Ervens, B., Middlebrook, A. M., Warneke, C., de Gouw, J. A., DeCarlo, P. F., Jimenez, J. L., Atlas, E., Brioude, J., Brock, C. A., Fried, A., Holloway, J. S., Peischl, J., Richter D., Ryerson, T. B., Stark, H., Walega, J., Weibring, P., Wollny , A. G. and Fehsenfeld, F. C.: Organic Aerosol Formation in Urban and Industrial plumes near Houston and Dallas, TX. Journal of Geophysical Research-Atmospheres 114, D00F16, doi:10.1029/2008JD011493, 2009.

Bansemar, A.: SODA2 System for OAP (optical array probe) Data Analysis, University Corporation for Atmospheric Research, available at: https://github.com/abansemer/soda2 (last access: 26 April 2021), 2016.

Baron, P.: Aerosol Calculator AeroCalc_2001_1, last_accessed: 27 April 2021, https://www.tsi.com/getmedia/540a30fa-8444-49f6-814f-891495c70aa1/Aerocalc2001_1, 2001.

Barrett, P. A., Blyth, A., Brown, P. R. A., and Abel, S. J.: The structure of turbulence and mixed-phase cloud microphysics in a highly supercooled altocumulus cloud, Atmos. Chem. Phys., 20, 1921–1939, https://doi.org/10.5194/acp-20-1921-2020, 2020.

Baumgardner, D., Abel, S. J., Axisa, D., Cotton, R., Crosier, J., Field, P., Gurganus, C., Heymsfield, A., Korolev, A., Krämer, M., Lawson, P., McFarquhar, G., Ulanowski, Z., and Um, J.: Cloud Ice Properties: In Situ Measurement Challenges, Meteorological Monographs, pp9.1-9.23, https://doi.org/10.1175/AMSMONOGRAPHS-D-16-0011.1, 2017.

Chuang, P. Y., Saw, E. W., Small, J. D., Shaw, R. A., Sipperley, C. M., Payne, G. A. and Bachalo, W. D.: Airborne Phase Doppler Interferometry for Cloud Microphysical Measurements, Aero. Sci. Tech. 42, 8 (685-703), https://doi.org/10.1080/02786820802232956, 2008.

Cochrane, S. P., Schmidt, K. S., Chen, H., Pilewskie, P., Kittelman, S., Redemann, J., LeBlanc, S., Pistone, K., Kacenelenbogen, M., Segal Rozenhaimer, M., Shinozuka, Y., Flynn, C., Platnick, S., Meyer, K., Ferrare, R., Burton, S., Hostetler, C., Howell, S., Freitag, S., Dobracki, A., and Doherty, S.: Above-cloud aerosol radiative effects based on ORACLES 2016 and ORACLES 2017 aircraft experiments, Atmos. Meas. Tech., 12, 6505–6528, https://doi.org/10.5194/amt-12-6505-2019, 2019.

Cotterell, M.I., Ward, G.P, Hibbins, A.P., Haywood, J.M., Wilson, A., and Langridge, J.K.: Optimizing the performance of aerosol photoacoustic cells using a finite element model. Part 1: Method and application to single-resonator multipass cells, Aero. Sci. Tech, 53:10, 1107-1127, https://doi.org/10.1080/02786826.2019.1650161, 2019a.

Cotterell, M.I., Ward, G.P, Hibbins, A.P., Wilson, A., Haywood, J.M., and Langridge, J.K.: Optimizing the performance of aerosol photoacoustic cells using a finite element model. Part 2: Application to a two resonator cell, Aero. Sci. Tech, 53:10, 1128-1148, https://doi.org/10.1080/02786826.2019.1648749, 2019b.

1260   Cotterell, M. I., Szpek, K., Haywood , J. M. and Langridge, J. M.: Sensitivity and accuracy of refractive index retrievals from measured extinction and absorption cross sections for mobility-selected internally mixed light absorbing aerosols, Aero. Sci. Tech., 54:9, 1034-1057, DOI: 10.1080/02786826.2020.1757034, 2020.

Cotterell, M. I., Szpek, K., Tiddeman, D., Haywood, J. M., and Langridge, J. M.: Photoacoustic Studies of Energy Transfer from Ozone Photoproducts to Bath Gases following Chappuis Band Photoexcitation. Physical Chemistry Chemical Physics.
1265   https://doi.org/10.1039/D0CP05056C, 2021.

Crosier, J., Bower, K. N., Choularton, T. W., Westbrook, C. D., Connolly, P. J., Cui, Z. Q., Crawford, I. P., Capes, G. L., Coe, H., Dorsey, J. R., Williams, P. I., Illingworth, A. J., Gallagher, M. W., and Blyth, A.M.: Observations of ice multiplication in a weakly convective cell embedded in supercooled mid-level stratus, Atmos. Chem. Phys., 11, 257–273, https://doi.org/10.5194/acp-11-257-2011, 2011.

1270   Davies, N. W., Cotterell, M. I., Fox, C., Szpek, K., Haywood, J. M. and Langridge, J. M.: On the accuracy of aerosol photoacoustic spectrometer calibrations using absorption by ozone, Atmos. Meas. Tech., 11, 2313–2324 , https://doi.org/10.5194/amt-11-2313-2018, 2018a.

Davies, N. W.: The climate impacts of atmospheric aerosols using in-situ measurements, satellite retrievals and global climate model simulations (Thesis), University of Exeter, http://hdl.handle.net/10871/34544, 2018b

1275   Davies, N.W., Fox, C., Szpek, K., Cotterell, M. I., Taylor, J. W., Allan, J. D., Williams, P. I., Trembath, J., Haywood, J. M., and Langridge, J. M.: Evaluating biases in filter-based aerosol absorption measurements using photoacoustic spectroscopy, Atmos. Meas. Tech., 12, 3417-3434, DOI: 10.5194/amt-12-3417-2019, 2019.

DeCarlo, P. F., Kimmel, J. R., Trimborn, A., Northway, M. J., Jayne, J. T., Aiken, A. C., Gonin, M., Fuhrer, K., Horvath, T., Docherty, K. S., Worsnop, D. R. and Jimenez, J. L.: Field-deployable, high-resolution, time-of-flight aerosol mass
1280   spectrometer. Anal Chem, 78, 24, 8281-9, 2006.

Diamond, M. S., Dobracki, A., Freitag, S., Small Griswold, J. D., Heikkila, A., Howell, S. G., Kacarab, M. E., Podolske, J. R., Saide, P. E., and Wood, R.: Time-dependent entrainment of smoke presents an observational challenge for assessing aerosol–cloud interactions over the southeast Atlantic Ocean. Atmos. Chem. and Phys., 18(19), 14623–14636, https://doi.org/10.5194/acp-18-14623-2018, 2018.

1285   DMT: Passive Cavity Aerosol Spectrometer Probe (PCASP-100X) Operator Manual DOC-0228, Rev C https://www.dropletmeasurement.com/manual/operations-manual-passive-cavity-aerosol-spectrometer-probe-pcasp-100x/ Last_accessed: 26 April 2021.

Dobracki, A., Zuidema, P., Howell, S., Saide, P., Freitag, S., Aiken, A.C., Burton, S., Sedlacek III, A.J., Redemann, J., Wood, R.: Non-reversible aging can increase solar absorption in African biomass burning plumes of intermediate age.
1290   Atmos. Chem. Phys. Disc., [preprint], doi:10.5194/acp-2021-1081, in review, 2022.

Drewnick, F., Hings, S. S., DeCarlo, P., Jayne, J. T., Gonin, M., Fuhrer, K., Weimer, S., Jimenez, J. L., Demerjian, K. L., Borrmann, S., and Worsnop, D. R.: A New Time-of-Flight Aerosol Mass Spectrometer (TOF-AMS)—Instrument Description and First Field Deployment, Aerosol Science and Technology, 39, 637-658, 10.1080/02786820500182040, 635
2005.

1295   Farmer, D. K., Matsunaga, A., Docherty, K. S., Surratt, J. D., Seinfeld, J. H., Ziemann, P. J. and Jimenez, J. L.: Response of an aerosol mass spectrometer to organonitrates and organosulfates and implications for atmospheric chemistry. Proc Natl Acad Sci USA, 107, 15, 6670-6675, 2010.

Foot, J. S., Hignett, P. and Kilsby, C.G.: Investigation into errors associated with upward=facing pyranometers fitted to the Met Office, MRF Internal Notes 31, https://library.metoffice.gov.uk/Portal/Default/en-GB/RecordView/Index/649422#, ©
1300   Crown Copyright 1986. Information provided by the National Meteorological Library and Archive – Met Office, UK

Formenti, P., D'Anna, B., Flamant, C., Mallet, M., Piketh, S. J., Schepanski, K., Waquet, F., Auriol, F., Brogniez, G., Burnet, F., Chaboureau, J. -P., Chauvigné, A., Chazette, P., Denjean, C., Desboeufs, K., Doussin, J. -F., Elguindi, N., Feuerstein, S., Gaetani, M., Giorio, C., Klopper, D., Mallet, M. D., Nabat, P., Monod, A., Solmon, F., Namwoonde, A., Chikwililwa, C., Mushi, R., Welton, E. J., and Holben, B.: The Aerosols, Radiation and Clouds in Southern Africa Field Campaign in Namibia: Overview, Illustrative Observations, and Way Forward, BAMS, 100, 7 (1277–1298), https://doi.org/10.1175/BAMS-D-17-0278.1, 2019.

Gupta, S., McFarquhar, G. M., O'Brien, J. R., Delene, D. J., Poellot, M. R., Dobracki, A., Podolske, J. R., Redemann, J., LeBlanc, S. E., Segal-Rozenhaimer, M., and Pistone, K.: Impact of the variability in vertical separation between biomass burning aerosols and marine stratocumulus on cloud microphysical properties over the Southeast Atlantic, Atmos. Chem. Phys., 21, 4615–4635, https://doi.org/10.5194/acp-21-4615-2021, 2021a.

Gupta, S., McFarquhar, G. M., O'Brien, J. R., Poellot, M. R., Delene, D. J., Miller, R. M., and Griswold, J. D. S.: Precipitation Susceptibility of Marine Stratocumulus with Variable Above and Below-Cloud Aerosol Concentrations over the Southeast Atlantic, Atmos. Chem. Phys. Discuss., https://doi.org/10.5194/acp-2021-677, 2021b.

Gysel, M, Laborde, M., Olfert, J. S., Subramanian, R., and Grohn, A. J.: Effective density of Aquadag and fullerene soot black carbon reference materials used for SP2 calibration. Atmos. Meas. Tech, 4, 12, 2851-2858, doi:10.5194/amt-4-2851-2011. 2011.

Haywood, J. M., Francis, P. N., Glew, M. D., and Taylor, J. P.: Optical properties and direct radiative effect of Saharan Dust: A case study of two Saharan dust outbreaks using aircraft data. J. Geophys. Res., 106, 18,417-18428, 2001.

Haywood, J. M., Francis, P., Osborne, S. R., Glew, M., Loeb, N., Highwood, E., Tanré, D., Myhre, G., Formenti, P., and Hirst, E.: Radiative properties and direct radiative effect of Saharan dust measured by the C-130 aircraft during SHADE: 1. Solar spectrum, J. Geophys. Res., 108(D18), 8577, doi:10.1029/2002JD002687, 2003.

Haywood, J. M., Pelon, J., Formenti, P., Bharmal, N., Brooks, M., Capes, G., Chazette, P., Chou, C., Christopher, S., Coe, H., Cuesta, J., Derimian, Y., Desboeufs, K., Greed, G., Harrison, M., Heese, B., Highwood, E. J., Johnson, B., Mallet, M., Marticorena, B., Marsham, J., Milton, S., Myhre, G., Osborne, S. R., Parker, D. J., Rajot, J.-L., Schulz, M., Slingo, A., Tanré, D., Tulet, P.: Overview of the Dust and Biomass burning Experiment and African Multidisciplinary Monsoon Analysis Special Observational Period-0, J. Geophys. Res, 113, doi:10.1029/2008JD01007, 2008.

Haywood, J. M., Johnson, B. T., Osborne, S. R., Baran, A. J., Brooks, M., Milton, S. F., Mulcahy, J., Walters, D., Allan, R. P., Woodage, M. J., Klaver, A., Formenti, P., Brindley, H. E., Christopher, S., Gupta, P.: Motivation, rationale and key results from the GERBILS Saharan dust measurement campaign, Q. J. R. Meteorol. Soc. DOI:10.1002/qj.797, 137, 1106-1116, 2011.

Haywood, J. M., Abel, S. J., Barrett, P. A., Bellouin, N., Blyth, A., Bower, K. N., Brooks, M., Carslaw, K., Che, H., Coe, H., Cotterell, M. I., Crawford, I., Cui, Z., Davies, N., Dingley, B., Field, P., Formenti, P., Gordon, H., de Graaf, M., Herbert, R., Johnson, B., Jones, A. C., Langridge, J. M., Malavelle, F., Partridge, D. G., Peers, F., Redemann, J., Stier, P., Szpek, K., Taylor, J. W., Watson-Parris, D., Wood, R., Wu, H., and Zuidema, P.: The CLoud–Aerosol–Radiation Interaction and Forcing: Year 2017 (CLARIFY-2017) measurement campaign, Atmos. Chem. Phys., 21, 1049–1084, https://doi.org/10.5194/acp-21-1049-2021, 2021.

Hazi, Y., Heikkinen, M. S. A., Cohen, B. S., Size distribution of acidic sulfate ions in fine ambient particulate matter and assessment of source region effect, Atmos. Env. 37 (5403-5413), 2003.

Howell, S. G., Freitag, S., Dobracki, A., Smirnow, N., and Sedlacek III, A. J.: Undersizing of Aged African Biomass Burning Aerosol by an Ultra High Sensitivity Aerosol Spectrometer, Atmos. Meas. Tech., 14, 7381–7404, https://doi.org/10.5194/amt-14-7381-2021, 2021.

Jimenez, J. L., Canagaratna, M. R., Donahue, N. M., Prévôt, A. S. H., Zhang, Q., Kroll, J. H., DeCarlo, P. F., Allan, J. D., Coe, H., Ng, N. L., Aiken, A. C., Docherty, K. D., Ulbrich, I. M., Grieshop, A. P., Robinson, A. L., Duplissy, J., Smith, J. D., Wilson, K. R., Lanz, V. A., Hueglin, C., Sun, Y.L., Tian, J., Laaksonen, A., Raatikainen, T., Rautiainen, J., Vaattovaara, P., Ehn, M., Kulmala, M., Tomlinson, J. M., Collins, D. R., Cubison, M. J., Dunlea, E. J., Huffman J. A., Onasch, T. B.,

Alfarra, M. R., Williams, P. I., Bower, K., Kondo, Y., Schneider, J., Drewnick, F., Borrmann, S., Weimer, S., Demerjian, K., Salcedo, D., Cottrell, L., Griffin, R., Takami, A., Miyoshi, T., Hatakeyama, S., Shimono, A., Sun, J. Y., Zhang, Y. M., Dzepina, K., Kimmel, J. R., Sueper, D., Jayne, J. T., Herndon, S. C., Trimborn, A. M., Williams, L. R., Wood, E. C., Kolb, C. E., Middlebrook, A. M., Baltensperger, U., and D. R. Worsnop.: Evolution of Organic Aerosols in the
1350 Atmosphere,Science, 326, 1525-1529, DOI: 10.1126/science.1180353, 2009.

Jones, A. C., Haywood, J. M., Vance, A., and Ryder, C.: Pitch and roll corrections for the CLARIFY-2017 radiation data, Met Office, OBR Technical Note 91, https://library.metoffice.gov.uk/Portal/Default/en-GB/RecordView/Index/646187, © Crown Copyright 2018. Information provided by the National Meteorological Library and Archive – Met Office, UK

King, W. D., Maher, C. T., and Hepburn, G. A.: Further Performance Tests on the CSIRO Liquid Water Probe. J. Appl.
1355 Meteor., 20, 195–202, https://doi.org/10.1175/1520-0450(1981)020<0195:FPTOTC>2.0.CO;2, 1981.

Klein, S. A., and D. L. Hartmann, The seasonal cycle of low stratiform clouds. J. Climate, 6, 1587–1606, 1993.

Laborde, M., Schnaiter, M., Linke, C., Saathoff, H., Naumann, K. -H., Möhler, O., Berlenz, S., Wagner, U., Taylor, J. W., Liu, D., Flynn, M., Allan, J. D., Coe, H., Heimerl, K., Dahlkötter, F., Weinzierl, B., Wollny, A. G., Zanatta, M., Cozic, J., Laj, P., Hitzenberger, R., Schwarz, J. P., and Gysel, M.: Single Particle Soot Photometer intercomparison at the AIDA
1360 chamber, 5, (12), www.atmos-meas-tech.net/5/3077/2012/ , 2012.

Lance, S., Brock, C. A., Rogers, D., and Gordon, J. A.: Water droplet calibration of the Cloud Droplet Probe (CDP) and in-flight performance in liquid, ice and mixed-phase clouds during ARCPAC, Atmos. Meas. Tech., 3, 1683–1706, https://doi.org/10.5194/amt-3-1683-2010, 2010.

Lance, S.: Coincidence Errors in a Cloud Droplet Probe (CDP) and a Cloud and Aerosol Spectrometer (CAS), and the
1365 Improved Performance of a Modified CDP. J. Atmos. Oceanic Technol., 29, 1532–1541, https://doi.org/10.1175/JTECH-D-11-00208.1, 2012.

Langridge, J. M, Richardson, M. S., Lack, D., Law, D., and Murphy, D. M.: Aircraft Instrument for Comprehensive Characterization of Aerosol Optical Properties, Part I: Wavelength-Dependent Optical Extinction and Its Relative Humidity Dependence Measured Using Cavity Ringdown Spectroscopy, Aero. Sci. Tech., 45:11, 1305-1318,
1370 https://doi.org/10.1080/02786826.2011.592745, 2011.

Lawson, R.P., O'Connorm, D., Zmarzly, P., Weaver, K., Baker, B., Mo, Q., and Jonsson, H.: The 2D-S (Stereo) Probe: Design and Preliminary Tests of a New Airborne, High-Speed, High-Resolution Particle Imaging Probe. J. Atmos. Oceanic Technol., 23, 1462–1477, 2006.

Liu, P. S. K., Leaitch, W. R., Strapp, J. W. and Wasey, M. A.: Response of Particle Measuring Systems Airborne ASASP
1375 and PCASP to NaCl and Latex Particles, Aerosol Science and Technology, 16:2, 83-95, DOI: 10.1080/02786829208959539, 1992.

Liu, X., Huey, L. G., Yokelson, R. J., Selimovic, V., Simpson, I. J., Müller, M., Jimenez, J. L., Campuzano-Jost, P., Beyersdorf, A. J., Blake, D. R., Butterfield, Z., Choi, T., Crounse, J. D., Day, D. A., Diskin, G. S., Dubey, M. K., Fortner, E., Hanisco, T. F., Hu, W., King, L. E., Kleinman, L., Meinardi, S., Mikoviny, T., Onasch, T. B., Palm, B. B., Peischl, J.,
1380 Pollack, I. B., Ryerson, T. B., Sachse, G. W., Sedlacek, A. J., Shilling, J. E., Springston, S., St. Clair, J. M., Tanner, D. J., Teng, A. P., Wennberg, P. O., Wisthaler, A. and Wolfe, G. M.; Airborne measurements of western U.S. wildfire emissions: Comparison with prescribed burning and air quality implications, J. Geophys. Res.-Atmos., 122, 6108–6129, https://doi.org/10.1002/2016JD026315, 2017.

Marshak, A., and Davis, A. (Eds.): 3D radiative transfer in cloudy atmospheres. Springer Science and Business Media, 2005.

1385 McFarquhar, G. M., Finlon, J. A., Stechman, D. M., Wu, W., Jackson, R. C., and Freer, M.: University of Illinois/Oklahoma Optical Array Probe (OAP) Processing Software, https://doi.org/10.5281/zenodo.1285969, 2018.

McNaughton, C. S., Clarke, A. D., Howell, S. G., Pinkerton, M., Anderson, B., Thornhill, L., Hudgins, C., Winstead, E., Dibb, J. E., Scheuer, E., and Maring, H.: Results from the DC-8 Inlet Characterization Experiment (DICE): Airborne Versus

Surface Sampling of Mineral Dust and Sea Salt Aerosols, Aerosol Science and Technology, 41:2, 136-159, DOI:
1390   10.1080/02786820601118406, 2007.

McNaughton, C. S., Clarke, A. D., Kapustin, V., Shinozuka, Y., Howell, S. G., Anderson, B. E., Winstead, E., Dibb, J.,
Scheuer, E., Cohen, R. C., Wooldridge, P., Perring, A., Huey, L. G., Kim, S., Jimenez, J. L., Dunlea, E. J., DeCarlo, P. F.,
Wennberg, P. O., Crounse, J. D., Weinheimer, A. J., and Flocke, F.: Observations of heterogeneous reactions between Asian
pollution and mineral dust over the Eastern North Pacific during INTEX-B, Atmos. Chem. Phys., 9, 8283–8308,
1395   https://doi.org/10.5194/acp-9-8283-2009, 2009.

McNaughton, C. S., Clarke, A. D., Freitag, S., Kapustin, V. N., Kondo, Y., Moteki, N., Sahu, L., Takegawa, N., Schwarz, J.
P., Spackman, J. R., Watts, L., Diskin, G., Podolske, J., Holloway, J. S., Wisthaler, A., Mikoviny, T., de Gouw, J., Warneke,
C., Jimenez, J., Cubison, M., Howell, S. G., Middlebrook, A., Bahreini, R., Anderson, B. E., Winstead, E., Thornhill, K. L.,
Lack, D., Cozic, J., and Brock, C. A.: Absorbing aerosol in the troposphere of the Western Arctic during the 2008
1400   ARCTAS/ARCPAC airborne field campaigns, Atmos. Chem. Phys., 11, 7561–7582, https://doi.org/10.5194/acp-11-7561-
2011, 2011.

Middlebrook, A. M., Bahreini, R., Jimenez, J. L., and Canagaratna, M. R.: Evaluation of composition-dependent collection
efficiencies for the aerodyne aerosol mass spectrometer using field data, Aerosol Sci. Tech., 46, 258–271,
https://doi.org/10.1080/02786826.2011.620041, 2012.

1405   Miller, M. A., Nitschke, K., Ackerman, T. P., Ferrell, W. R., Hickmon, N., and Ivey, M.: The ARM Mobile Facilities,
Meteor. Mon., 57, 9.1–9.15, https://doi.org/10.1175/AMSMONOGRAPHS-D-15-0051.1, 2016.

Miller, R. M., McFarquhar, G. M., Rauber, R. M., O'Brien, J. R., Gupta, S., Segal-Rozenhaimer, M., Dobracki, A. N.,
Sedlacek, A. J., Burton, S. P., Howell, S. G., Freitag, S., and Dang, C.: Observations of supermicron-sized aerosols
originating from biomass burning in southern Central Africa, Atmos. Chem. Phys., 21, 14815–14831,
1410   https://doi.org/10.5194/acp-21-14815-2021 , 2021.

Moore, R. H., Wiggins, E. B., Ahern, A. T., Zimmerman, S., Montgomery, L., Campuzano Jost, P., Robinson, C. E.,
Ziemba, L. D., Winstead, E. L., Anderson, B. E., Brock, C. A., Brown, M. D., Chen, G., Crosbie, E. C., Guo, H., Jimenez, J.
L., Jordan, C. E., Lyu, M., Nault, B. A., Rothfuss, N. E., Sanchez, K. J., Schueneman, M., Shingler, T. J., Shook, M. A.,
Thornhill, K. L., Wagner, N. L., and Wang, J.: Sizing response of the Ultra-High Sensitivity Aerosol Spectrometer (UHSAS)
1415   and Laser Aerosol Spectrometer (LAS) to changes in submicron aerosol composition and refractive index, Atmos. Meas.
Tech., 14, 4517–4542, https://doi.org/10.5194/amt-14-4517-2021, 2021.

Morgan, W. T, , J. D. Allan, Bower, K. N., Capes, G., Crosier, J., Williams, P. I., and Coe, H.: Vertical distribution of
submicron aerosol chemical composition from North-Western Europe and the North-East Atlantic, Atmos. Chem. Phys., 9,
5389–5401, https://doi.org/10.5194/acp-9-5389-2009, 2009.

1420   NASA Handbook, P-3B Orion (N426NA) Airborne Laboratory Experimenter Handbook 548-HDBK-0001 Release:
Baseline, https://airbornescience.nasa.gov/sites/default/files/P-3B%20Experimenter%20Handbook%20548-HDBK-0001.pdf,
last accessed: 2nd Feb 2021, Effective Date: August 2010.

Ng, N. L., Herndon, S. C., Trimborn, A., Canagaratna, M. R., Croteau, P. L., Onasch, T. B., Sueper, D., Worsnop, D. R.,
Zhang, Q., Sun, Y. L., and Jayne J. T.: An Aerosol Chemical Speciation Monitor (ACSM) for Routine Monitoring of the
1425   Composition and Mass Concentrations of Ambient Aerosol, Aero. Sci. Technol., 45:7, 780-
794, DOI: 10.1080/02786826.2011.560211, 2011.

Ogren, J. A.: Comment on "Calibration and Intercomparison of Filter-Based Measurements of Visible Light Absorption by
Aerosols", Aerosol Science and Technology, 44:8, 589-591, DOI: 10.1080/02786826.2010.482111 2010.

Onasch, T., Massoli, P., Kebabian, P., Hills, F., Bacon, F., and Freedman, A.: Single Scattering Albedo Monitor for Airborne
1430   Particulates, Aerosol Sci.Technol., 49, 267-279, 2015

Peers, F., Francis, P., Fox, C., Abel, S. J., Szpek, K., Cotterell, M. I., Davies, N. W., Langridge, J. M., Meyer, K. G.,
Platnick, S. E., and Haywood, J. M.: Observation of absorbing aerosols above clouds over the south-east Atlantic Ocean

from the geostationary satellite SEVIRI – Part 1: Method description and sensitivity, Atmos. Chem. Phys., 19, 9595–9611, https://doi.org/10.5194/acp-19-9595-2019 , 2019.

1435   Pennypacker, S., Diamond, M., and Wood, R.: Ultra-clean and smoky marine boundary layers frequently occur in the same season over the southeast Atlantic, Atmos. Chem. Phys., 20, 2341–2351, https://doi.org/10.5194/acp-20-2341-2020, 2020.

Pilewskie. P., Pommier, J., Bergstrom, R., Gore, W., Howard, S., Rabbette, M., Schmid, B., Hobbs, P. V., Tsay, S. C.: Solar spectral radiative forcing during the Southern African Regional Science Initiative, J. Geophys. Res., 108, D13, https://doi.org/10.1029/2002JD002411, 2003.

1440   Pistone, K., Redemann, J., Doherty, S., Zuidema, P., Burton, S., Cairns, B., Cochrane, S., Ferrare, R., Flynn, C., Freitag, S., Howell, S. G., Kacenelenbogen, M., LeBlanc, S., Liu, X., Schmidt, K. S., Sedlacek III, A. J., Segal-Rozenhaimer, M., Shinozuka, Y., Stamnes, S., van Diedenhoven, B., Van Harten, G., and Xu, F.: Intercomparison of biomass burning aerosol optical properties from in situ and remote-sensing instruments in ORACLES-2016, Atmos. Chem. Phys., 19, 9181–9208, https://doi.org/10.5194/acp-19-9181-2019, 2019.

1445   Pistone, K., Zuidema, P., Wood, R., Diamond, M., da Silva, A. M., Ferrada, G., Saide, P., Ueyama, R., Ryoo, J. -M., Pfister, L., Podolske, J., Noone, D., Bennett, R., Stith, E., Carmichael, G., Redemann, J., Flynn, C., LeBlanc, S., Segal-Rozenhaimer, M., and Shinozuka, Y.: Exploring the elevated water vapor signal associated with the free tropospheric biomass burning plume over the southeast Atlantic Ocean, Atmos. Chem. Phys., 21, 9643-9668, doi.org/10.5194/acp-21-9643-2021, 2021.

Price, H., FAAM Handbook, zenodo, 2022

1450   Redemann, J., Wood, R., Zuidema, P., Doherty, S. J., Luna, B., LeBlanc, S. E., Diamond, M. S., Shinozuka, Y., Chang, I. Y., Ueyama, R., Pfister, L., Ryoo, J. -M., Dobracki, A. N., da Silva, A. M., Longo, K. ., Kacenelenbogen, M. S., Flynn, C. J., Pistone, K., Knox, N. M., Piketh, S. J., Haywood, J. M., Formenti, P., Mallet, M., Stier, P., Ackerman, A. S., Bauer, S. E., Fridlind, A. M., Carmichael, G. R., Saide, P. E., Ferrada, G. A., Howell, S. G., Freitag, S., Cairns, B., Holben, B. N., Knobelspiesse, K. D., Tanelli, S., L'Ecuyer, T. S., Dzambo, A. M., Sy, O. O., McFarquhar, G. M., Poellot, M. R., Gupta, S.,
1455   O'Brien, J. R., Nenes, A., Kacarab, M., Wong, J. P. S., Small-Griswold, J. D., Thornhill, K. L., Noone, D., Podolske, J. R., Schmidt, K. S., Pilewskie, P., Chen, H., Cochrane, S. P., Sedlacek, A. J., Lang, T. J., Stith, E., Segal-Rozenhaimer, M., Ferrare, R. A., Burton, S. P., Hostetler, C. A., Diner, D. J., Seidel, F. C., Platnick, S. E., Myers, J. S., Meyer, K. G., Spangenberg, D. A., Maring, H., and Gao, L.: An overview of the ORACLES (ObseRvations of Aerosols above CLouds and their intEractionS) project: aerosol–cloud–radiation interactions in the southeast Atlantic basin, Atmos. Chem. Phys., 21,
1460   1507–1563, https://doi.org/10.5194/acp-21-1507-2021, 2021.

Ryder, C. L., Highwood, E. J., Rosenberg, P. D., Trembath, J., Brooke, J. K., Bart, M., Dean, A., Crosier, J., Dorsey, J., Brindley, H., Banks, J., Marsham, J. H., McQuaid, J. B., Sodemann, H., and Washington, R.: Optical properties of Saharan dust aerosol and contribution from the coarse mode as measured during the Fennec 2011 aircraft campaign, Atmos. Chem. Phys., 13, 303–325, https://doi.org/10.5194/acp-13-303-2013, 2013.

1465   Sedlacek, A.: Single-Particle Soot Photometer (SP2) Instrument Handbook. United States, ARM Tech. Rep. DOE/SC-ARM-TR-169, 24 pp, https://doi.org/10.2172/1344179, 2017.

Schwarz, J. P., Gao, R. S., Fahey, D. W., Thomson, D. S., Watts, L. A., Wilson, J. C., Reeves, J. M., Darbeheshti, M., Baumgardner, D. G., Kok, G. L., Chung, S. H., Schulz, M., Hendricks, J., Lauer, A., Kärcher, B., Slowik, J.G., Rosenlof, K. H., Thompson, T. L., Langford, A. O., Loewenstein, M., Aikin, K. C.: Single-particle measurements of midlatitude black
1470   carbon and light-scattering aerosols from the boundary layer to the lower stratosphere, J. Geo. Res., https://doi.org/10.1029/2006JD007076, 2006.

Sherman, J. P. and McComiskey, A.: Measurement-based climatology of aerosol direct radiative effect, its sensitivities, and uncertainties from a background southeast US site, Atmos. Chem. Phys., 18, 4131–4152, https://doi.org/10.5194/acp-18-4131-2018, 2018.

1475   Shinozuka, Y., Saide, P. E., Ferrada, G. A., Burton, S. P., Ferrare, R., Doherty, S. J., Gordon, H., Longo, K., Mallet, M., Feng, Y., Wang, Q., Cheng, Y., Dobracki, A., Freitag, S., Howell, S. G., LeBlanc, S., Flynn, C., Segal-Rosenhaimer, M., Pistone, K., Podolske, J. R., Stith, E. J., Bennett, J. R., Carmichael, G. R., da Silva, A., Govindaraju, R., Leung, R., Zhang,

Y., Pfister, L., Ryoo, J. -M., Redemann, J., Wood, R., and Zuidema, P.: Modeling the smoky troposphere of the southeast Atlantic: a comparison to ORACLES airborne observations from September of 2016, Atmos. Chem. Phys., 20, 11491–
1480   11526, https://doi.org/10.5194/acp-20-11491-2020, 2020.

Strapp, J. W., Oldenburg, J., Ide, R., Lilie, L., Bacic, S., Vukovic, Z., Oleskiw, M., Miller, D., Emery, E., Leone, G.: Wind Tunnel Measurements of the Response of Hot-Wire Liquid Water Content Instruments to Large Droplets, J Atmos. Sci., 20, 6: 791–806, https://doi.org/10.1175/1520-0426(2003)020<0791:WTMOTR>2.0.CO;2, 2003.

Stier, P., Schutgens, N. A. J., Bellouin, N., Bian, H., Boucher, O., Chin, M., Ghan, S., Huneeus, N., Kinne, S., Lin, G., Ma,
1485   X., Myhre, G., Penner, J. E., Randles, C. A., Samset, B., Schulz, M., Takemura, T., Yu, F., Yu, H., and Zhou, C.: Host model uncertainties in aerosol radiative forcing estimates: results from the AeroCom Prescribed intercomparison study, Atmos. Chem. Phys., 13, 3245–3270, https://doi.org/10.5194/acp-13-3245-2013, 2013.

Springston, S. R.: Particle Soot Absorption Photometer (PSAP) Instrument Handbook, https://www.osti.gov/servlets/purl/1246162, last accessed: 05/05/2021, DOE/SC-ARM-TR-176, 2018a.

1490   Springston, S.: AOS: Carbon Monoxide Analyzer, Atmospheric Radiation Measurement Data Archive, https://doi.org/10.5439/1046183, last access: 4 September 2018, 2018b.

Taylor, J. W., Choularton, T. W., Blyth, A. M., Liu, Z., Bower, K. N., Crosier, J., Gallagher, M. W., Williams, P. I., Dorsey, J. R., Flynn, M. J., Bennett, L. J., Huang, Y., French, J., Korolev, A., and Brown, P. R. A.: Observations of cloud microphysics and ice formation during COPE, Atmos. Chem. Phys., 16, 799–826, https://doi.org/10.5194/acp-16-799-2016,
1495   2016.

Taylor, J. W., Wu, H., Szpek, K., Bower, K. N., Crawford, I., Flynn, M. J., Williams, P. I., Dorsey, J., Langridge, J. M., Cotterell, M. I., Fox, C., Davies, N. W., Haywood J. M., and Coe, H.: Absorption closure in highly aged biomass burning smoke, Atmos. Chem. Phys. https://doi.org/10.5194/acp-2020-333, 2020.

Trembath, J., Bart, M., and Brooke, J.: FAAM Technical Note 01: Efficiencies of Modified Rosemount Housings for
1500   Sampling Aerosol on a Fast Atmospheric Research Aircraft, Tech. Rep., Facility for Airborne Atmospheric Measurement (FAAM), www.faam.ac.uk, 2012.

Trembath, J.: Airborne CCN Measurements, University of Manchester, PhD Thesis, https://www.escholar.manchester.ac.uk/item/?pid=uk-ac-man-scw:212956, 2013.

Uin, J., Smith, S.: Southern Great Plains (SGP) Aerosol Observing System (AOS) Instrument Handbook,
1505   https://www.arm.gov/publications/tech_reports/handbooks/doe-sc-arm-tr-267.pdf, last accessed: 05/05/2021, DOE/SC-ARM-TR-267, 2020.

Vance, A. K., Abel, S. J., Cotton, R. J., and Woolley, A. M.: Performance of WVSS-II hygrometers on the FAAM research aircraft, Atmos. Meas. Tech., 8, 1617–1625, https://doi.org/10.5194/amt-8-1617-2015, 2015.

Vance, A.K., Norwood-Brown, J., and O'Sullivan, D.: SWS-SHIMS Calibration and Uncertainties – Interim Report to
1510   Christmas 2017, Met Office, OBR Technical Note 90, https://library.metoffice.gov.uk/Portal/Default/en-GB/RecordView/Index/650108, © Crown Copyright 2017. Information provided by the National Meteorological Library and Archive – Met Office, UK

Vance, A., Price, H., Woolley, A., and Szpek, K.: Update on the performance of the WVSS-II hygrometers fitted to the FAAM BAe 146, Met Office, OBR Technical Note 93, https://library.metoffice.gov.uk/Portal/Default/en-
1515   GB/RecordView/Index/647266, © Crown Copyright 2018. Information provided by the National Meteorological Library and Archive – Met Office, UK

Virkkula, A.: Correction of the Calibration of the 3wavelength Particle Soot Absorption Photometer (3λ PSAP), Aerosol Sci. Technol., 44:8, 706–712, https://doi.org/10.1080/02786826.2010.482110, 2010.

Watson, T. B.: Aerosol Chemical Speciation Monitor (ACSM) Instrument Handbook, ARM CRM DOE/SC-ARM-TR-196,
1520   last_Accessed: 20/05/2021, https://www.arm.gov/publications/tech_reports/handbooks/acsm_handbook.pdf, 2017.

Weigel, R., Spichtinger, P., Mahnke, C., Klingebiel, M., Afchine, A., Petzold, A., Krämer, M., Costa, A., Molleker, S., Reutter, P., Szakáll, M., Port, M., Grulich, L., Jurkat, T., Minikin, A., and Borrmann, S.: Thermodynamic correction of particle concentrations measured by underwing probes on fast-flying aircraft, Atmos. Meas. Tech., 9, 5135–5162, https://doi.org/10.5194/amt-9-5135-2016 , 2016.

1525   Wu, H., Taylor, J. W., Szpek, K., Langridge, J., Williams, P. I., Flynn, M., Allan, J. D., Abel, S. J., Pitt, J., Cotterell, M. I., Fox, C., Davies, N. W., Haywood, J., Coe, H.: Vertical variability of the properties of highly aged biomass burning aerosol transported over the southeast Atlantic during CLARIFY-2017, Atmos. Chem. Phys., 20, 12697–12719, https://doi.org/10.5194/acp-20-12697-2020 , 2020.

Wu, H., Taylor, J. W., Langridge, J. M., Yu, C., Allan, J. D., Szpek, K., Cotterell, M. I., Williams, P. I., Flynn, M., Barker,
1530   P., Fox, C., Allen, G., Lee, J., and Coe, H.: Rapid transformation of ambient absorbing aerosols from West African biomass burning, Atmos. Chem. Phys., https://doi.org/10.5194/acp-21-9417-2021, 2021.

Wyant, M. C., Bretherton, C. S., Rand, H. A., and Stevens, D. E.: Numerical Simulations and a Conceptual Model of the Stratocumulus to Trade Cumulus Transition, JAS, 168–192, https://doi.org/10.1175/1520-0469(1997)054<0168:NSAACM>2.0.CO;2 , 1997.

1535   Zhang, J. and Zuidema, P.: The diurnal cycle of the smoky marine boundary layer observed during August in the remote southeast Atlantic, Atmos. Chem. Phys., 19, 14493–14516, https://doi.org/10.5194/acp-19-14493-2019, 2019.

Zuidema, P., Redemann, J., Haywood, J., Wood, R., Piketh, S., Hipondoka, M., and Formenti, P.: Smoke and Clouds above the Southeast Atlantic: Upcoming Field Campaigns Probe Absorbing Aerosol's Impact on Climate, BAMS 97, 7, 10.1175/BAMS-D-15-00082.1, 2016.

1540   Zuidema, P., Sedlacek III, A. J., Flynn, C., Springston, S., Delgadillo, R., Zhang, J., Aiken, A. C., Koontz, A., and Muradyan, P:, The Ascension Island Boundary Layer in the Remote Southeast Atlantic is Often Smoky, 39, https://doi.org/10.1002/2017GL076926, 2018a.

Zuidema, P., Alvarado, M., Chiu, C., DeSzoeke, S., Fairall, C., Feingold, G., Freedman, A., Ghan, S., Haywood, J., Kollias, P., Lewis, E., McFarquhar, G., McComiskey, A., Mechem, D., Onasch, T., Redemann, J., Romps, D., Turner, D., Wang, H.,
1545   Wood, R., Yuter, S., and Zhu P.: Layered Atlantic Smoke Interactions with Clouds (LASIC) Field Campaign Report, edited by: Stafford, R., DOE/SC-ARM-18-018, ARM Climate Research Facility, Report DOE/SC-ARM-18-018, US Dept. of Energy, Office of Science, 2018b.

Figures and Tables

Campaign	Platform	2016	2017	2018
ORACLES (Redemann 2021)	NASA P3 (350 hours) 44 flights	Aug Namibia (115.2)	Aug / Sept São Tomé* (112.0)	Oct São Tomé (121.4)
ORACLES (Redemann 2021)	NASA ER2 (97 hours) 12 flights	Aug Namibia		
CLARIFY	FAAM BAe-146		Aug / Sept	

(Haywood 2021)	(99 hours)		Ascension Island	
LASIC (Zuidema 2018a, b)	ARM Mobile Facility #1	1 June 2016 to 31 Oct 2017 Ascension Island		
AEROCLO-SA (Formenti 2019)	Sapphire ATR-42 30 hours 10 flights		Sept 2017 Namibia	

Table 1 Deployments of ground-based and airborne measurements in the southeast Atlantic during three biomass burning seasons from 2016 to 2018. *The NASA P3 relocated to Ascension Island temporarily to conduct the intercomparison flight in this study.

1550

	Altitude	CODE	Start (All)	End (Aircraft)	End (LASIC)	Notes
FAAM C031 and NASA PRF05Y17 Intercomparison flight	5.8 km	runFT	125119	130222		Upper level
	5.8 km to 330 m	runPRO	130222	132001		Profile descent
	3972 m to 2678 m	runELEV	130755	131222		Elevated Polluted Plume Segment
	330 m 330 m	runBL	132018	133911		Full run
			132030	133930		FAAM AMS
			132030	133420		Low level P3 Normal Inlet
			133450	133940		Low level P3 CVI Inlet
		runBL_A	132018	132929		P3: PM10
		runBL_1	133001	133216		P3: PM1
		runBL_B	133220	133559		P3: PM10
		runBL_2	133601	133816		P3: PM1
		runBL_C	133820	133911		P3: PM10

	1722 m 1731 m	runCLD	134300	135700		Cloud leg BAe-146
			134900	140430		Cloud leg P3
FAAM – LASIC ARM site fly past intercomparison legs	316 m	C030-ARM	163753	165153	170753	17th Aug
	309 m	C031-ARM	144653	145853	151653	18th Aug
	318 m	C033-ARM	101353	102545	104353	22nd Aug
	309 m	C036-ARM	093753	095100	100753	24th Aug
	316 m	C039-ARM	153754	154715	160754	25th Aug
	326 m	C051-ARM	113752	114452	120752	5th Sept

Table 2 Event timing markers during FAAM C031 / NASA PRF05Y17 inter-comparison flight on 18th August 2017 and FAAM-LASIC ARM site intercomparison flight legs on 6 days between 17th August 2017 and 5th September 2017. FAAM Altitudes are GPS corrected to WGS84 geoid.

Parameter	Run	NASA P3	FAAM BAe-146	LASIC ARM #1
Thermodynamics				
T [K]	runBL	294.7 ± 0.1	294.7 ± 0.1	
	runCLD	283.3 ± 0.3	283.3 ± 0.2	
	runELEV	284.2 ± 3.4	284.2 ± 3.4	
	runFT	268.5 ± 0.2	268.6 ± 0.2	
	17th Aug		295.0 ± 0.2	295.8 ± 0.1
	18th Aug		295.0 ± 0.1	295.5 ± 0.1
	22nd Aug		294.0 ± 0.2	294.1 ± 0.2
	24th Aug		294.7 ± 0.2	295.2 ± 0.1
	25th Aug		294.2 ± 0.1	295.0 ± 0.2
	5th Sept		294.3 ± 0.1	295.3 ± 0.1
		-0.05 K	**Mean Bias**	**+ 0.7 K**
vmr (H_2O) [ppm] *Tot1=WISPER CVI, Tot2=WISPER SDI, C=COMA W = WVSS-II*	runBL	**Tot1** 18367 ± 1009 **Tot2** 18333 ± 1021 **C** 19102 ± 903	**W** 19512 ± 971 **B** 19455 ± 935	

B = Buck CR2				
	runCLD	**Tot1** n/a **Tot2** 14399 ± 550 **C** 14592 ± 1015	**W** 14099 ± 360 **B** 14386 ± 442	
	runELEV	**Tot1** 1830 ± 461 **Tot2** 1799 ± 425 **C** 1478 ± 439	**W** 1717 ±411 **B** 1362 ± 312	
	runFT	**Tot1** 140 ± 4 **Tot2** 150 ± 3 **C** n/a	**W** 168 ± 9 **B** 153 ± 5	
	17th Aug		**W** 18635 ± 964 **B** 18537 ± 961	18101 ± 190
	18th Aug		**W** 18907 ± 611 **B** 18873 ± 595	18689 ± 132
	22nd Aug		**W** 20465 ± 692 **B** 20325 ± 745	21026 ± 282
	24th Aug		**W** 20221 ± 1010 **B** 20353 ± 1265	18599 ± 227
	25th Aug		**W** 20980 ± 391 **B** 21095 ± 279	20318 ± 330
	5th Sept		**W** 20971 ± 858 **B** 21096 ± 889	21219 ± 252
		Tot1:W -7 % **Tot2:W -**3 % **Coma:W -**5 %	**Mean Bias**	**L:W** -1.9 % **L:B** -1.9 %
TD [K] *Tot1=WISPER CVI,* *Tot2=WISPER SDI,* *C=COMA*	runBL	**Tot1** 288.4 ± 0.9 **Tot2** 288.4 ± 0.7 **C** 289.0 ± 0.7	**W** 289.3 ± 0.8 **B** 289.5 ± 0.7	

W= WVSS2 B=Buck CR2				
	runCLD	**Tot1** n/a **Tot2** 282.3 ± 0.5 **C** 282.5 ± 1.0	**W** 282.0 ± 0.4 **B** 282.5 ± 0.5	
	runELEV	**Tot1** 252.6 ± 3.4 **Tot2** 252.5 ± 3.2 **C** 249.9 ± 4.2	**W** 251.8 ± 3.4 **B** 252.0 ± 3.0	
	runFT	**Tot1** 223 .0 ± 0.3 **Tot2** 223 .0 ± 0.2 **C** n/a	**W** 224.7 ± 0.5 **B** 228.8 ± 0.3	
	17th Aug		**W** 288.6 ± 0.8 **B** 288.7 ± 0.8	288.6 ± 0.2
	18th Aug		**W** 288.8 ± 0.5 **B** 289.0 ± 0.5	289.0 ± 0.1
	22nd Aug		**W** 290.0 ± 0.5 **B** 290.2 ± 0.6	291.0 ± 0.2
	24th Aug		**W** 289.9 ± 0.8 **B** 290.2 ± 1.0	289.0 ± 0.2
	25th Aug		**W** 290.4 ± 0.3 **B** 290.7 ± 0.2	290.4 ± 0.3
	5th Sept		**W** 290.4 ± 0.6 **B** 290.8 ± 0.7	291.1 ± 0.2
		Tot1:W -0.6 K **Tot2:W** -0.2 K **COMA:W** -0.6 K	**Mean Bias**	**W** 0.17 K **B** -0.1 K
RH [%]	runBL	**Tot1** 68 ± 3 **Tot2** 68 ± 3 **C** 70 ± 4	**W** 70 ± 4 **B** 72 ± 4	

Tot1=WISPER CVI, *Tot2=WISPER SDI,* *C=COMA* *W= WVSS2* *B=Buck CR2*				
	runCLD	**Tot1** n/a **Tot2** 94 ± 3 **C** 95 ± 6	**W** 90 ± 2 **B** 94 ± 3	
	runELEV	**Tot1** 10 ± 3 **Tot2** 9 ± 2 **C** 8 ± 2	**W** 9 ± 2 **B** 8 ± 1	
	runFT	**Tot 1** 1 ± 0 **Tot2** 2 ± 0 **C** n/a	**W** 2 ± 0 **B** 3 ± 0	
	17th Aug		**W** 66 ± 4 **B** 67 ± 4	63 ± 1
	18th Aug		**W** 68 ± 2 **B** 69 ± 2	67 ± 1
	22nd Aug		**W** 77 ± 3 **B** 79 ± 3	82 ± 1
	24th Aug		**W** 73 ± 4 **B** 76 ± 6	68 ± 1
	25th Aug		**W** 79 ± 2 **B** 81 ± 1	75 ± 2
	5th Sept		**W** 77 ± 4 **B** 80 ± 4	77 ± 1
		Tot1:W -0.9 % RH **Tot2:W** -0.2 % RH **COMA:W** -1.2 % RH	**Mean Bias**	**W** -1.2 % RH **B** -3.3 % RH

Vertical wind velocity				
standard deviation [m s^{-1}]	runBL	0.44	0.62	
Skewness	runBL	0.76	0.38	
Airmass Tracers				
CO [ppb]	runBL	102 ± 5	96 ± 4	
	runCLD	92 ± 2	91 ± 3	
	runELEV	94 ± 5	86 ± 5	
	runFT	90 ± 1	84 ± 1	
	17th Aug		97 ± 4	90 ± 1
	18th Aug		89 ± 5	81 ± 0
	22nd Aug		62 ± 2	61 ± 1
	24th Aug		72 ± 3	68 ± 1
	25th Aug		67 ± 2	64 ± 0
	5th Sept		106 ± 3	102 ± 1
		5	**Mean Bias**	**-4.8**
		y = 8 + 0.97x	**Linear regression**	**y = 0.24 + 0.94x**
O3 [ppb]	runBL	38 ± 2	41 ± 1	
	runCLD	40 ± 3	42 ± 1	
	runELEV	61 ± 2	59 ± 1	
	runFT	73 ± 3	71 ± 0	
	17th Aug		42.0 ± 0.8	42.9 ± 0.5
	18th Aug		38.2 ± 0.7	39.2 ± 0.5
	22nd Aug		30.4 ± 0.5	32.3 ± 0.5
	24th Aug		34.1 ± 0.5	35.3 ± 0.5
	25th Aug		30.2 ± 0.4	31.7 ± 0.5

	5th Sept		44.1 ± 0.8	44.8 ± 0.5
		-0.27	**Mean Bias**	**1.2**
		y = -10 + 1.19x	**Linear regression**	**y = 3.8 + 0.93x**
Chemical composition				
rBC$_n$ [cm^{-3}]	17th Aug		164 ± 14	129 ± 2
	18th Aug		111 ± 14	84 ± 2
	22nd Aug		5 ± 2	5.2 ± 0.3
	24th Aug		21 ± 5	12.0 ± 0.7
	25th Aug		5.4 ± 2	3.8 ± 0.5
	5th Sept		101 ± 5	78 ± 1
			Linear regression	**y = -1 + 0.79x**
rBC$_m$ [ng m^{-3}]	17th Aug		413 ± 42	368 ± 10
	18th Aug		302 ± 46	251 ± 8
	22nd Aug		19 ± 6	20 ± 2
	24th Aug		74 ± 22	40 ± 4
	25th Aug		23 ± 9	13 ± 3
	5th Sept		367 ± 31	299 ± 5
			Linear regression	**y = -10 + 0.88x**
OA [µg m^{-3}]	runBL	2.25 ± 0.36	2.66 ± 0.31	
SO4 [µg m^{-3}]	runBL	1.96 ± 0.23	1.39 ± 0.14	
NO3 [µg m^{-3}]	runBL	0.09 ± 0.05	0.11 ± 0.02	
NH4 [µg m^{-3}]	runBL	0.43 ± 0.06	0.47 ± 0.07	
f43	runBL	0.047±0.019	0.055±0.028	
f44	runBL	0.24±0.03	0.24±0.07	
mz30 over 46 ratio	*runBL*	*2.9 ± 1.1*	*3.5 ± 0.5*	

mz30 over 46 ratio _ cal	*runBL*	*1.65*	*1.2*	
m/z30	*runBL*	*0.034 ± 0.017*	*0.041 ± 0.008*	
m/z46	*runBL*	*0.008 ± 0.005*	*0.012 ± 0.002*	
f30 (m/z30 / NO₃)	*runBL*	*0.40 ± 0.16*	*0.44 ± 0.02*	
f46 (m/z46 / NO₃)	*runBL*	*0.12 ± 0.09*	*0.11 ± 0.02*	
Aerosol Optical				
σ_{SP} [Mm^{-1}]				
470 nm	runBL_1	47 ± 3	42 ± 3	
	runFT	0.3 ± 2.4	1.6 ± 0.7	
	runFT	1.2 ± 2.3 *(PM10)*	1.6 ± 0.7	
	runBL_A	*67 ± 3 (PM10)*	46 ± 4	
	runBL_B	*60 ± 3 (PM10)*	39 ± 3	
	17th Aug		50 ± 3	34.20 ± 0.10
	18th Aug		34 ± 2	22.70 ± 0.30
	22nd Aug		8 ± 1	2.70 ± 0.20
	24th Aug		11 ± 2	4.60 ± 0.40
	25th Aug		5 ± 1	0.60 ± 0.10
	5th Sept		38 ± 1	27.08 ± 0.05
		y = -0.8 + 1.52x (PM10) **y = -1.5 + 1.2x (PM1)**	**Linear regression**	**y = -2.8 + 0.74x**
660 nm	runBL_1	27 ± 2	30 ± 6	
	runFT	0.5 ± 1.3	0.8 ± 1.2	
	runFT	0.9 ± 1.9 *(PM10)*	0.8 ± 1.2	
	runBL_A	*48 ± 3 (PM10)*	32 ± 5	
	runBL_B	*45 ± 3 (PM10)*	27 ± 5	
	17th Aug		33 ± 2	12.12 ± 0.02

	18th Aug		25 ± 2	8.00 ± 0.20
	22nd Aug		6 ± 2	1.40 ± 0.20
	24th Aug		9 ± 2	1.90 ± 0.30
	25th Aug		-	0.31 ± 0.04
	5th Sept		-	12.40 ± 0.01
		y = -0.1 + 1.56x (PM10) **y = -0.3 + 0.9x (PM1)**	**Linear regression**	**y = -1.3 + 0.39x**
σ_{AP} [Mm^{-1}]				
470 nm	runBL_B	5.2 ± 0.2	6.0 ± 0.5	
	runBL_2	5.57 ± 0.14	6.0 ± 0.3	
	runBL_C	5.09 ± 0.17	5.6 ± 0.4	
	17th Aug		7.1 ± 0.6	6.7 ± 0.2
	18th Aug		5.0 ± 0.5	5.0 ± 0.2
	22nd Aug		0.6 ± 0.3	0.3 ± 0.1
	24th Aug		1.3 ± 0.5	0.8 ± 0.1
	25th Aug		0.3 ± 0.15	0.3 ± 0.1
	5th Sept		6.2 ± 0.6	6.0 ± 0.1
		Y = 0.90x	**Linear regression**	**y = -0.39 + 0.99x**
660 nm	runBL_B	3.6 ± 0.4	3.8 ± 0.7	
	runBL_2	4.0 ± 0.1	3.7 ± 0.5	
	runBL_C	3.5 ± 0.2	3.5 ± 0.5	
	17th Aug		4.6 ± 0.7	4.7 ± 0.1
	18th Aug		3.5 ± 0.5	3.5 ± 0.1
	22nd Aug		0.47 ± 0.48	0.14 ± 0.1
	24th Aug		0.85 ± 0.5	0.6 ± 0.1
	25th Aug		-	0.25 ± 0.1
	5th Sept		-	4.3 ± 01
		Y = 1.01x	**Linear regression**	**y = -0.33 + 1.07x**

				PSAP *CAPS PM$_{SSA}$*
530 nm	runBL_B	4.6 ± 0.2	5.3 ± 0.4	
	runBL_2	3.9 ± 0.1	5.1 ± 0.3	
	runBL_C	4.2 ± 0.2	5.2 ± 0.3	
	17th Aug		6.0 ± 1.1	5.9 ± 0.1 *7.4 ± 2.2[†]*
	18th Aug		4.1 ± 1.0	4.3 ± 0.1 *5.0 ± 2.0*
	22nd Aug		-	0.18 ± 0.1 -
	24th Aug		1.2 ± 0.7	0.7 ± 0.1 *1.1 ± 1.8*
	25th Aug		-	0.3 ± 0.0 *0.76 ± 1.78*
	5th Sept		5.4 ± 0.9	5.2 ± 0.0 *6.9 ± 2.2[†]*
		Y = 0.98x	**Linear regression**	**y = -0.25 + 1.03x** *y = 0.10 + 1.23x[†]*
CN [cm^{-3}]	runBL_A	741 ± 14	821 ± 14	
	runBL_1	692 ± 25	777 ± 27	
	runBL_B	650 ± 60	716 ± 10	
	17th Aug		890 ± 50	714 ± 8
	18th Aug		650 ± 50	494 ± 6
	22nd Aug		178 ± 11	153 ± 4
	24th Aug		220 ± 80	148 ± 5
	25th Aug		130 ± 40	62 ± 4
	5th Sept		285 ± 8	274 ± 13

		y = 2 + 0.90x	Linear regression	y = -12 + 0.81x
		NASA	**FAAM**	**LASIC**
		PCASP *(UHSAS)*	PCASP1 PCASP2	
N_A [cm^{-3}]	runBL	550 ± 61, *(570 ± 54)*	516 ± 63 484 ± 63	
	runCLD	402 ± 28	374 ± 33 346 ± 39	
	runELEV	76 ± 22	74 ± 23 67 ± 22	
	runFT	26 ± 12	22 ± 7 16 ± 5	
			PCASP2 (>120nm) PCASP3 (>120nm) SMPS (>120nm) (SMPS (all))	SMPS (>120 nm) (SMPS (all))
	17th Aug		640 ± 74 678 ± 217 535 ± 32 (777 ± 37)	490 ± 5 (678 ± 4)
	18th Aug		404 ± 55 407 ± 138 362 ± 38 (535 ± 47)	361 ± 4 (509 ± 1)
	22nd Aug		20.3 ± 8.6 21.2 ± 11.5 11.8 ± 6.5 (91.0 ± 14.1)	32.4 ± 1.5 (135 ± 2)

	24th Aug		86.2 ± 16.8 97.0 ± 39.7 79.1 ± 44.8 (120 ± 49)	54.9 ± 3.1 (148 ± 8)
	25th Aug		21.1 ± 6.7 21.2 ± 8.4 10.7 ± 3.7 (21.1 ± 10.1)	21.5 ± 1.8 (59.7 ± 3.0)
	5th Sept		259 ± 25 294 ± 64 120 ± 14 (259 ± 41.3)	197 ± 5 (254 ± 6)
		PCASP1: **y = 0.24 + 1.07x** **PCASP2:** **Y = 5.0 + 1.13x**	**Linear regression**	**PCASP2:** **Y = 6.0 + 0.78x** **PCASP3:** **Y = 4.9 + 0.74x** **SMPS:** **Y = 25.7 + 0.90x** **SMPS (all):** **Y = 50.3 + 0.82x**
R_e [μm]	runBL	0.139 ± 0.004, *(0.123 ± 0.14)*	0.140 ± 0.004 0.133 ± 0.003	
	runCLD	0.146 ± 0.004 (n/a)	0.144 ± 0.005 0.134 ± 0.004	
	runELEV	0.152 ± 0.014 (n/a)	0.157 ± 0.018 0.145 ± 0.014	
	runFT	0.110 ± 0.031 (n/a)	0.114 ± 0.033 0.111 ± 0.032	
		PCASP1:	**Linear regression**	

		y = 0.002 + 0.97x PCASP2: Y = -0.03 + 1.27x		
Cloud Physical		**CDP**	**CDP**	
CMD [μm]	runCLD	11.35 (11.12)*	10.92	
R_e [μm]	runCLD	7.2 ± 1.5 (7.0 ± 1.4)*	7.0 ± 1.5	
R_V [μm]	runCLD	7.9 ± 1.5 (7.7 ± 1.4)*	7.8 ± 1.6	
	Percentiles	*[75th, 90th, 99th]*	*[75th, 90th, 99th]*	
N_c [cm^{-3}]	runCLD	274 ± 153 *[366, 528, 595]* (253 ± 137)* *([351, 487, 539)]**	226 ± 69 *[288, 308, 335]*	
LWC [g m^{-3}]	runCLD	0.37 ± 0.43 *[0.39, 0.68, 2.1]* (0.24 ± 0.15)* *([0.36, 0.50, 0.63])**	0.23 ± 0.15 *[0.35, 0.47, 0.76]*	
		King probe	**Nevzorov LWC1**	
		0.20 ± 0.31 *[0.22, 0.37, 1.46]* (0.12 ± 0.10)* *([0.21, 0.25, 0.36])**	0.23 ± 0.16 *[0.37, 0.46, 0.57]*	

Table 3 Summary of comparisons from NASA, FAAM for multiple flight levels and LASIC for 6 FAAM fly-pasts for thermodynamic properties, chemical composition, carbon monoxide and ozone concentrations, aerosol optical properties, aerosol particle number concentrations and submicron properties of the aerosol particle distributions. Data are presented as mean and standard deviations apart from for N_c which is presented as 75th, 90th and 99th percentiles. Linear regression parameters are shown and where an offset is not given the fit was performed with a fixed intercept of zero. † - LASIC CAPS PM$_{SSA}$ data behind PM10 inlet. * - NASA cloud data derived values with the updraught data removed where updraughts was stronger than 2 ms^{-1}.

	FAAM BAe-146	NASA P3

Module spectral range	0.40-0.95μm [Wm⁻²]	0.96-1.69μm [Wm⁻²]	0.40-0.95μm [Wm⁻²]	0.96-1.69μm [Wm⁻²]
SLR: runFT, 12:51-13:02	779 (9)	303 (4)	767 (3)	308 (1)
Profile: 13:02-13:20	771 (37)	290 (37)	753 (30)	291 (38)
SLR: runBL: 13:20-13:39	567 (357)	169 (124)	566 (384)	168 (136)
SLR: runFT, 12:51-13:02	*85 (76)*	*20 (29)*	*86 (79)*	*21 (30)*

Table 4 The integrated fluxes derived from the SHIMS and SSFR instruments over the SHIMS module spectral ranges. The measurements in standard font represent downwelling irradiances, while those in italics represent upwelling irradiances. Values in brackets denote 2 standard deviations.
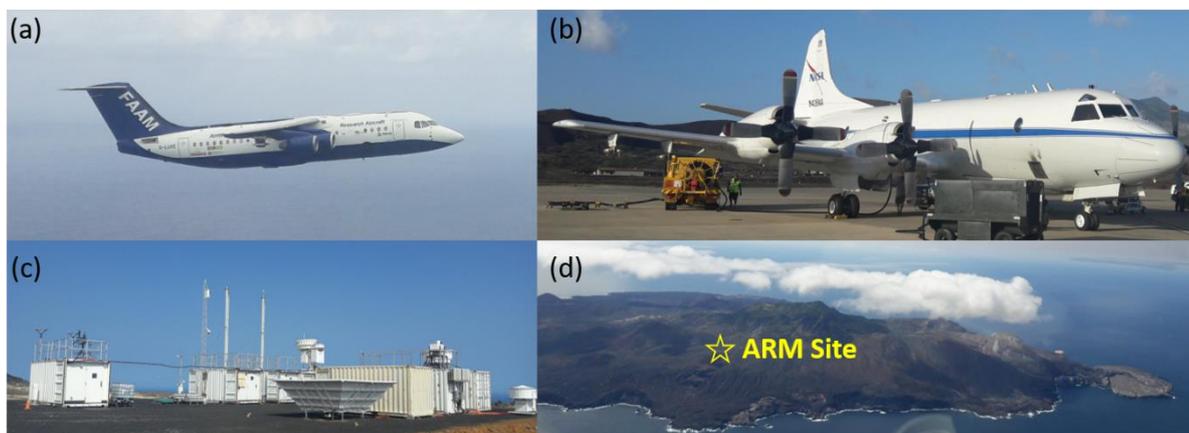
1565 **Figure 1 The observations platforms during (a) CLARIFY: the FAAM BAe-146, (b) ORACLES: the NASA P3 and (c) LASIC: Mobile ARM Facility #1 and (d) the location on Ascension Island of the ARM Mobile Facility #1 on Nasa Road, Ascension Island. This photograph was taken looking approximately NNE showing the site exposed to the prevailing south westerly winds.**
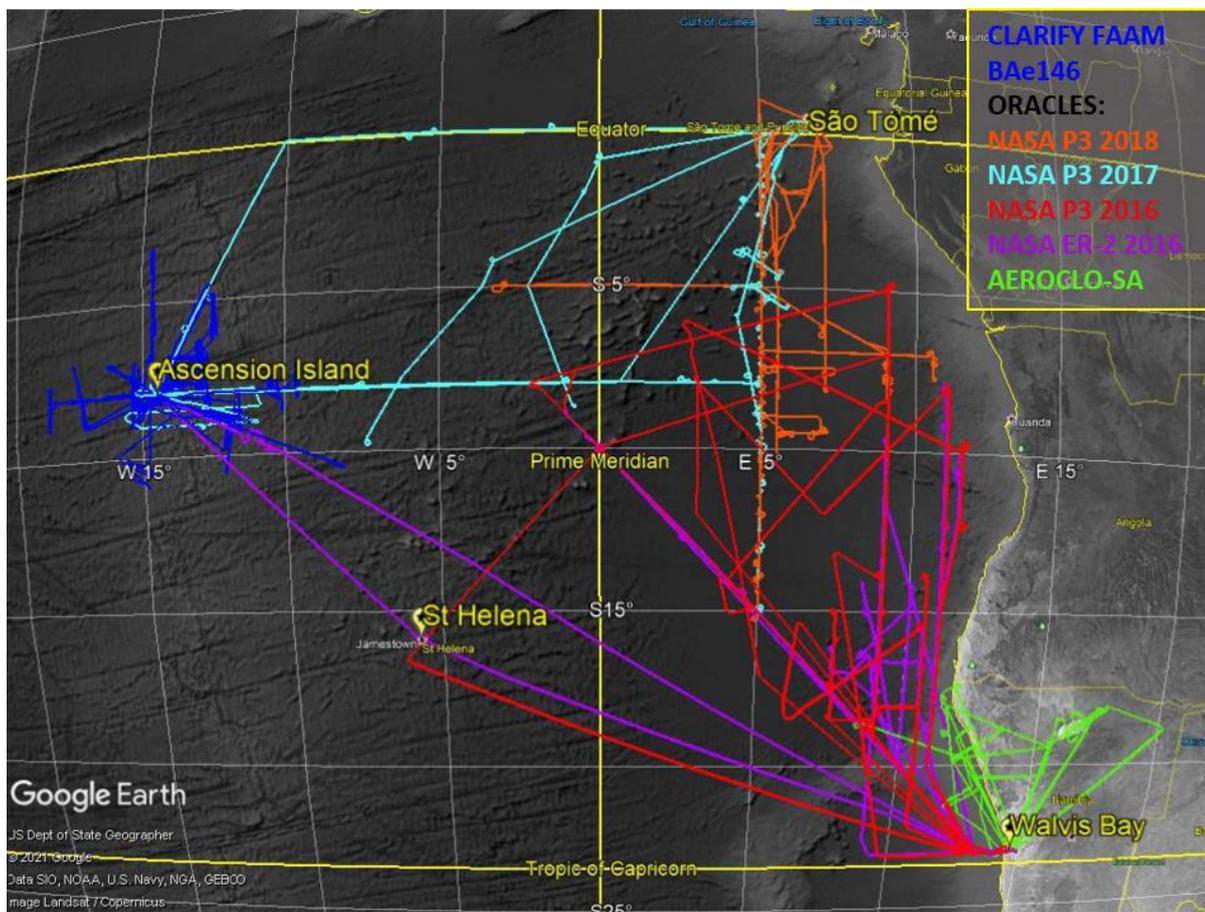
Figure 2 Flight tracks for science flights (transit and ferry flights omitted), ((c) Google Earth 2021) from CLARIFY 2017 (FAAM BAe-146), ORACLES 2016 (NASA P3 and ER-2), 2017 (P3), 2018 (P3), along and AEROCLO-SA (Falcon20).
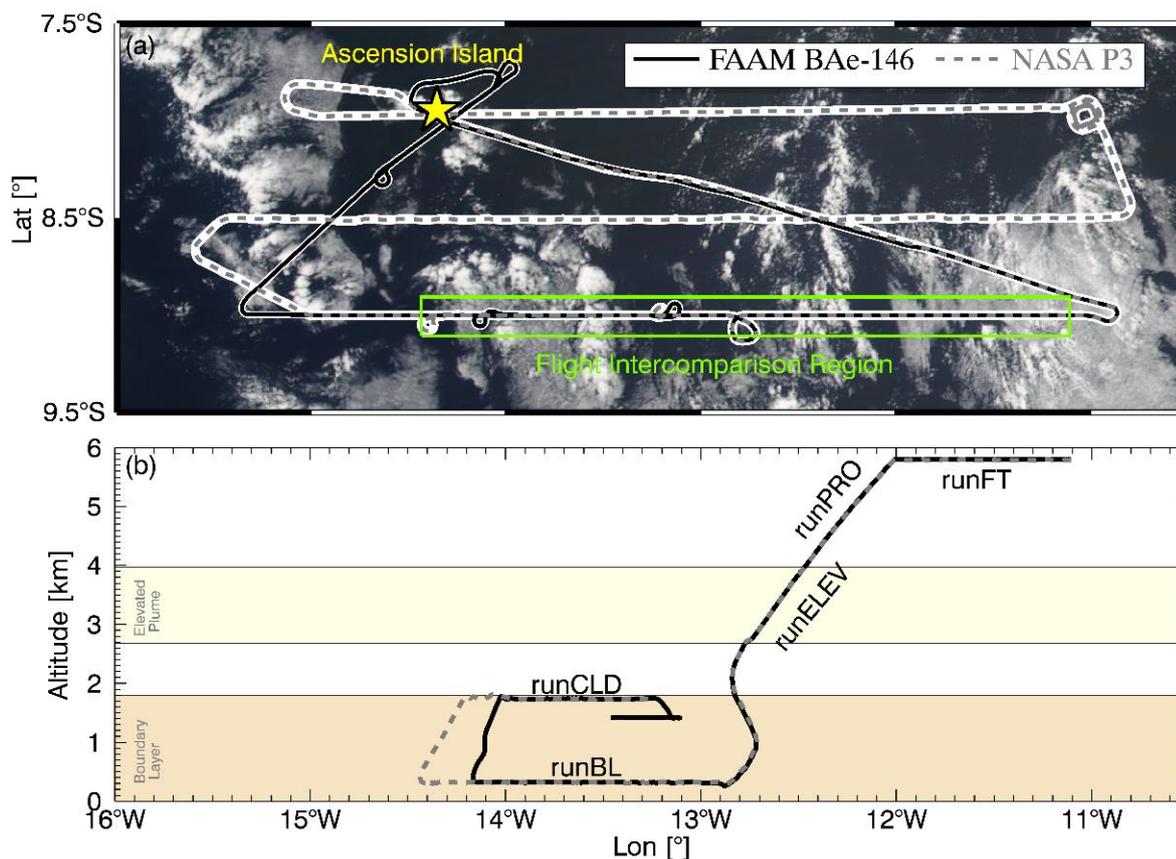
Figure 3 (a) Flight tracks for both the FAAM BAe-146 and NASA P3 flights with the inter-comparison flight segment marked (green box), overlaid on VIIRS Corrected Reflectance (True Colour) imagery from 18th August 2017, (b) Flight vertical cross sections as a function of longitude for the intercomparison segment for FAAM BAe-146 and NASA P3, which commenced at 5.8 km. Run names are indicated (see Table 2), along with horizontal bands which mark out the elevated pollution plume (yellow) and boundary layer (light orange).

1575
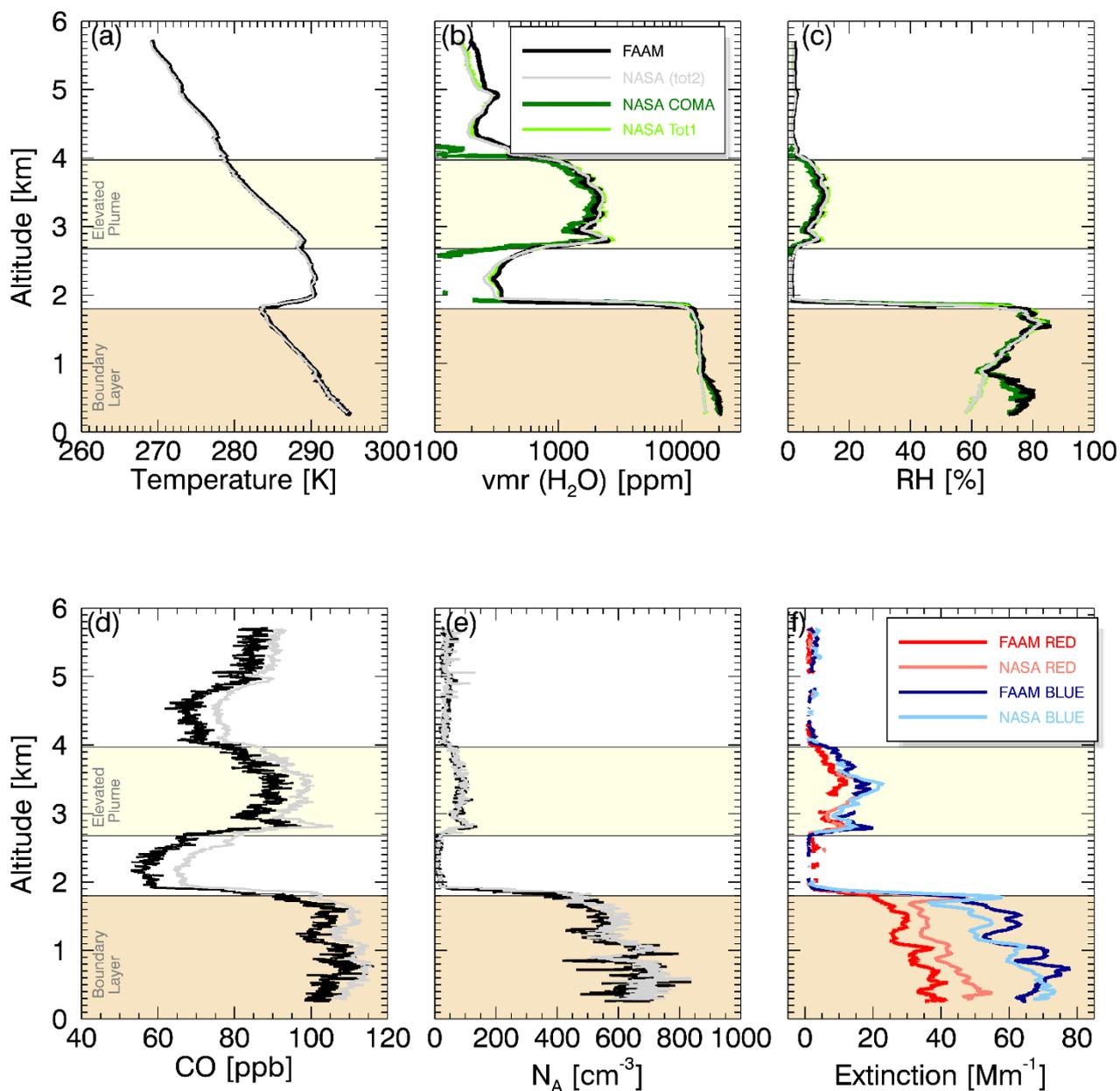
Figure 4 Vertical profiles of data from FAAM BAe-146 and NASA P3 for intercomparison "runPRO" descent from 5.8 km to 300 m for (a) temperature, (b) water vapour mixing ratio, (c) RH, (d) CO, (e) N_A from PCASP, and (f) σ_{EP} from FAAM EXSCALABAR CRDS and NASA PSAP+Nephelometer for wavelengths of 470 nm (blue) and 660 nm (red). The legend on panel (b) applies to panels (a)-(e). The legend on panel (f) applies only to panel (f). Horizontal bands mark out the elevated pollution plume (yellow) and boundary layer (light orange).

1580
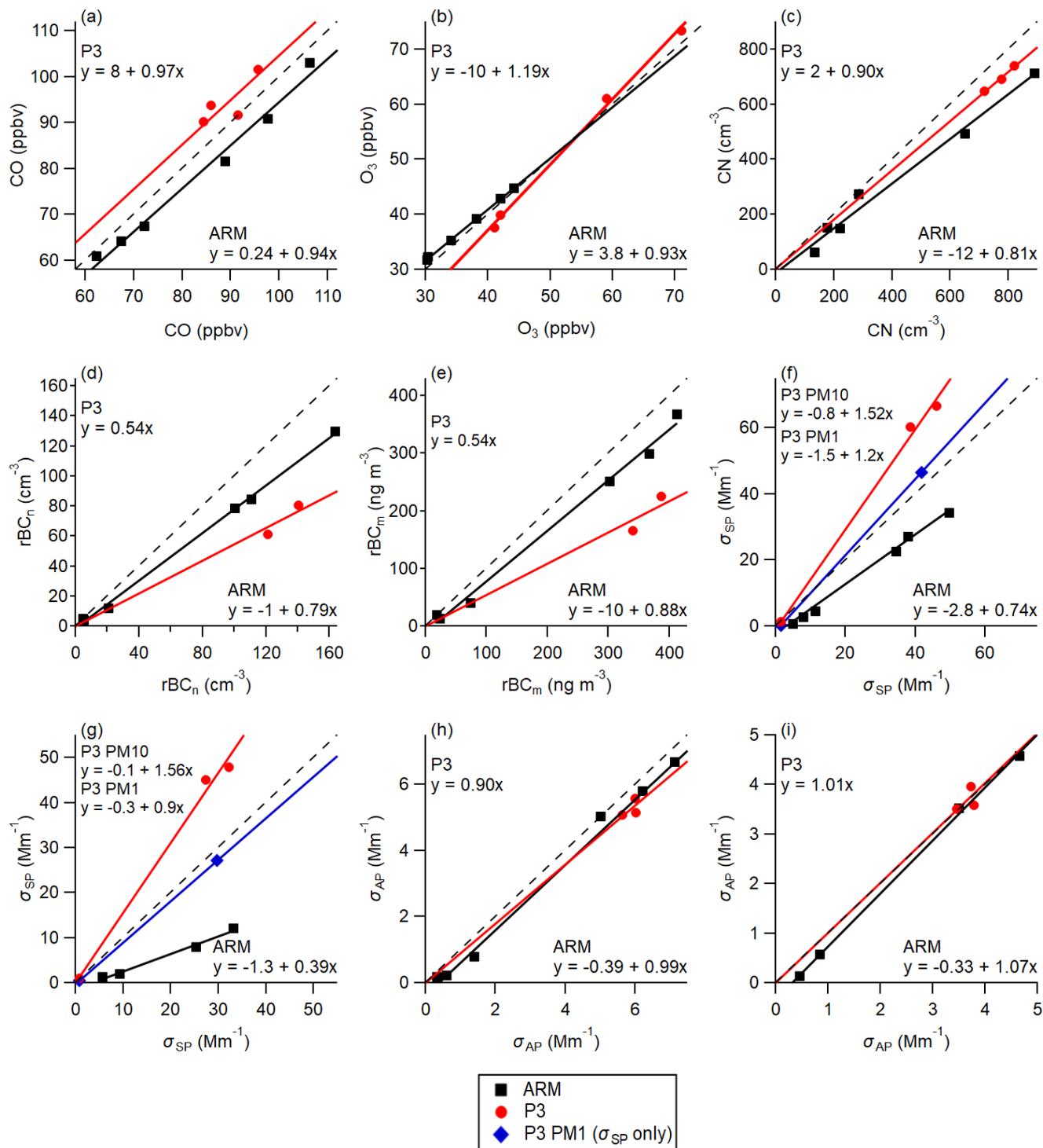
Figure 5 Correlations between parameters (Table 3) as a function of those measured onboard the FAAM BAe-146 for both the NASA P3 and with P3 data behind a PM1 impactor, from various flight segments (Table 2) and LASIC ARM site from 6 flights for (a) CO,

1585

(b) O₃, (c) CN, (d) rBC$_n$, (e) rBC$_m$, (f) σ$_{SP}$ at 470 nm and (g) σ$_{SP}$ at 660 nm, (h) σ$_{AP}$ at 470 nm and (i) σ$_{AP}$ at 660 nm The 1:1 ratio line is shown on all panels as a dashed-black line, and linear fit parameters are shown.
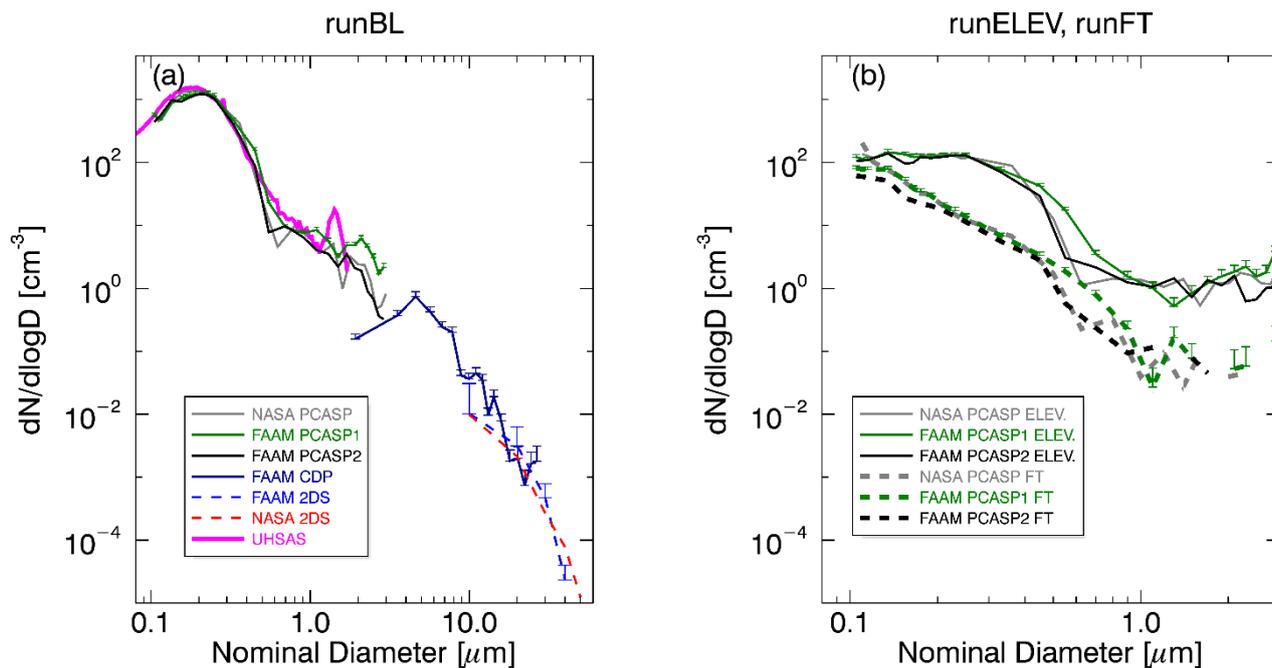
Figure 6 Aerosol PSD for (a) runBL (b) runELEV (solid lines) and runFT (dashed lines). Errors (positive only) are only shown for
1590   **FAAM PCASP1 to aid clarity - see main text for details.**
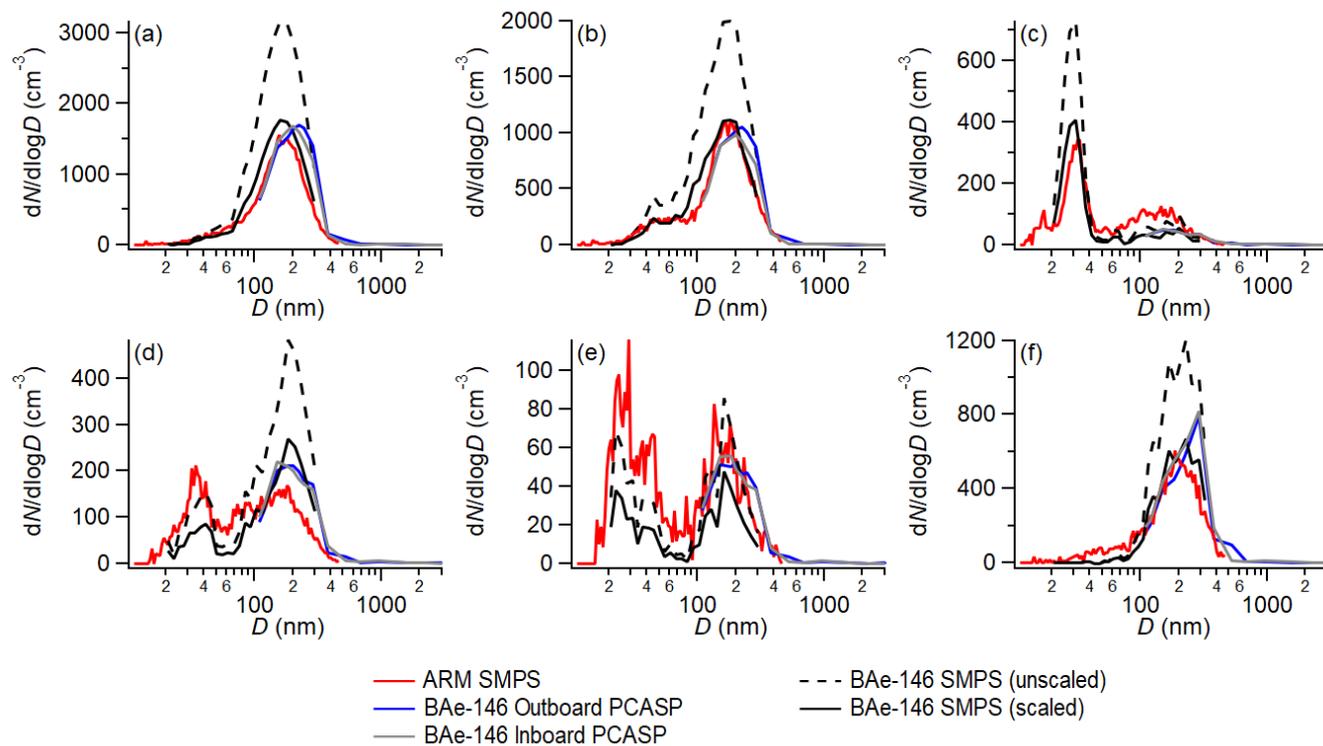
Figure 7 Particle size distribution for 6 FAAM–LASIC fly-past flight legs for (a) 17th August 2017, (b) 18th August 2017, (c) 22nd August 2017, (d) 24th August 2017, (e) 25th August 2017, (f) 5th September 2017.
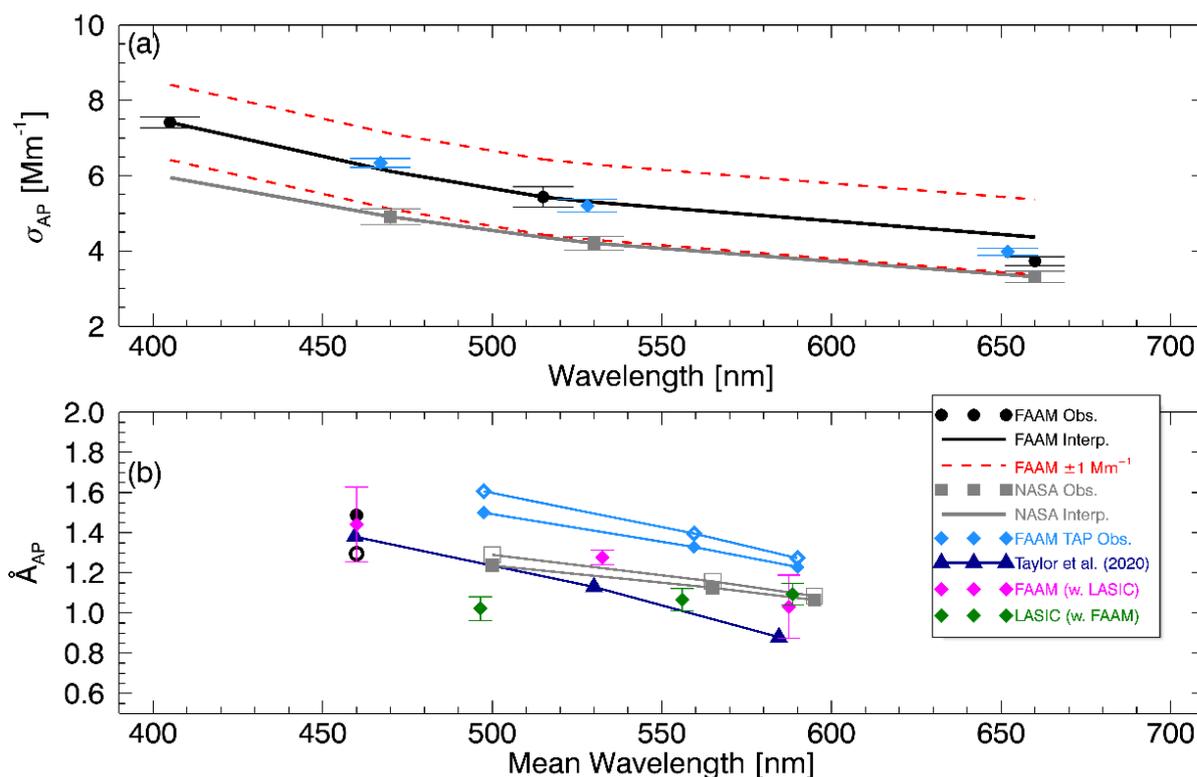
1595

Figure 8 Optical absorption coefficient as a function of wavelength for boundary layer leg runBL_2 (Table 2). Observations are shown as mean (symbols) and standard deviation (error bars) for FAAM EXSCALABAR PAS and NASA PSAP data, along with FAAM TAP data. Interpolated values of σ_{AP} are shown which use $Å_{EP}$ from observations for FAAM and NASA except for FAAM at wavelengths longer than 515 nm which uses the CLARIFY campaign mean value of $Å_{EP}$ (514:660) = 0.88 from Taylor et al. (2020). (b) $Å_{EP}$ as function of pairs of mean wavelengths for runBL_1 (filled symbols) and runBL_2 (hollow symbols). The range of observations from the 3 FAAM fly-pasts of the LASIC ARM site are shown. Full CLARIFY campaign data are reproduced from Taylor et al. (2020).

1600
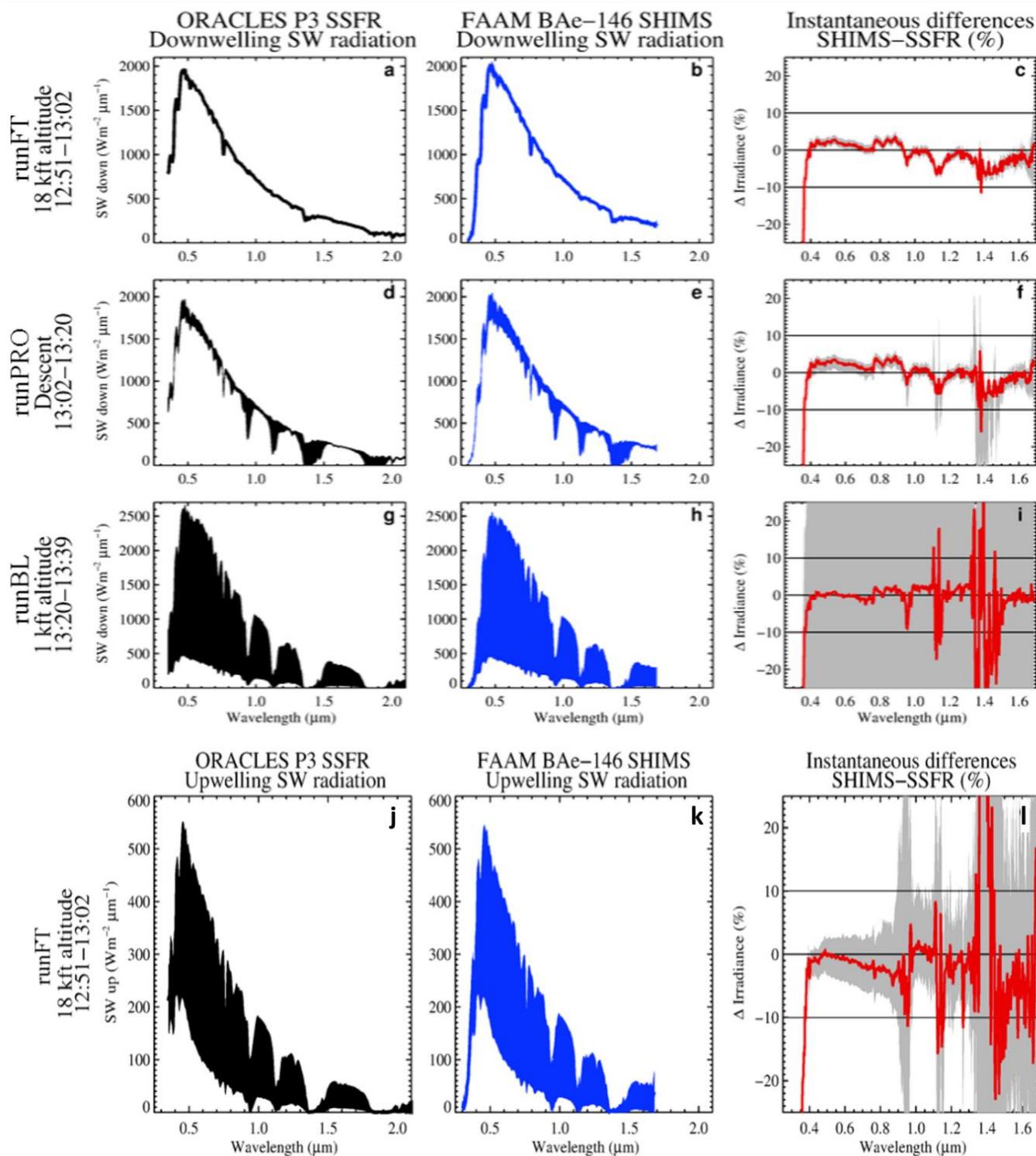
1605 **Figure 9 Intercomparison of downwelling shortwave spectral irradiance from (left column) ORACLES NASA P3, (centre column) CLARIFY FAAM BAe-146 and (right column) percentage differences, for 3 wing-tip to wing-tip manoeuvres: (a)-(c) runFT, (d)-(f) runPRO, (g)-(i) runBL, and intercomparison of upwelling shortwave spectral irradiance for runFT (as (a)-(c). Black and blue filled contours in the first two columns show the observed spectral irradiance ranges. Grey filled contours in the third column show the range of percentage differences in paired measurements, overlaid with the average percentage difference (red line).**
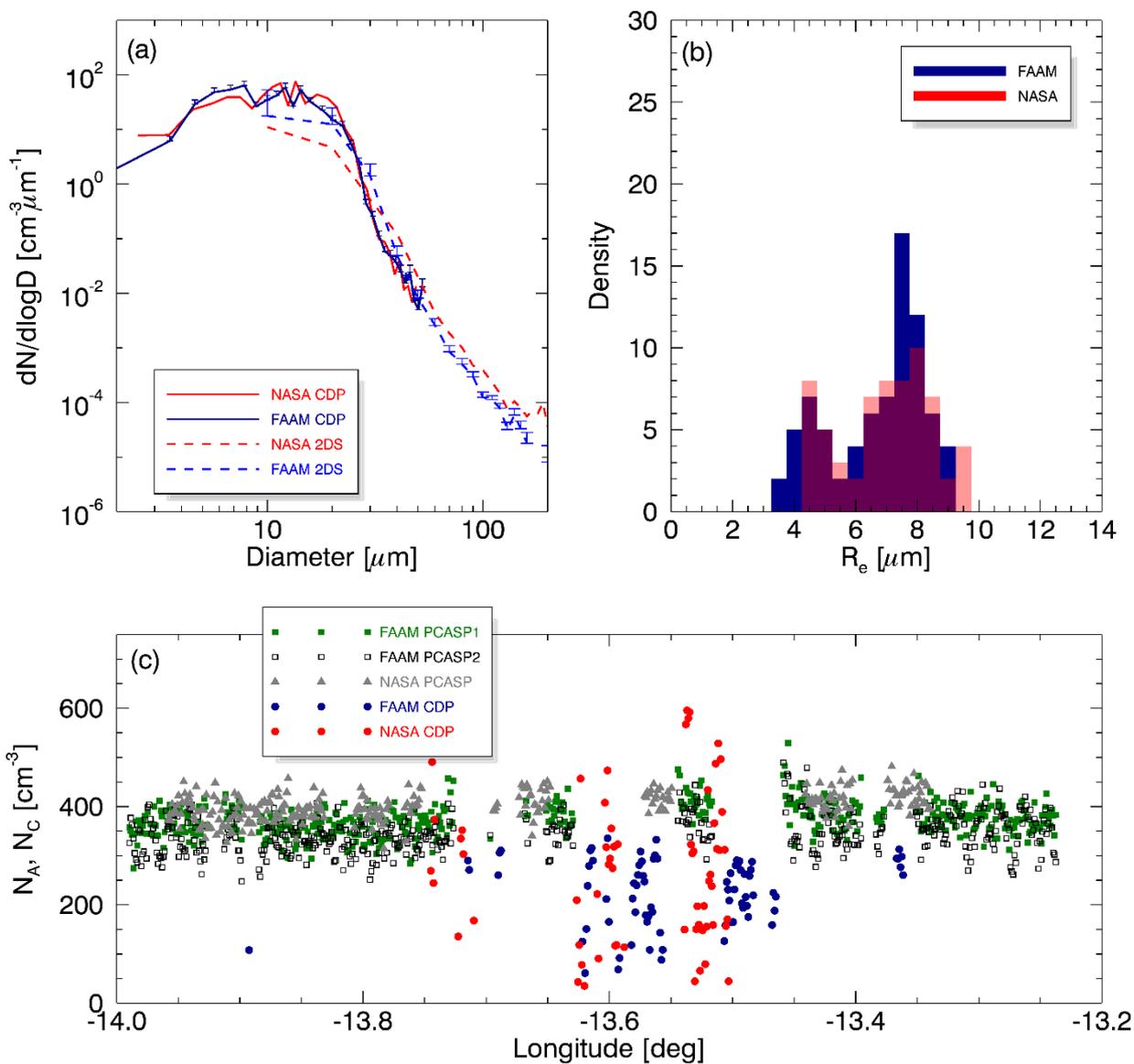
Figure 10 (a) Cloud PSD, (b) PDF of cloud particle R_e, and (c) time series of N_c (CDP) and interstitial N_A (PCASP) at cloud-level.
1610 **Errors on PSD as Fig. 6 are shown only for FAAM platform to aid clarity.**